

AN ABSTRACT OF THE DISSERTATION OF

Alvin J. Gatimu for the degree of Doctor of Philosophy in Chemistry presented on July 10, 2012.

Title: Structure-Property Relationships in Oxides Containing Select Platinum Group Metals.

Abstract
approved: _____

Munirpallam A. Subramanian

Oxide materials exhibit a wide variety of structures and properties. In particular, transition metal oxides tend to be highly stable while exhibiting a wide range of properties that can be used for numerous applications. This work focuses on investigating how the structures' of 4d and 5d transition metal oxides influences their properties. Specifically oxides of Ru, Rh and Ir were investigated.

A complete solid solution was found between isostructural $\text{Pb}_3\text{Mn}_7\text{O}_{15}$ and $\text{Pb}_3\text{Rh}_7\text{O}_{15}$. $\text{Pb}_3\text{Rh}_7\text{O}_{15}$ shows a Verwey-type transition at 185 K. This transition remains with a 3 % substitution of Mn for Rh but disappears with a 4 % substitution of Mn for Rh. The structure was found to expand in the direction perpendicular to the layers of the structure, which is the *c*-axis, despite a contracting unit cell. Bi for Pb substitution in $\text{Pb}_3\text{Mn}_7\text{O}_{15}$ was found to be limited as compared to in $\text{Pb}_3\text{Rh}_7\text{O}_{15}$.

Alkali metal substitution on the A-site of the orthorhombic perovskite SrRuO_3 showed only low substitution levels were possible. Nonetheless, the substituted phases showed decreased ferromagnetic Curie temperatures, increased electrical

resistivity and relatively unchanged Seebeck coefficients. Thermoelectric studies of $\text{Sr}_{2-x}\text{La}_x\text{CoRuO}_6$ perovskite phases showed $\text{Sr}_{1.1}\text{La}_{0.9}\text{CoRuO}_6$ with the best thermoelectric performance. This system showed possible correlations between cation ordering on the B-site and the charge carrier transport. A similar thermoelectric study of $(\text{RhV})_{1+x}\text{Ti}_{1-2x}\text{O}_6$ phases crystallizing in a disordered trirutile structure was done. Electron carriers were found to be dominant and dependent on Ti content. The electron carriers appear to become diminished at higher temperatures.

Sr_2IrO_4 crystallizes in a K_2NiF_4 -type structure. Effects of Ti, Fe and Co substitution for Ir were investigated. A complete $\text{Sr}_2\text{Ir}_{1-x}\text{Ti}_x\text{O}_4$ solid solution was synthesized and characterized while limited solubility was found for Fe and Co substitutions. All substitutions showed a decrease in the *c*-cell parameter coupled with a decrease in octahedral tilting. All substitutions also showed a decrease in magnetic susceptibility and an increase in the paramagnetic effective moment was observed for Co and Fe doped samples. An incomplete solid solution was formed for $\text{Sr}_2\text{Ti}_{1-x}\text{Rh}_x\text{O}_4$ phases; however effects of increased octahedral tilting with higher Rh content were observed.

©Copyright by Alvin J. Gatimu
July 10, 2012
All Rights Reserved

Structure-Property Relationships in Oxides Containing Select Platinum Group
Metals.

by

Alvin J. Gatimu

A DISSERTATION

submitted to

Oregon State University

in partial fulfillment of
the requirements for the
degree of

Doctor of Philosophy

Presented July 10, 2012

Commencement June 2013

Doctor of Philosophy dissertation of Alvin J. Gatimu presented on July 10, 2012.

APPROVED:

Major Professor, representing Chemistry

Chair of the Department of Chemistry

Dean of the Graduate School

I understand that my dissertation will become part of the permanent collection of Oregon State University libraries. My signature below authorizes release of my dissertation to any reader upon request.

Alvin J. Gatimu, Author

ACKNOWLEDGEMENTS

It has been the opportunity of a lifetime to pursue my degree at Oregon State University. Growing up in a place where a basic education is still so hard to attain for so many, having the opportunity to learn from so many outstanding teachers has been an unbelievable blessing. I feel like I have so many individuals to thank for the ride of my life that has been the last four years. I'm eternally grateful to God for surrounding me with so many wonderful people, some whom I may unfortunately not be able to thank and acknowledge in the next few short paragraphs.

To refer to Dr. M.A. Subramanian as a brilliant scientist would be a serious understatement. His profound knowledge extends way beyond the barriers of solid state chemistry. I have been blessed to learn most of all the chemistry I may ever claim to know from him. I will forever be indebted to him for instilling in me a work ethic and passion that I have never had. He has exemplified a work ethic, passion and commitment that I have greatly benefitted from.

It has also been a great honor to learn from and discuss with Dr. A.W. Sleight. His pioneering research has laid the foundation for much of the solid state chemistry research ongoing today. His unique insights and exceptional abilities in understanding inorganic structures and their properties have greatly influenced and contributed to this thesis. I consider myself incredibly fortunate to have had the opportunity to listen to, be questioned by and ultimately learn from him. I would also like to thank the rest of my graduate committee consisting of Dr. Brady Gibbons, Dr. Michael Lerner, Dr.

Paul Cheong, Dr. Fred Prahel and Dr. Oleh Taratula. Their support and commitment have been truly appreciated.

None of the work in this thesis would have been possible without the encouragement and assistance of all previous and present Subramanian research group members over the last four years. I sincerely thank Dr. Andrew E. Smith, and Dr. Hiroshi Mizoguchi for introducing me to general laboratory procedures and for their patience with me. I also thank Dr. Sean Muir for his help with research endeavors. His jovial nature has been infectious and made working in the office and laboratory an everyday pleasure. Thank you also to Dr. Jun Li for her teachings in structure refinements, Dr. Romain Berthelot for numerous productive discussions and Dr. Krishnendu Biswas for his guidance. Furthermore, I thank Dr. James Eilertsen, Dr. Theeranun 'June' Siritanon, Peng Jiang, Geneva Luarita-Plankis, Rosa Grajczyk and all other members of the Subramanian research group.

Thank you to Dr. Lev Zakharov for single crystal refinements and productive discussions. In addition, I sincerely thank the Chemistry department for their support. In particular thank you to the Lerner and Keszler research groups, Luanne, Paula, Talley, Kristi, Todd, Greg, Austin, Dan, Joey, and Rene. It has been a great pleasure to be daily surrounded by such outstanding individuals. I also thank Dr. Rahim Kazerouni, my undergraduate advisor who believed in me and directed me towards pursuit of this degree.

Finally, a thank you to those who know me best: my family and friends. I thank my parents for their unending love and support for which I daily thank the Lord for. Thank you also to my aunt Wangeci, Kevin and Brian for being my Kenyan base

in Oregon. I thank Chris, Seth, Jason and the rest of my Grace City Church family for their love, prayers and constant reminder of what's truly important. Last but definitely not least, thank you Jessica. The last ten months have been utterly phenomenal because of your presence in my life. Your love and support has inspired me to reach and seek far beyond what I once thought possible.

CONTRIBUTION OF AUTHORS

I acknowledge and sincerely thank all those who have contributed in any and all fashions to the work in this thesis. Dr. M.A. Subramanian and Dr. A.W. Sleight have contributed significantly to all the chapters in this thesis. Dr. Hiroshi Mizoguchi contributed to synthesis optimization of powder and single crystal samples in the $\text{Pb}_3\text{Rh}_{7-x}\text{Mn}_x\text{O}_{15}$ solid solution. He also contributed to X-ray diffraction analysis and numerous productive discussions. Dr. Lev Zakharov assisted with the single crystal refinements for the $\text{Pb}_3\text{Rh}_{7-x}\text{Mn}_x\text{O}_{15}$ single crystals grown.

Dr. Jun Li was very helpful with GSAS refinements and the use of the GSAS software. She was also instrumental in Rietveld refinements of the neutron diffraction data in the $\text{Sr}_{1-x}\text{M}_x\text{RuO}_3$ ($M = \text{K}, \text{Rb}, \text{Cs}$) investigation. Dr. Krishnendu Biwas gave much insight on thermoelectricity in oxides and assisted in Seebeck and thermal diffusivity measurements. Dr. James Eilertsen also gave much insight through discussions on thermoelectricity and assisted with specific heat measurements.

Aun-anong Ruanthon assisted with synthesis and characterization of $(\text{RhV})_{1+x}\text{Ti}_{1-2x}\text{O}_6$ phases. She also provided insight on the rutile structure through discussion. Dr. Romain Berthelot contributed to crystal structure refinements in the $\text{Sr}_2\text{Ir}_{1-x}\text{M}_x\text{O}_4$ ($M = \text{Ti}, \text{Co}, \text{Fe}$) investigation. He also assisted with synthesis and characterization of the Co and Fe doped compositions. Discussions with him also provided much insight on the overall investigation.

Dr. Sean Muir contributed to magnetic measurements and analysis of the magnetism in the $\text{Sr}_2\text{Ir}_{1-x}\text{M}_x\text{O}_4$ ($\text{M} = \text{Ti}, \text{Co}, \text{Fe}$) investigation. Discussions with him in this and all investigations have provided significant insight.

TABLE OF CONTENTS

	<u>Page</u>
1 Introduction.....	1
1.1 Oxide Materials.....	1
1.1.1 Transition Metal Oxides	1
1.2 Oxide Structures.....	2
1.3 Oxide Properties.....	4
1.3.1 Electronic Properties	4
1.3.2 Thermoelectric Properties	8
1.3.2.1 Thermal Conductivity	14
1.3.2.2 Oxide Thermoelectric Materials	15
1.3.3 Magnetic Properties	16
1.3.4 Dielectric Properties.....	21
1.3.5 Superconductivity	22
1.4 References.....	26
2 Substitutional studies on the hexagonal structure of $\text{Pb}_3\text{Rh}_7\text{O}_{15}$	28
2.1 Abstract.....	28
2.2 Introduction.....	31
2.1.1 Rhodium Oxides	31
2.2.2 Mixed Valency.....	32
2.2.3 Bond Valence.....	33
2.2.4 Charge Ordering.....	34
2.2.5 The Verwey Transition	35

TABLE OF CONTENTS (Continued)

	<u>Page</u>
2.3	Verwey-Type Transition within the $\text{Pb}_3\text{Rh}_{7-x}\text{Mn}_x\text{O}_{15}$ Solid Solution.....39
2.3.1	Introduction.....39
2.3.2	Results.....41
2.3.3	Discussion.....49
2.3.4	Conclusion.....53
2.3.5	Experimental.....54
2.4	Effects of Bi substitution in $\text{Pb}_{3-x}\text{Bi}_x\text{Mn}_7\text{O}_{15}$56
2.4.1	Introduction.....56
2.4.2	Results and Discussion.....57
2.4.3	Conclusion.....62
2.4.4	Experimental.....62
2.5	References.....63
3	Investigating the thermoelectric properties of compositionally controlled oxide materials.....65
3.1	Abstract.....65
3.2	Introduction.....68
3.2.1	Cation Arrangements in Perovskite Structures.....68
3.2.1.1	B-Site Ordering.....69
3.2.1.2	A-Site Ordering.....74
3.3	Structure-Property relationships in $\text{Sr}_{1-x}\text{M}_x\text{RuO}_3$ (M = K, Rb, Cs) perovskite oxides.....77
3.3.1	Introduction.....77
3.3.2	Results and Discussion.....79
3.3.3	Conclusion.....91
3.3.4	Experimental.....91
3.4	Effect of substitution on the thermoelectric properties of $\text{Sr}_2\text{CoRuO}_6$93

TABLE OF CONTENTS (Continued)

	<u>Page</u>
3.4.1	Introduction.....93
3.4.2	Results and Discussion96
3.4.2.1	Structure.....96
3.4.2.2	Physical Properties.....99
3.4.3	Conclusion107
3.4.4	Experimental.....107
3.5	Investigating the thermoelectric properties of $(\text{RhV})_{1+x}\text{Ti}_{1-2x}\text{O}_6$ phases with the Rutile-type structure.....109
3.5.1	Introduction.....109
3.5.2	Results and Discussion113
3.5.3	Conclusion122
3.5.4	Experimental.....122
3.6	References.....124
4	Structure – Property relationships in the K_2NiF_4 – type structure of Sr_2IrO_4 and Sr_2TiO_4127
4.1	Abstract.....127
4.2	Introduction.....129
4.2.1	Ir and its oxides.....129
4.2.2	K_2NiF_4 Structure133
4.3	Synthesis and characterization of $\text{Sr}_2\text{Ir}_{1-x}\text{M}_x\text{O}_4$ ($\text{M} = \text{Ti}, \text{Fe}, \text{Co}$) solid solutions.....135
4.3.1	Introduction.....135
4.3.2	Results and Discussion138
4.3.2.1	X-Ray Diffraction characterization.....138
4.3.2.2	Physical measurements145
4.3.3	Conclusion151

TABLE OF CONTENTS (Continued)

	<u>Page</u>
4.3.4	Experimental152
4.4	Investigation of the $\text{Sr}_2\text{Ti}_{1-x}\text{Rh}_x\text{O}_4$ solid solution.....154
4.4.1	Introduction.....154
4.4.2	Results and Discussion155
4.4.3	Conclusion160
4.4.4	Experimental160
4.5	References.....162
5	Further Details on Experimental Methods164
5.1	Introduction.....164
5.2	X-ray Diffraction165
5.2.1	Powder X-ray Diffraction – Rigaku Miniflex II Diffractometer166
5.2.2	Single Crystal X-ray Diffraction – Bruker Smart Apex II.....169
5.3	Low Temperature Magnetometry and Resisitivity – Quantum Design PPMS171
5.3.1	Low Temperature Magnetometry172
5.3.2	Low Temperature Electrical Resistivity173
5.4	High Temperature Seebeck and Resisitivity – ZEM-3 Thermoanalyzer175
5.5	Thermal Diffusivity – Netzsch Microflash.....177
5.6	Specific Heat – Mettler Toledo Differential Scanning Calorimeter179
5.7	References.....180
	General Conclusions and Future Work.....181
	Bibliography184

LIST OF FIGURES

<u>Figure</u>	<u>Page</u>
1.1 The electronic band structure of TMOs with metallic, semiconducting and insulating behavior shown.....	5
1.2 The movement positive holes in the valence band and excited electrons in the conduction band of a semiconductor.....	5
1.3 Temperature dependence of the electronic conductivity for metals and semiconductors. At low temperatures, metallic conductivity is no longer linear with temperature and is dominated by the presence of defects.....	7
1.4 Basic schematic of simple setup to show the Seebeck effect of two different materials. Adapted from Basford. [12].....	9
1.5 Figure 1.5. The Seebeck coefficient, electrical resistivity and power factor as a function of density of conduction electrons. Adapted from Mahan [13].....	10
1.6 The Peltier effect between two different materials with the heat flow controlled by the electrical current flow. Adapted from Tritt et al. [11].....	11
1.7 Schematics of a <i>pn</i> couple being used in refrigeration and power generation either application of a voltage difference or thermal gradient respectively. Actual thermoelectric devices are composed of numerous <i>pn</i> couples. Adapted from Mahan[13].....	12
1.8 Plot showing the ZT , thermal conductivity (κ), electrical conductivity (σ) and Seebeck coefficient (α) for insulators, semiconductors and metals as a function of carrier concentration. As can be inferred, highly doped semiconductors make the best candidates for thermoelectric materials. Adapted from [17].....	13
1.9 The prominent magnetic interactions with accompanying detail on their evolution with temperature [31].....	20
1.10 Plot showing the T_c of some known superconductors with their time of discovery. Adapted from [43].....	24

LIST OF FIGURES (Continued)

<u>Figure</u>	<u>Page</u>
1.11 A depiction of the two types of superconductors with the difference being the upper and lower critical field for type II superconductors. Adapted from [44].	25
2.1 The Verwey Transition at 119 K in Magnetite is visible in a number of physical properties of the material include (a) the magnetization, (b) the specific heat and (c) the resistivity. Adapted from [25].	37
2.2 Structure of $\text{Pb}_3\text{Rh}_7\text{O}_{15}$ and $\text{Pb}_3\text{Mn}_7\text{O}_{15}$. Colors of octahedra indicate Rh valencies in $\text{Pb}_3\text{Rh}_7\text{O}_{15}$. Green represents Rh^{3+} in the 8h site, yellow represents $\text{Rh}^{3.5+}$ in the 12i site, cyan represents Rh^{3+} in the 2b site, and dark blue represents Rh^{4+} in the 6f site. b). The hexagonal structure with the Pb atoms shown in two sites within the interlayer region. c). A view along the c-axis of the structure with the interlayer Rh present and d). without the interlayer Rh present.	40
2.3 Cell edges, c/a, and unit cell volume for $\text{Pb}_3\text{Rh}_{7-x}\text{Mn}_x\text{O}_{15}$ phases.	42
2.4 Some interatomic distances (Rh/Mn-O) vs. x for $\text{Pb}_3\text{Rh}_{7-x}\text{Mn}_x\text{O}_{15}$ phases. x < 7 phases are shown in hexagonal symmetry while the x = 7 phase is shown in orthorhombic symmetry.	46
2.5 Resistivity vs. temperature for $\text{Pb}_3\text{Rh}_{7-x}\text{Mn}_x\text{O}_{15}$ phases. Inset shows linear data for the x < 1 phases.	47
2.6 Magnetic susceptibility for $\text{Pb}_3\text{Rh}_{7-x}\text{Mn}_x\text{O}_{15}$ phases. χ_m is calculated in emu/mol.	48
2.7 Pb-O bonding in $\text{Pb}_3\text{Rh}_{7-x}\text{Mn}_x\text{O}_{15}$ phases. Cyan spheres represent O4 atoms. Contraction of a with increasing x causes Pb-O distances in the ab plane to decrease, which is compensated by an increase in Pb-O bond lengths perpendicular to this plane resulting in an expansion of c. The decrease of the O3-Pb1-O3 angle with increasing x also contributes to an increase in c.	51
2.8 The lattice parameter trends for the $\text{Pb}_{3-x}\text{Bi}_x\text{Mn}_7\text{O}_{15}$ phases with x ≤ 0.2.	57

LIST OF FIGURES (Continued)

<u>Figure</u>	<u>Page</u>
2.9 The magnetic susceptibility of $\text{Pb}_{3-x}\text{Bi}_x\text{Mn}_7\text{O}_{15}$ phases with $x \leq 0.2$ showing the dramatically different transitions at ~ 70 K, 40 K and 20 K for the $x = 0.2$ composition.....	58
2.10 The magnetic susceptibility of $\text{Pb}_{2.8}\text{Bi}_{0.2}\text{Mn}_7\text{O}_{15}$ measured at the different fields shown.....	59
2.11 The magnetic susceptibility of the resynthesized $\text{Pb}_{2.8}\text{Bi}_{0.2}\text{Mn}_7\text{O}_{15}$ (sample 2) as compared to the original composition (sample 1) and the $\text{Pb}_3\text{Mn}_7\text{O}_{15}$ composition.....	60
2.12 The electrical resistivity $\text{Pb}_{3-x}\text{Bi}_x\text{Mn}_7\text{O}_{15}$ compositions compared with that of $\text{Pb}_3\text{Rh}_7\text{O}_{15}$	61
3.1 B-site ordering in perovskites. The most symmetric type of ordering is Rock salt ordering and can be considered as 0-Dimensional. Columnar ordering (1-Dimensional) and layered ordering (2-Dimensional) are less symmetric and also less common in B-site ordered perovskites. Adapted from [10].....	70
3.2 A plot of Charge Difference vs. Ionic Radius Difference for stoichiometric double perovskites. The plot shows that the type of B-site ordering observed is primarily influenced by the charge difference between the B cations. The plot is adapted from work by Anderson et al. [14].....	73
3.3 A-site ordering in $\text{AA}'\text{B}_2\text{X}_6$ perovskites. Rock salt, columnar and layered ordering are shown for $\text{AA}'\text{B}_2\text{X}_6$ perovskites. In comparison to B-site ordering, A-site ordering tends to prefer a layered sublattice type over rock salt sublattice type. Adapted from [10].....	75
3.4 Orthorhombic perovskite structure resulting from distortions of the ideal cubic structure when the A cation is smaller than that required for the aristotype cubic structure. Tilting of the BO_6 octahedra is visible in (a) while (b) is a projection along the c -axis showing the rotations of the octahedra.....	78
3.5 XRD patterns of $\text{Sr}_{1-x}\text{M}_x\text{RuO}_3$ ($\text{M} = \text{K}, \text{Rb}, \text{Cs}$) phases. The patterns show that only low solubility can be achieved for all three alkali metals with $x \leq 0.3$ for $\text{Sr}_{1-x}\text{K}_x\text{RuO}_3$ and $x \leq 0.1$ for $\text{Sr}_{1-x}\text{Rb}_x\text{RuO}_3$ and $\text{Sr}_{1-x}\text{Cs}_x\text{RuO}_3$...80	80

LIST OF FIGURES (Continued)

<u>Figure</u>	<u>Page</u>
3.6 The evolution of the <i>a</i> and <i>b</i> cell parameters for the Sr _{1-x} K _x RuO ₃ (a), Sr _{1-x} Rb _x RuO ₃ (b) and Sr _{1-x} Cs _x RuO ₃ (c) phases.....	82
3.7 The evolution of the <i>c</i> cell parameter and cell volume for the Sr _{1-x} K _x RuO ₃ (a), Sr _{1-x} Rb _x RuO ₃ (b) and Sr _{1-x} Cs _x RuO ₃ (c) phases.....	83
3.8 Time of flight neutron diffraction data for the Sr _{0.9} K _{0.1} RuO ₃ composition collected at 10K and 300K. Rietveld refinement statics determined by GSAS software are shown. Data was collected at Oak Ridge National Laboratory.....	84
3.9 Time of flight neutron diffraction data for the Sr _{0.9} Rb _{0.1} RuO ₃ composition collected at 10K and 300K. Rietveld refinement statics determined by GSAS software are shown. Data was collected at Oak Ridge National Laboratory.....	85
3.10 Time of flight neutron diffraction data for the Sr _{0.9} Cs _{0.1} RuO ₃ composition collected at 10K and 300K. Rietveld refinement statics determined by GSAS software are shown. Data was collected at Oak Ridge National Laboratory.....	86
3.11 The molar magnetic susceptibility (χ_m) for the Sr _{1-x} K _x RuO ₃ (a), Sr _{1-x} Rb _x RuO ₃ (b), and Sr _{1-x} Cs _x RuO ₃ (c) phases.....	88
3.12 Evolution of Seebeck coefficient (a) and electrical resistivity (b) with temperature for the Sr _{0.9} M _{0.1} RuO ₃ (M = K, Rb, Cs) phases.....	90
3.13 Crystal structures of SrLaCoRuO ₆ (a) and Sr ₂ CoRuO ₆ (b). In (a) the rocksalt arrangement of the B-site cations in the SrLaCoRuO ₆ structure is shown with each CoO ₆ octahedron (orange in color) isolated from all other CoO ₆ octahedra and each RuO ₆ octahedron (blue) isolated from all other RuO ₆ octahedra. This structure is defined by a monoclinic P2 ₁ /n space group. Disorder on the B-site in Sr ₂ CoRuO ₆ is depicted in (b) with both Co or Ru octahedra represented by green octahedra. This structure is defined by a monoclinic I2/c space group.....	95
3.14 The XRD pattern evolution of the Sr _{2-x} La _x CoRuO ₆ solid solution. The presence of these new peaks at x = 0.5 likely indicates a change in structure from the monoclinic I2/c to P2 ₁ /n structure.....	97

LIST OF FIGURES (Continued)

<u>Figure</u>	<u>Page</u>
3.15 Changes in the lattice parameter evolution with La content. The <i>a</i> and <i>b</i> parameter changes are shown in (a), <i>c</i> parameter changes are shown in (b), cell volume changes in (c) and the <i>c/a</i> ratio evolution in (d).....	98
3.16 The evolution of the Seebeck coefficient (a) and resistivity (b) with temperature.....	101
3.17 The evolution of thermal conductivity (a) and thermoelectric figure of merit (ZT) (b) with temperature.....	104
3.18 The magnetism data for the Sr _{2-x} La _x CoRuO ₆ solid solution. The molar magnetic susceptibility with temperature is shown in (a) and inverse molar magnetic susceptibility with temperature is shown in (b). Plot (c) shows the Curie constant, (d) shows the Weiss constant, and (e) shows the magnetic moment with La content.....	106
3.19 Depiction of the tetragonal P42/mmm (136) rutile structure. In (a) the corner sharing in the <i>ab</i> plane and edge sharing along the <i>c</i> -axis is shown. The structure is displayed along the <i>a</i> , <i>b</i> , and <i>c</i> direction in (b), (c) and (d) respectively.....	110
3.20 XRD patterns of the (RhV) _{1+x} V _{1-2x} O ₆ solid solution with the (hkl) values to show the formation of the tetragonal rutile structure.....	114
3.21 Refined values of the <i>a</i> (black squares) and <i>c</i> (blue circles) cell parameters of the tetragonal unit cell (a), cell volume (b) and <i>c/a</i> ratio (c).....	116
3.22 Electrical conductivity (a), Seebeck coefficient (b) and Thermal conductivity (c) evolution with temperature from 300 – 900K of (RhV) _{1+x} V _{1-2x} O ₆ phases.....	118
3.23 Figure of merit (ZT) of the (RhV) _{1+x} V _{1-2x} O ₆ samples in the 300 – 900 K temperature range.....	119
3.24 The activation energy in eV of the (RhV) _{1+x} V _{1-2x} O ₆ compositions...121	121

LIST OF FIGURES (Continued)

<u>Figure</u>	<u>Page</u>
4.1 Typical flat bottomed Ir crucible used for growth of metal oxide single crystals such as Gadolinium Gallium Garnet (GGG). The crucible pictured has a diameter of 180 mm and a capacity of 4330 ml.....	131
4.2 Depiction of the K_2NiF_4 structure. The green spheres represent the rock salt layers of K separating the blue NiF_6 octahedra which corner share in a similar fashion to BO_6 octahedra in the cubic ABO_3 perovskite structure. The presence of rock salt layers contributes to an extension of the c cell parameter and a tetragonal unit cell.....	134
4.3 Representation of the K_2NiF_4 -type structure for Sr_2MO_4 ($M = Ti, Fe, Co$) in a perspective view (a) and in projection in the (a,b) plane (b). In case of Sr_2IrO_4 , the same latter projection (c) evidences the octahedra tilting $\theta \sim 11^\circ$ around the c axis. Simulated XRD patterns of Sr_2IrO_4 (d) from [14] and Sr_2TiO_4 (e) from [28] are shown for comparison.....	137
4.4 (a) XRD patterns of the entire solid solution $Sr_2Ir_{1-x}Ti_xO_4$ on the whole 2θ range and (b) a focus on the $40 - 48^\circ 2\theta$ region that highlights the transition $I41/acd$ to $I4/mmm$. (c) Refined values of the cell parameters. The a cell parameter has been multiplied by $\sqrt{2}$ for compositions with the Sr_2TiO_4 structure. The dotted and dashed lines highlight the a and c parameter evolutions respectively. The solid line represents the theoretical a parameter evolution in the case of no octahedra tilting (<i>i.e.</i> $I4/mmm$ space group from Sr_2IrO_4 to Sr_2TiO_4).....	140
4.5 XRD patterns of (a) $Sr_2Ir_{1-x}Fe_xO_4$ (up to $x = 0.5$) and (b) $Sr_2Ir_{1-x}Co_xO_4$ (up to $x = 0.4$). (c and d). Weak peak impurities are marked by a * symbol. Evolution of the corresponding cell parameters a (empty circles) and c (black circles). Sr_2FeO_4 and Sr_2CoO_4 values (star) are taken from the literature [29,30]. The dashed lines (in c and d) show that the c parameter evolution can be split into two linear regions with distinct slopes around $x = 0.4$ and may then linearly decrease to the Fe and Co end members...	143
4.6 Magnetic molar susceptibility (a), molar susceptibility as per emu per mol of Ir^{4+} near the Curie transition temperature (b), magnetization versus magnetic field between -5 and 5 Tesla at 5 K (c), and electrical resistivity (d) evolution in temperature from 5 to 300 K of $Sr_2Ir_{1-x}Ti_xO_4$ samples. Sr_2IrO_4 resistivity data are taken from a previous work [16]. In case of the pure Sr_2TiO_4 , too high resistivity prevented four probe measurements..	148

LIST OF FIGURES (Continued)

<u>Figure</u>	<u>Page</u>
4.7	Magnetic susceptibility (a) evolution in temperature from 5 to 300 K of $\text{Sr}_2\text{Ir}_{1-x}\text{Fe}_x\text{O}_4$ (x up to 0.5) and refined values for Weiss constant, Curie Constant and effective moment (b) for the same compositions.....149
4.8	Magnetic susceptibility (a) evolution in temperature from 5 to 300 K of $\text{Sr}_2\text{Ir}_{1-x}\text{Co}_x\text{O}_4$ (x up to 0.3) and refined values for Weiss constant, Curie Constant and effective moment (b) for the same compositions. Note that the weak presence of Co_3O_4 for the composition $\text{Sr}_2\text{Ir}_{0.7}\text{Co}_{0.3}\text{O}_4$ was not detected by XRD.....150
4.9	XRD patterns of single phase $\text{Sr}_2\text{Ti}_{1-x}\text{Rh}_x\text{O}_4$ ($x \leq 0.6$) compositions.....157
4.10	Refined lattice parameters of the $\text{Sr}_2\text{Ti}_{1-x}\text{Rh}_x\text{O}_4$ phases showing relatively little change in the <i>a</i> cell parameter with Rh substitution, however, a change from a positive to negative slope at the $x = 0.2$ composition can be observed as shown by the dashed line. This is likely related to octahedral rotation occurring with Rh substitution. The <i>c</i> cell parameter shows an increase with substitution.....157
4.11	The <i>c/a</i> ratio of the refined $\text{Sr}_2\text{Ti}_{1-x}\text{Rh}_x\text{O}_4$ phases. A clear change in slope is observed at the $x = 0.2$ composition which is likely related to octahedral rotation occurring.....158
4.12	The magnetic susceptibility evolution with temperature of the $\text{Sr}_2\text{Ti}_{1-x}\text{Rh}_x\text{O}_4$ phases. All phases show paramagnetic behavior however, high susceptibilities are observed with increasing Rh content.....159
4.13	The electrical resistivity evolution with temperature of the $\text{Sr}_2\text{Ti}_{1-x}\text{Rh}_x\text{O}_4$ phases. All phases show semiconducting behavior however, a transition to metallic conductivity is expected if higher Rh content can be successfully substituted as Sr_2RhO_4 has been found to be metallic [39].....159
5.1	Bragg's law relationship depicted by identical incident X-ray beams of equal wavelength being scattered by atoms on different planes of crystalline material. The lower beam travels an extra $2d\sin\theta$ distance with constructive interference resulting when this extra distance equals $n\lambda$. Image is adapted from [1].....166

LIST OF FIGURES (Continued)

<u>Figure</u>	<u>Page</u>
5.2 Origin of $K\alpha$ radiation. The electron beam excites the atom leading to a core electron being emitted. An electron on the L-shell drops to the K-shell to fill the vacancy and return the atom to the ground state. As the L-shell electron drops into the lower energy K-shell, $K\alpha$ radiation is emitted.....	168
5.3 Rigaku Miniflex II diffractometer system. The Haskris water recirculator (a) allows for the instrument (b) to function without the X-ray tube shown in (c) overheating.....	169
5.4 The Physical Property Measurement System by Quantum Design. A multiplatform workstation allowing for low temperature magnetometry and electrical resistivity measurement.....	171
5.5 A schematic showing the dimensions of the ACMS coil set and tube assemblage (a) [6]. (b) shows a typical powder sample packed in a polycarbonate capsule which is then packed into a polycarbonate straw using cotton.....	173
5.6 The resistivity puck allowing low temperature electrical resistivity measurements of the samples simultaneously numbered on the puck circuit board (a). The puck is connected to the instrument via a 12-pin connection at the base of the puck (b). The samples are measured via the four-probe method (c).....	174
5.7 The ULVAC-RIKO ZEM-3 Thermoanalyzer set-up (a). Inside the furnace chamber the sample is held in place by Ni electrodes and Pt probes (b).....	176
5.8 An external view of the The Netzch Microflash (a) and schematic view of the instrument design from [8]. The sample carrier and infrared detector fins are shown in (c).....	178
5.9 The Mettler Toledo DSC (a) with the sample and reference placed in pans that sit on two separate heater in the general furnace area (b).....	179

LIST OF TABLES

<u>Table</u>	<u>Page</u>
2.1 Summary of Crystallographic Results	43
2.2 Atomic coordinates and isotropic displacement factors ($\text{\AA}^2 \times 10^3$).	44
2.3 Site percentage (%) occupied by Rh for the four octahedral sites.....	44
2.4 Interatomic distances in \AA	45
2.5 Summary of magnetic susceptibility measurements for $\text{Pb}_3\text{Rh}_{7-x}\text{Mn}_x\text{O}_{15}$ phases.....	49
3.1 Three common arrangements of B cations in perovskite oxides. A comparison of the cell parameters, crystal systems and common space groups is shown, with a_c representing the unit cell parameter of the ideal cubic ABX_3 perovskite structure.....	72
4.1 Structure types and unit cell dimensions of some Ir(IV) oxides. Adapted from [6].....	132
4.2 Structural data at 300 K comparing Sr_2IrO_4 and Sr_2RhO_4 . Adapted from [15]	154

This thesis is dedicated to
my parents and grandparents.

Your faith in me and sacrifice for me has allowed me
to soar to heights I never thought possible.

Thank you!

STRUCTURE-PROPERTY RELATIONSHIPS IN OXIDES CONTAINING SELECT PLATINUM GROUP METALS.

CHAPTER 1

INTRODUCTION

1.1 Oxide Materials

The term “oxide material” encompasses a wide range of inorganic materials. These materials possess a great variety of structures, properties and applications. This wealth of structures, properties and resulting applications is briefly discussed in the following sections and has provided the underlying motivation for the research endeavors detailed in this thesis. More specifically, oxide materials of transition metals are focused on.

1.1.1 Transition Metal Oxides

Transition metal oxides (TMOs) can be described as oxide compounds containing at least one element between Ti and Zn in the 3d series, between Zr and Cd in the 4d series, or between Hf and Au in the 5d series. These TMOs tend to be highly stable with a wide range of properties. The range in electronic properties is especially notable including insulators like TiO_2 , semiconductors like Mn_{1-x}O , metals like LaTiO_3 and superconductors like $\text{YBa}_2\text{Cu}_3\text{O}_7$. The magnetic properties of TMOs are equally as diverse (involving paramagnetism, ferromagnetism, ferrimagnetism, antiferromagnetism and diamagnetism). Furthermore, coupling of these electric and magnetic properties is also prevalent in TMOs leading to the

realization of coupled-properties such as magneto-capacitance, magneto-resistance, and multiferroicity [1,2].

However, what makes TMOs truly special is that they can be tailored to specific applications by subtle distortions of the coordination environments of ions, or changes in elemental composition. This is the general goal of solid state chemistry research, to optimize or realize new properties via structure modification.

The work detailed in this thesis focuses on the characterization of oxide materials that have been altered in structure via synthesis methods and/or elemental composition. Specifically, $\text{Pb}_3\text{Rh}_7\text{O}_{15}$ phases, perovskite SrRuO_3 and SrLaCoRuO_6 phases and tetragonal Sr_2IrO_4 phases are discussed and used as parent materials in the search and study of new crystal structures and resulting novel phenomena. An initial brief overview of oxide structures and properties will allow later extensive discussions on the synthesis, structure and characterization of the “tuned” oxide materials.

1.2 Oxide Structures

A fundamental understanding of oxide structures is necessary for further study of investigations involving tuning of their structure and describing the resulting properties. An understanding of oxide structures begins with an understanding of how the cations and oxygen anions stack to form the crystal structure. Two forms of stacking are most commonly observed. These are cubic close packing and hexagonal close packing and are

best understood by assuming cations and anions will have a spherical-like shape.

Cubic close packing involves an ABCABC... repetitive stacking sequence for either the anions or cations (usually the anions). This leads to a packing fraction of 74.05% and a layer stacking perpendicular to the [111] direction. This tends to result in structures with cubic symmetry. Hexagonal close packing on the other hand involves an ABABAB... repetitive stacking sequence and also leads to a packing fraction of 74.05%. This tends to result in structures with hexagonal symmetry.

Usually in oxide structures, the oxygen anions stack in one of these fashions and the stacking results in voids that the cations will occupy. Most common are octahedral and tetrahedral voids. This is the general basis for a number of common structures oxides adopt. These include the rock salt structure that has cubic symmetry with cubic close packing of the anions while the cations fill all the octahedral voids. An example of an oxide possessing this structure is LiCoO_2 which is extensively used in Li – ion batteries [3]. Another common oxide structure is the rutile structure involving hexagonal close packing and tetragonal symmetry. TiO_2 is an example of this oxide which is heavily used in the making of paints [4]. A derivative of the rocksalt structure is the perovskite structure which involves cubic close packing similar to the rocksalt structure but only $\frac{1}{4}$ of the octahedral voids are filled and in addition a third ion in the twelve coordinate site at the center of

the unit cell is present. Perovskite structures are very common and a good example is BaTiO_3 , a well known dielectric used in capacitors [5].

1.3 Oxide Properties

As alluded to earlier, oxide materials possess a wealth of properties of with new properties continually being discovered [6]. The following sections will give a brief foundational description to a number of these properties that will allow deeper discussions in the investigations covered later. Electronic, thermoelectric, magnetic, dielectric and superconducting properties are highlighted.

1.3.1 Electronic Properties

In investigating electronic phenomena, solid state chemists tend to consider both the applications in which the material will be used while being able to understand the effects of structure, composition, and eventual setting relating to electrical behavior. For the most part, the electronic properties of TMOs can be predicted and manipulated to with an understanding of structure-property relationships.

The first thing to keep in mind is that the magnitude of electrical conduction is strongly correlated to the number of electrons available for participation. This in turn is dictated by the occupation of electronic states, their specific arrangement and the presence of atomic interactions. Collectively these factors influencing the conduction are generally referred to

as the band structure. This band structure results by combining of the atomic orbitals of a very high number of atoms in solids resulting in molecular orbitals that are more like bands when their energies are considered.

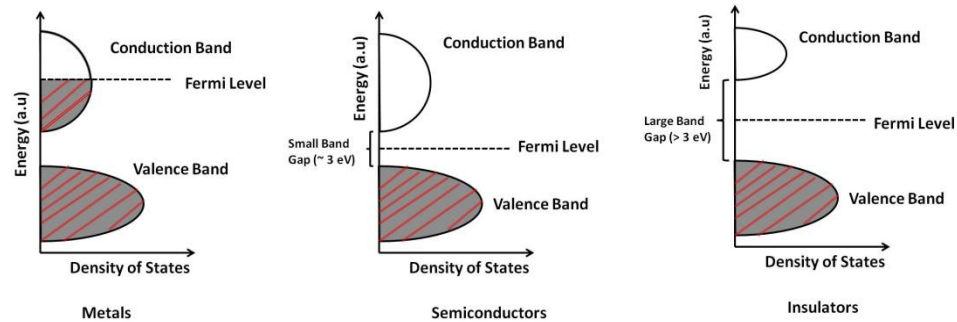


Figure 1.1. The electronic band structure of TMOs with metallic, semiconducting and insulating behavior shown.

Insulators tend to be ionic or strongly covalent, and thus the valence electrons are tightly bound to the atom which is described as high electron localization. Semiconductors on the other hand, are predominantly covalent and have valence electrons that are weakly bound to the atoms meaning they are free to move up to the conduction band with some appropriate thermal excitation. In doing so, positive holes are left in the valence band and these will move as electrons enter them. This is depicted in fig 1.2 below.

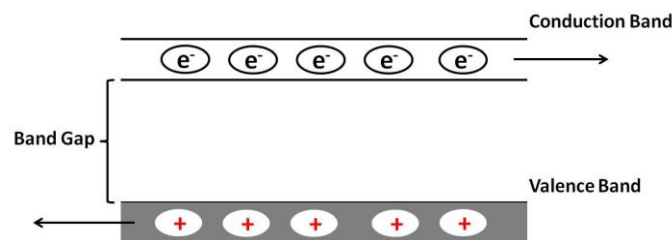


Figure 1.2. The movement positive holes in the valence band and excited electrons in the conduction band of a semiconductor [7].

Consideration of an ideal solid at absolute zero (0 Kelvin) allows these distinctions between the types of conductors to be made even clearer. In a metal, the conduction band is partially filled as shown in figure 1.1. The highest filled level at 0 K is the Fermi level and the corresponding energy is the Fermi Energy. In metals, electrons in singly occupied states close to the Fermi energy are mobile and are responsible for the high conductivity [7].

In semiconductors and insulators, there will be a lack of an overlap and there will be a forbidden gap in the band structure (forbidden as there are no states for electrons to occupy) called the band gap (figure 1.1). In semiconductors this gap is usually less than 3 eV but exceeds this number in insulators such as diamond with a band gap of 6 eV [7].

The effect of temperature also helps distinguish the types of conduction further. Metals become less conducting with increasing temperature due to lattice vibrations which are limiting for the movement of carriers. On the other hand, insulators and semiconductors become more conducting with increasing temperatures due to thermal excitations of electrons through the band gap into the empty conduction band. Semiconductors specifically, which have smaller band gaps than insulators show a larger increase in conductivity [7,8]. These trends with temperature are illustrated in figure 1.3. For metals, at very low temperature, the relationship with temperature stops being linear and the presence of defects dominates the electrical resistivity.

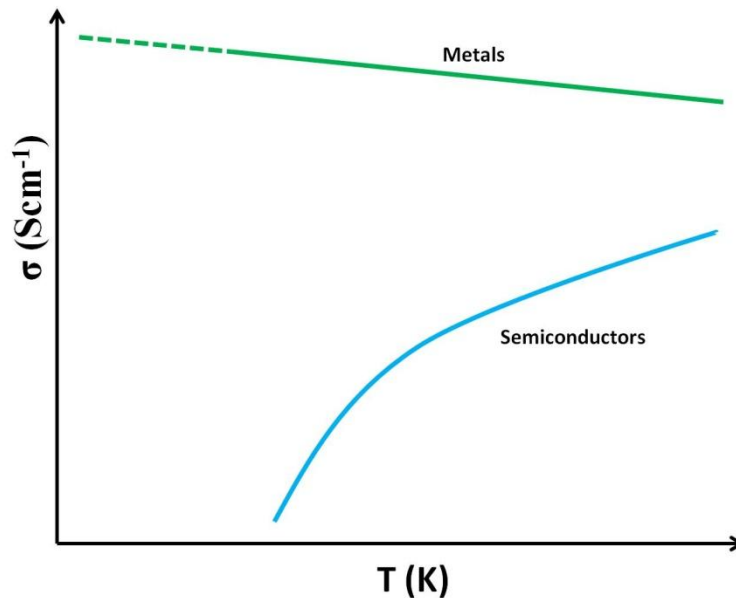


Figure 1.3. Temperature dependence of the electronic conductivity for metals and semiconductors. At low temperatures, metallic conductivity is no longer linear with temperature and is dominated by the presence of defects.

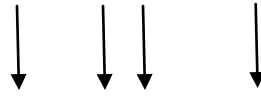
Mathematically, an Arrhenius plot of $\ln\sigma$ vs. $1/T$ can be used to show the difference in temperature dependence of metals, semiconductors and insulators as shown in figure 1.3. This plot is derived from the mathematical expression for electronic conductivity,

$$\sigma = \sigma_0 \exp \frac{E_a}{k_B T}$$

with σ_0 being a constant, E_a being the activation energy of the conductivity, k_B the Boltzmann's constant of 8.617×10^{-5} eV/K and T the temperature in Kelvin.

When the natural logarithm is applied to this equation, the Arrhenius plot is derived with E_a as the slope of the straight line plot of $\ln\sigma$ vs. $1/T$ and $\ln\sigma_0$ as the y-intercept. This is shown below.

$$\text{Ln } \sigma = \frac{Ea}{k_B} \frac{1}{T} + \text{Ln } \sigma_o$$



$$y = (m)x + b$$

1.3.2 Thermoelectric Properties

Continuous ongoing demand for the reduction of fossil fuel dependence, particularly foreign oil in the U.S., and an improvement of alternative energy technologies, has led to a peaked interest in thermoelectric materials by the materials community [9]. In the U.S., this strong call for alternative energy sources has been well exemplified by recent initiatives by policy makers and has allowed for a wealth of ongoing research initiatives into alternative energy sources to meet national demand [10].

Current alternatives to fossil fuel energy include geothermal, solar, wind and hydroelectric energy. Furthermore, materials research has discovered and developed additional renewable sources with thermoelectrics being perhaps the best known of these materials. Thermoelectric devices incorporate these thermoelectric materials. They are designed to generate electrical energy from the presence of a thermal gradient or vice versa. Current and possible future applications of these devices include industrial waste, automobile, geothermal and solar heat recovery. In addition thermoelectrics have been proposed as components of future computer

processors where they could serve as complementary metal oxide semiconductors (CMOS) and boost processing speeds up to 200% [11].

To understand the origins of the energy conversion in thermoelectrics we begin with an overview of the Seebeck effect. This was discovered in the early 1800s when it was found that a thermal gradient across the junctions of two dissimilar materials created a voltage that was proportional to the thermal gradient as depicted in figure 1.4. Thus, the Seebeck coefficient (α) is the ratio of a voltage generated for a temperature difference where, $\alpha = \Delta V / \Delta T$. This is an intrinsic property of the material.

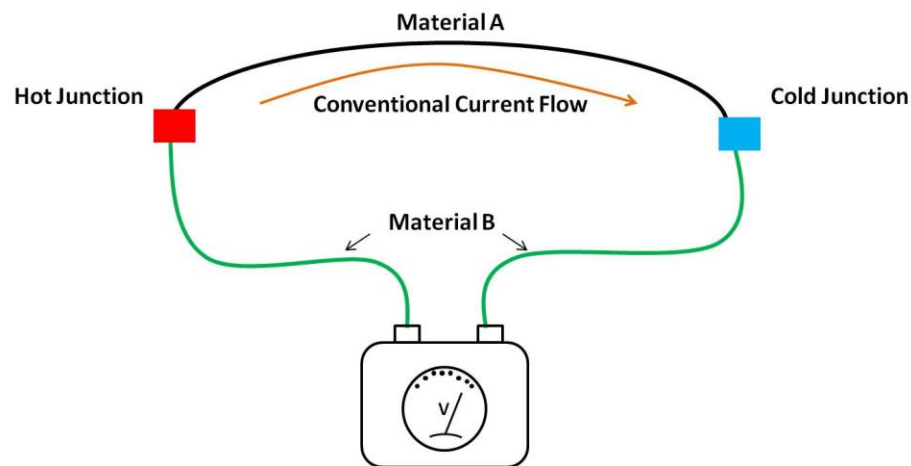


Figure 1.4. Basic schematic of simple setup to show the Seebeck effect of two different materials. Adapted from Basford. [12].

In comparing different types of electronic materials as thermoelectrics, metals tend to have relatively low Seebeck coefficients, a few $\mu\text{V}/\text{K}$, whereas semiconductors and insulators can have Seebeck coefficients of several hundred $\mu\text{V}/\text{K}$. This observation is related to the density of conducting electrons present within the materials. The Seebeck coefficient will decrease

with increasing density of conducting electrons. Metals with high densities of conducting electrons will thus show lower Seebeck coefficients, while insulators and semiconductors with lower densities of conducting electrons will show higher Seebeck coefficients. The density of conduction electrons also influences the electrical conductivity and hence Power factor ($\alpha^2\sigma$) as shown in the figure 1.5 below.

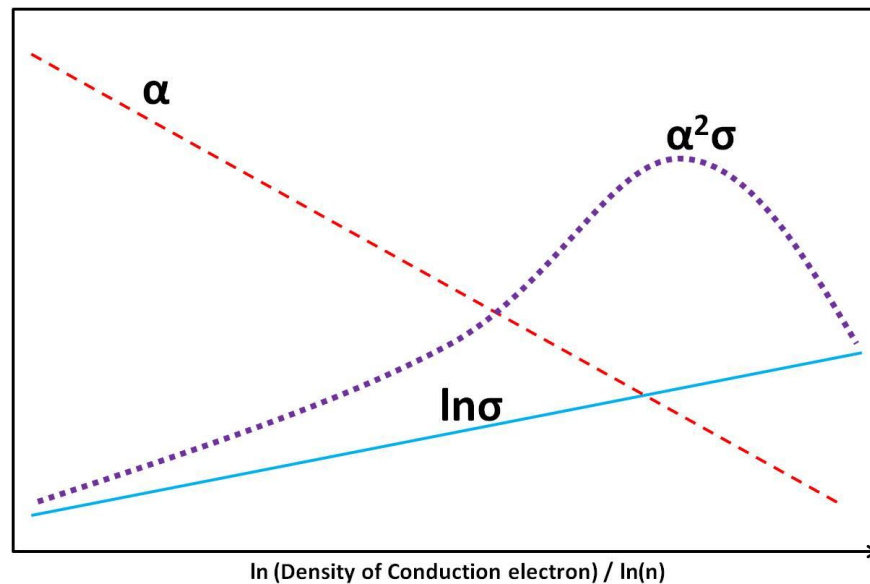


Figure 1.5. The Seebeck coefficient, electrical resistivity and power factor as a function of density of conduction electrons. Adapted from Mahan [13].

The Seebeck coefficient allows us to analyze the majority charge carriers in a particular material. A material with a positive Seebeck coefficient indicates holes are the dominant carrier and is labeled as p-type material while one with a negative Seebeck coefficient indicates electrons as the dominant carriers and is labeled as a n-type material.

Common applications of the Seebeck phenomena is in temperature measurement as thermocouples [14]. These involve two conductors of known

thermal characteristics and temperature differences between the two materials being determined from previously calibrated voltages.

Also vital in understanding thermoelectric mechanisms is the Peltier effect. Soon after the Seebeck effect was discovered, it was found that with an applied electrical current at the junction of two dissimilar materials, heat was either liberated or absorbed depending on the direction of the current flow. This is depicted in figure 1.6 below.

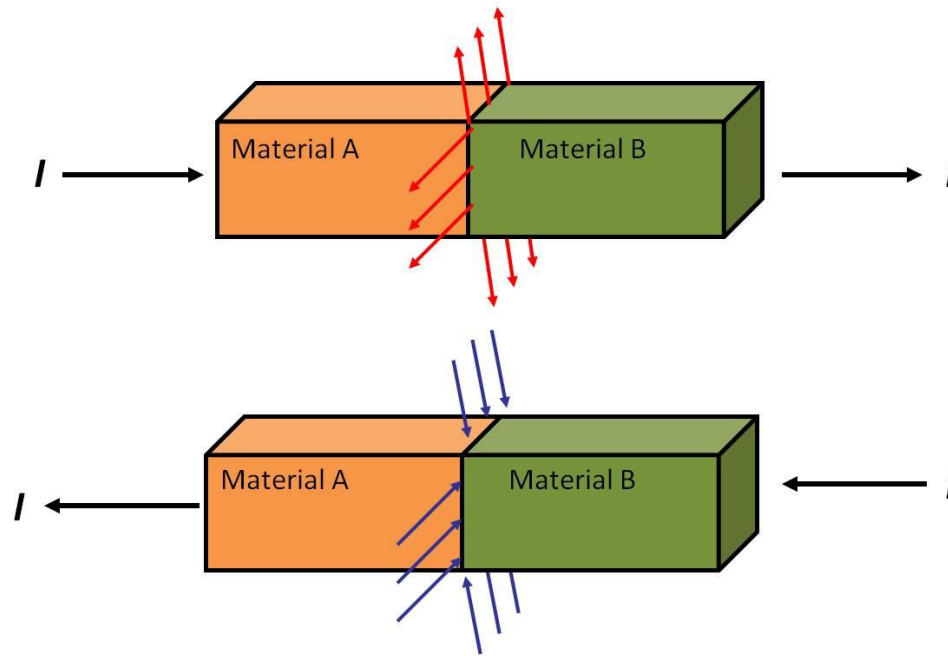


Figure 1.6. The Peltier effect between two different materials with the heat flow controlled by the electrical current flow. Adapted from Tritt et al. [11].

Mathematically, the interrelation between the Peltier and Seebeck effects are described by the Peltier coefficient equation,

$$\Pi = \alpha T$$

where Π is the Peltier coefficient.

This interrelationship allows us to then understand how thermoelectric materials are incorporated into thermoelectric devices. Actual devices require both p-type and n-type materials set-up in a fashion referred to as a *pn* couple. The current flow will determine if the couple and overall device will be used for refrigeration or power generation. This is shown in figure 1.7.

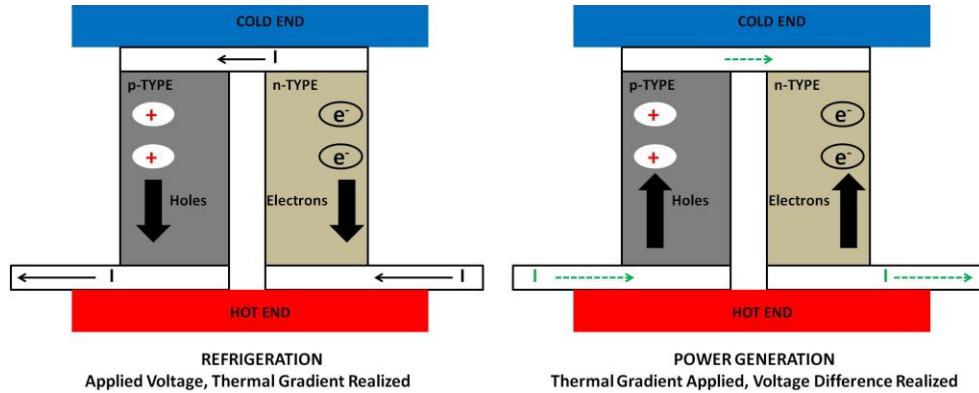


Figure 1.7. Schematics of a *pn* couple being used in refrigeration and power generation either application of a voltage difference or thermal gradient respectively. Actual thermoelectric devices are composed of numerous *pn* couples. Adapted from Mahan [13].

Nonetheless in order to truly gauge the potential or efficiency of a material as a thermoelectric, a dimensionless figure of merit denoted as ZT is used. This is defined as,

$$ZT = \frac{\alpha^2 \sigma T}{\kappa} = \frac{\alpha^2 T}{\rho \kappa}$$

where k is the total thermal conductivity (electronic and lattice, thus $k = k_e + k_l$). A brief discussion on this is in a following section. As can be seen from the ZT expression above, the efficiency of a thermoelectric can be increased with higher Seebeck coefficients and conductivities and lower thermal conductivity. As elementary as this may sound it continues to be a significant

stumbling block for researchers in the field as the properties are interrelated in a way that makes it difficult to synthesize a material with $ZT > 1$. Instead, what tends to be seen is that higher conductivities will be coupled with lower Seebeck coefficients and higher thermal conductivities (driven by higher electronic contributions).

Good thermoelectric materials have been found to possess properties of both metals and insulator that tend to be found in highly doped semiconductors. This is well represented in figure 1.8. It should be noted that current technologies require a $ZT > 1$ for worthwhile efficiencies and power conversion to occur and as of the writing of this work, this continues to be difficult to attain for many types of materials, especially oxides [15,16]. Oxide thermoelectric materials will be briefly discussed in a later section.

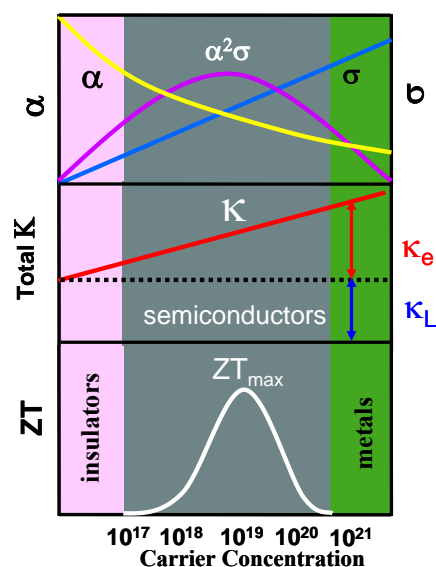


Figure 1.8. Plot showing the ZT , thermal conductivity (κ), electrical conductivity (σ) and Seebeck coefficient (α) for insulators, semiconductors and metals as a function of carrier concentration. As can be inferred, highly doped semiconductors make the best candidates for thermoelectric materials. Adapted from [17].

1.3.2.1 Thermal Conductivity

Crucial to the efficiency of a thermoelectric material is a low thermal conductivity. This property is composed of an electronic and lattice component. The electronic component originates from the transportation of heat by electron and hole carriers. The lattice component on the other hand originates from phonons travelling through the lattice.

It has been suggested that thermoelectric materials should have thermal conductivities approaching those of amorphous materials (~ 0.1 W/m.K) [13]. The most common approach in attempting to attain these low thermal conductivities is by decreasing the lattice thermal conductivity. In fact, the ideal thermoelectric is referred to as a “Phonon-Glass Electron-Crystal” [18]. This description corresponds to a high electrical conductivity and high Seebeck coefficient (electron-crystal) yet low lattice thermal conductivity (phonon-glass).

However a number of challenges result in developing this ideal material. One of the most prominent issues is the interrelation of the properties, particularly the electronic thermal conductivity and the electrical conductivity. This relationship is defined by the Wiedemann-Franz law,

$$k_e = L\sigma T = \eta e \mu L T$$

where L is the Lorenz factor, $\sim 2.4E-8$ J²K⁻²C⁻² for free electrons [19]. It should be noted that the Lorenz factor can vary significantly. For example, it has been observed to vary by as much as 20% in low carrier concentration materials [20].

Nonetheless, research has shown that for the most part, there are guidelines a materials chemist can follow to limit thermal conductivity as they strive to design the ideal thermoelectric material [13]. Elements of a high atomic weight will have smaller phonon energies, lower speeds of sound and lower intrinsic thermal conductivity such as Bi, Te and Pb. Incorporating these into your material is usually a good start for lowering the thermal conductivity. Complex crystal structures involving a large number of atoms per unit cell increase the optical modes that carry little heat as opposed to the acoustic modes. Alloying will also decrease the thermal conductivity. Unfortunately it will also decrease the mobility of the carriers, however, the thermal conductivity tends to be decreased faster than the mobility when alloying is involved. The introduction of impurity atoms that can rattle in caged structures like skutterudites has shown decreased thermal conductivity [21]. Other methods including novel synthesis techniques including milling and leading to substructuring and nanostructuring have also shown decreased thermal conductivity [22].

1.3.2.2 Oxide Thermoelectric Materials

Although the concept of an oxide thermoelectric material was seen as highly favorable particularly due to their tendency to have high thermal stability, great oxidation resistance and be generally non-toxic; it was not until Terasaki et al [23] discovered the high power factor of NaCo_2O_4 while investigating bronze-type oxides for superconductivity, that oxide

thermoelectrics became a serious focal point of thermoelectrics research. Other oxides showing significant thermoelectric properties involving Co in layered “misfit” structures such as $\text{Ca}_3\text{Co}_4\text{O}_9$ and $\text{Bi}_2\text{Sr}_3\text{Co}_2\text{O}_y$ soon followed [24]. The staggered layered structure was found to be essential in lowering thermal conductivity by disrupting the propagation of phonons through the lattice.

However skepticism of the feasibility of oxide thermoelectrics still persists. This originates from the tendency of oxides to be highly ionic which means narrow band widths (conduction band widths) as a result of the weak orbital overlap. This in turn leads to strong polarization of the interatomic bonds that localizes conduction electrons with lower mobilities [16,25]. Even so, research within this field still highly active and fair deal of optimism is present [26].

1.3.3 Magnetic Properties

It is believed that the first true use of magnetism was by the Chinese in primitive compasses where a splinter of Iodestone (magnetite/ Fe_3O_4) floated on water and always pointed north [27]. Today, modern luxuries comprised of magnetic materials include computer memories, T.Vs, medical equipment, generators and transformers. Nonetheless, there continues to be a large effort to understand and discover novel materials with novel magnetic properties. In accordance with this, the variety of oxidation states found in transition metals

make them prime candidates for magnetic oxide materials research. Of particular importance as will be seen in this section are the interactions between the electrons in TMOs.

Magnetic properties are largely dependent upon the materials interaction with an external field. This is described by the following series of equations:

$$B = H + 4\pi I$$

showing that the field strength within the sample (B) is a function of the applied magnetic field (H) and the intensity of the magnetization (I). I/H is the magnetic moment per unit volume and is referred to as the volume susceptibility (χ). Applying this to the field strength expression above leads to:

$$\mu = \frac{B}{H} = 1 + 4\pi \frac{I}{H} = 1 + 4\pi\chi$$

where μ is described as the magnetic permeability. The above expression involves extrinsic magnetic properties and can be converted to intrinsic magnetic properties by the following equation,

$$\chi_m = \chi \frac{F_w}{\rho}$$

with χ_m representing the molar susceptibility which is an intrinsic property, F_w the formula weight and ρ the density. Based on the behavior of the susceptibility as a function of temperature, most materials can be assigned to a specific family of magnetic materials [28–30].

Most elementary understandings of magnetism relate the magnetic moments associated with individual electrons with regards to spin and orbit to the magnetic phenomena observed. The Pauli exclusion principle and Hund's

rule stipulate that no two electrons can have the same quantum numbers (i.e principle, azimuthal, magnetic and spin projection). Thus for a specific orbital, there can only be two electrons and when filled, only one electron may exist in the spin up or spin down orientation.

When all the orbitals are paired, the atom is said to be diamagnetic. When a diamagnetic material is placed in magnetic field, the material will show a repulsive force, and because of this resistance towards the applied field it shows a minute negative magnetization.

When unpaired electrons are present, an atom is said to be paramagnetic. In the absence of the magnetic field, the magnetic moments point in random directions, but with a field present, some of the moments align preferentially to the applied field direction. This enhances the magnetic flux density, which refers to the magnetic field strength within the sample. The resulting net magnetization leads to a positive magnetic susceptibility. It should be noted that both diamagnetic and paramagnetic materials are classified as non-magnetic as in the absence of a magnetic field they show no net magnetization.

In other materials however, the magnetic moments of distinct atoms or ions may be strongly correlated with spontaneous alignment occurring in the absence of an external applied field. These regions possessing spontaneously aligned moments are referred to as domains. Within ferromagnetic materials, the alignment of the moments (or electron spins) is all in the same direction,

while for antiferromagnetic materials, the moments align in an antiparallel fashion.

Magnetic susceptibility behavior is a function of temperature. Below certain critical temperatures, spontaneous alignment of spins occurs observed by a magnetic susceptibility transition. Above the transitions, the materials tend to be paramagnetic and can be described by the Curie-Weiss law,

$$\chi_m = \frac{C}{(T - \theta)}$$

with C as the Curie constant and θ as the Weiss constant. When the law is obeyed in the high temperature paramagnetic region, a plot of the inverse susceptibility as a function of temperature yields a straight line with the Curie constant as the slope and the Weiss constant as the x-intercept. Thus information regarding the majority interactions can be deduced. The Curie constant allows calculation of the magnitude of the moment. This is usually an approximation depending on the nature of the material,

$$\mu = \sqrt{\frac{3kC}{N_A}} = 2.84\sqrt{C} \mu_B \quad \text{for spin only approximation}$$

$$\mu = g_J \sqrt{[J(J+1)]} \mu_B \quad \text{for a more accuracy (required for Lanthanides)}$$

where g is the the gyromagnetic ratio, a ratio of the magnetic dipole moment to its angular momentum of a particle (~ 2). It should be noted that the Weiss constant is an indication of the short range interactions between adjacent atoms. With a $\theta = 0$, paramagnetism is suggested. For a $\theta < 0$, short range antiferromagnetic interactions are suggested while for a $\theta > 0$, short range ferromagnetic interactions are suggested. A summary of these magnetic

interactions as well as their dependence with temperature is depicted in figure 1.9.

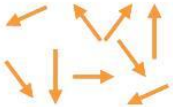
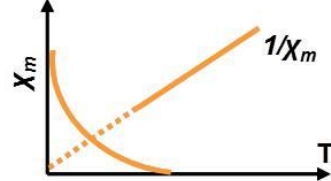
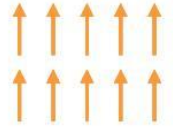
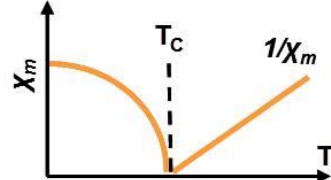
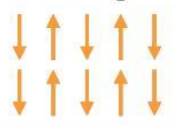
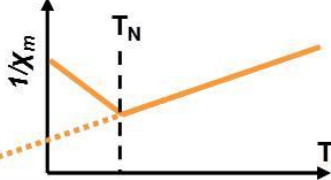
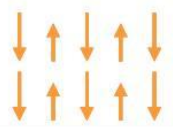
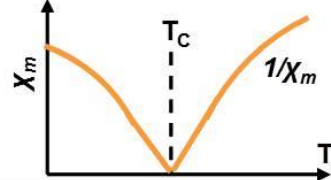
Classification & orientation of magnetic moments	Critical temperature	Magnitude of χ_m	Temperature dependence of χ_m
Diamagnetic	None	-10^{-6} to -10^{-5}	
Paramagnetic 	None	10^{-5} to 10^{-3}	
Ferromagnetic 	T_c Curie Temp. $\chi_m = C/(T - \theta)$	Large below T_c	
Anti - Ferromagnetic 	T_N Neel Temp. $\chi_m = C/(T \pm \theta)$	10^{-5} to 10^{-3}	
Ferrimagnetic 	T_c Curie Temp. $\chi_m \approx C/(T - \theta)$	Large below T_c	

Figure 1.9. The prominent magnetic interactions with accompanying detail on their evolution with temperature [31].

The future of magnetism research appears to be bright. Devices known as Spintronics are currently under heavy investigation, as they seek to take

advantage of not only the charge of the electron but also the spin of the electron in order to produce faster processing speeds in electronics. These rely on materials popularly referred to as multiferroics as they possess at least of two of either of the following: ferromagnetism, ferroelasticity or ferroelectricity. As elementary as this may sound, it is very difficult to couple two of these properties in a material as they tend to require different amounts of d electrons (usually one requiring no d electrons while the other requiring d electron presence). Lastly Giant Magnetoresistance (GMR), involving a large change in electrical resistance resulting from an applied field, is also a field of extensive magnetic research and has potential applications in hard drive storage capacity [32,33].

1.3.4 Dielectric Properties

Dielectric materials are commonly used in the electronics industry where they serve as substrates, separators, capacitors and other important functions [34]. Dielectric materials are insulators, thus possess charges that do not have a propensity to move easily and instead form islands of charge.

In characterizing dielectric materials, the Dielectric constant and loss allow quantification of a dielectric material's ability to store a charge relative to a vacuum. These measurements thus allow for a comparison of different dielectric materials. TMOs tend to have dielectric constants.

Factors affecting the dielectric constant include temperature, frequency, bonding, crystal structure and defects [7,8]. The magnitude of the

Dielectric constant depends on the degree to which a material polarizes or the amount of charge displacement that occurs. On the other hand, the Dielectric loss is defined as the phase lag that leads to an electrical energy loss in dielectric materials and this energy is either directly lost or absorbed by the material in form of heat.

1.3.5 Superconductivity

Superconductivity continues to be an area of great interest among materials community. It continues to be a field in which most would agree that there are still a lot of new discoveries to be made as well as voids in conceptual understanding to be filled. In fact, determining the exact origins of superconductivity in a given material is not as elementary as it may initially sound. Even the most current explanations of superconductivity are still theories and their predictions and boundaries continue to be broken and expanded. The most widely known of these theories is the Bardeen-Cooper-Schrieffer (BCS) theory [35]. According to BCS theory, superconductivity arises from attraction between electron pairs (Cooper pairs) in momentum space that results from electron-phonon coupling within a material.

What is commonly agreed on is the resulting phenomena that allow identification of superconductivity. A superconductor will show zero electrical resistance and also exclude magnetic fields from within (thus show perfect diamagnetism). As one would expect, measuring zero resistance is very difficult as connecting leads and other instrumental parts of measuring

equipment will possess some resistance. Nonetheless a steep drop in the electrical resistivity is usually noticed once a material's critical temperature (T_c) is reached and it becomes superconducting. The exclusion of magnetic flux by a superconductor is known as the Meissner effect [36]. It allows for testing of superconductivity and also allows for a wealth of possible current and future applications of superconductors such as MRI equipment and possibly in Submarine stealth devices [37].

The first report of superconductivity is credited to Kamerlingh Onnes in 1911 who found that Hg was superconducting at 4K [38]. Investigators then began to find superconductivity in Niobium containing materials such as NbN, Nb₃Sn and Nb₃Ge. This apparent Nb requirement together with the BCS T_c limit of 30 K was shattered in 1986 when Müller and Bednorz at IBM working on materials previously made by Michel and Raveau discovered superconductivity in the La_{2-x}Ba_xCuO₄ system [39]. Also of great significance was work by Paul Chu and others that discovered the phenomenon in YBa₂Cu₃O₇, which had a T_c around 93 K, thus exceeding the liquid nitrogen barrier of 77 K [40]. Further higher T_c materials, all with CuO₂ sheets (cuprates), were discovered, raising the T_c to close to 135 K under ambient conditions by the mid 1990s [41]. The last 15 years have seen further understanding of superconductivity with new non-cuprate superconductors such as LaFeAsO_{1-x}F_x being discovered [42]. Figure 1.10 illustrates these historical discoveries.

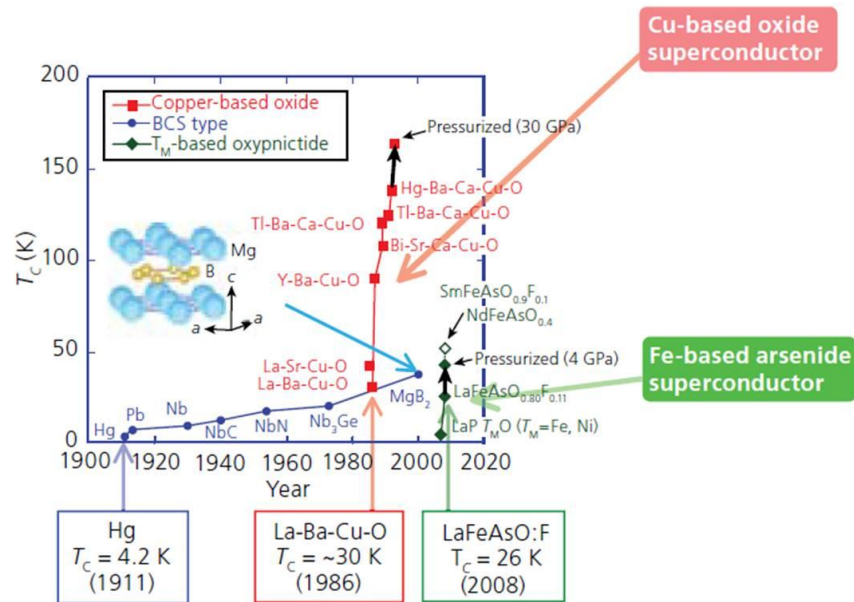


Figure 1.10. Plot showing the T_c of some known superconductors with their time of discovery. Adapted from [43].

Superconductors generally fall under two categories, type I and type II. These two groups are distinguished by the effect magnetic fields have on their transition from a normal (non-superconducting) state to their superconducting state below the T_c . As figure 1.11 shows, type I superconductors will possess a single critical field that similar to the critical temperature will be a boundary for the onset of superconductivity. Type I superconductors include most pure element superconductors. Contrastingly, with type II superconductors there is an upper and lower critical field in which a tertiary state referred to as a vortex state is present. This state is a mixture between the normal and superconducting state. Above the upper critical field, the material will become normal (non-superconducting). It should be noted that with type II superconductors, the phase transition from the superconducting to normal

state is second order. Type II superconductors include complex oxide ceramics as well as metal alloys.

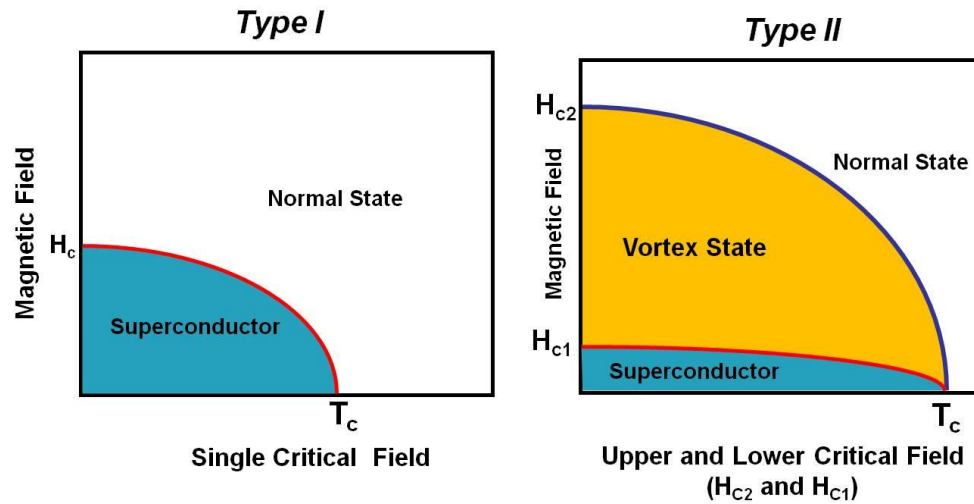


Figure 1.11. A depiction of the two types of superconductors with the difference being the upper and lower critical field for type II superconductors. Adapted from [44].

1.4 References

- [1] J.B. Goodenough, *Prog. Solid State Chem.* 5 (1971) 145–399.
- [2] C.N.R. Rao, B. Reveau, *Transition Metal Oxides: Structure, Properties, and Synthesis of Ceramic Oxides*, 2nd Edition., John Wiley & Sons, New York, 1998.
- [3] A.R. Armstrong, P.G. Bruce, *Nature* 381 (1996) 499–500.
- [4] M. Schofield, *Paint Manufacture* 15 (1945) 161.
- [5] A.R. West, T.B. Adams, F.D. Morrison, D.C. Sinclair, *J. Eur. Ceram. Soc.* 24 (2004) 1439–1448.
- [6] A.E. Smith, H. Mizoguchi, K. Delaney, N.A. Spaldin, A.W. Sleight, M.A. Subramanian, *J. Am. Chem. Soc.* 131 (2009) 17084–17086.
- [7] A.R. West, *Basic Solid State Chemistry Second Edition*, John Wiley & Sons, Ltd, Chichester, 1996.
- [8] W.D. Kingery, H.K. Bowen, D.R. Uhlmann, *Introduction to Ceramics*, 2nd Edition., John Wiley & Sons, New York, 1976.
- [9] T.M. Tritt, M.A. Subramanian, *Mater. Res. Soc. Bull.* 31 (2006) 188–198.
- [10] Obama Campaign, *All of the Above Approach - President Obama's Approach to Energy Independence* (2012).
- [11] T.M. Tritt, *Encyclopedia of Materials: Science and Technology* (2002) 1–11.
- [12] L. Basford, *Electricity Made Simple*, 1971.
- [13] G. Mahan, *Solid State Phys.* 51 (1998) 81–157.
- [14] S. Kasap, *Thermoelectric Effects in Metals: Thermocouples*. An e-booklet (1997-2001).
- [15] G.D. Mahan, J.O. Sofo, *Proc Natl Acad Sci U S A* 93 (1996) 7436–7439.
- [16] T. He, J. Chen, T.G. Calvarese, M.A. Subramanian, *Solid State Sci.* 8 (2006) 467–469.
- [17] M.A. Subramanian, *Thermoelectrics Lecture*, (2009).
- [18] D. Rowe, *CRC Handbook of Thermoelectrics*, 1995.
- [19] R. Franz, G. Wiedemann, R. Franz, G. Wiedemann, *Annalen der Physik* 165, 165 (1853) 497, 497–531, 531.
- [20] G.J. Snyder, E.S. Toberer, *Nat. Mater.* 7 (2008) 105–114.
- [21] T. He, J. Chen, H.D. Rosenfeld, M.A. Subramanian, *Chem. Mater.* 18 (2006) 759–762.
- [22] J. Eilertsen, S. Rouvimov, M.A. Subramanian, *Acta Mater.* 60 (2012) 2178–2185.
- [23] I. Terasaki, Y. Sasago, K. Uchinokura, *Thermoelectrics, 1998. Proceedings ICT 98. XVII International Conference On, 1998*, pp. 567–569.
- [24] I. Terasaki, N. Murayama, *Oxide Thermoelectrics, Research Signpost, Trivandrum, India, 2002*.
- [25] J. Androulakis, P. Migiakis, J. Giapintzakis, *Appl. Phys. Lett.* 84 (2004) 1099–1101.
- [26] R. Funahashi, T. Mihara, M. Mikami, S. Urata, N. Ando, *Thermoelectrics, 2005. ICT 2005. 24th International Conference, 2005*, pp. 307–314.
- [27] D.C. Mattis, *The Theory of Magnetism Made Simple.*, World Scientific Publishing Co., New York, 2006.

- [28] P.W. Selwood, *Magnetochemistry*, Interscience Publishers Inc., New York, 1943.
- [29] J.B. Goodenough, *Magnetism and the Chemical Bond*, John Wiley & Sons, New York, 1963.
- [30] M.M. Schieber, *Experimental Magnetochemistry: Nonmetallic Materials.*, John Wiley & Sons, New York, 1967.
- [31] A.E. Smith, *Functional Transition Metal Oxides: Structure-Property Relationships*, Oregon State University, 2010.
- [32] R. Schad, C.D. Potter, P. Beliën, G. Verbanck, V.V. Moshchalkov, Y. Bruynseraede, *Appl. Phys. Lett.* 64 (1994) 3500.
- [33] M.N. Baibich, J.M. Broto, A. Fert, F.N. Van Dau, F. Petroff, *Phys. Rev. Lett.* 61 (1988) 2472–2475.
- [34] R.C. Buchanan, *Ceramic Materials for Electronics: Processing, Properties, and Applications.*, Marcel Dekker, Inc., New York, 1986.
- [35] J. Bardeen, L.N. Cooper, J.R. Schrieffer, *Phys. Rev.* 108 (1957) 1175–1204.
- [36] W. Meissner, R. Ochsenfeld, *Naturwissenschaften* 21 (1933) 787–788.
- [37] Uses for Superconductors.
<http://www.superconductors.org/Uses.htm>. Accessed April 2012.
- [38] H.K. Onnes, *Commun. Phys. Lab. Unvi. Leiden. Suppl.* 29 (1911).
- [39] J.G. Bednorz, K.A. Müller, *Z. Phys. B: Condens. Matter* 64 (1986) 189–193.
- [40] M. Wu, J. Ashburn, C. Torng, P. Hor, R. Meng, L. Gao, Z. Huang, Y. Wang, C. Chu, *Phys. Rev. Lett.* 58 (1987) 908–910.
- [41] A. Schilling, M. Cantoni, J.D. Guo, H.R. Ott, Published Online: 06 May 1993; Doi:10.1038/363056a0 363 (1993) 56–58.
- [42] Y. Kamihara, T. Watanabe, M. Hirano, H. Hosono, *J. Am. Chem. Soc.* 130 (2008) 3296–3297.
- [43] H. Hosono, *Mater. Matters* 4 32–35 (2009).
- [44] M.A. Subramanian, *Superconductivity Lecture*, (2009).

CHAPTER 2

Substitutional studies on the hexagonal structure of $\text{Pb}_3\text{Rh}_7\text{O}_{15}$

2.1 Abstract

A brief introduction to Rhodium oxides along with an insight into mixed valency, a common feature of these oxides that tends to influence their physical properties is given. Also discussed is the concept of bond valency which can be used to determine the presence of mixed valency when good structural data is provided. Charge ordering, a phenomena observed in numerous mixed valent systems particularly in certain temperature regimes is introduced. To further understand the charge ordering phenomenon, the Verwey transition, which is a type of charge ordering transition, is also discussed.

With these concepts introduced, the second part of this chapter describes the substitution investigations into hexagonal $\text{Pb}_3\text{Rh}_7\text{O}_{15}$. A complete solid solution was found between isostructural $\text{Pb}_3\text{Mn}_7\text{O}_{15}$ and $\text{Pb}_3\text{Rh}_7\text{O}_{15}$. Single-crystals of two members of the solid solution $\text{Pb}_3\text{Rh}_{7-x}\text{Mn}_x\text{O}_{15}$ ($x = 1.07$ and 2.26) were grown and their crystal structures were determined. The Verwey-type transition for $\text{Pb}_3\text{Rh}_7\text{O}_{15}$ at 185 K remains with a 3% substitution of Mn for Rh but disappears with 4% substitution of Mn for Rh. The magnetic ordering temperature found for $\text{Pb}_3\text{Mn}_7\text{O}_{15}$ at about 70 K is maintained at a 43% substitution of Rh for Mn but has disappeared for 57% substitution of Rh for Mn. The unit cell volume of this layered structure contracts with increasing x for $\text{Pb}_3\text{Rh}_{7-x}\text{Mn}_x\text{O}_{15}$ phases, but the structure

actually expands in the direction perpendicular to the layers due increased separation between the layers.

Publications based on this chapter:

1. Gatimu, A.J., Mizoguchi, H., Sleight, A.W., Subramanian, M.A. Verwey-type transition within the $\text{Pb}_3\text{Rh}_{7-x}\text{Mn}_x\text{O}_{15}$ solid solution. *Journal of Solid State Chemistry* 183, 866–870. (2010)

2.2 Introduction

2.2.1 Rhodium Oxides

The chemistry of oxides of rhodium is of importance because of the range of possible practical applications of rhodium and its oxides [1]. The stable oxide of Rh under normal conditions is Rhodium Sesquioxide, Rh_2O_3 . This most commonly adopts a rhombohedral structure of the $\alpha - \text{Al}_2\text{O}_3$ structure-type and R-3c spacegroup. This ambient conditions form of Rh_2O_3 is referred to as Rh_2O_3 -I [2,3].

Two other non-ambient conditions polymorphs of this corundum structure of Rh_2O_3 are known. Rh_2O_3 -II is a high pressure phase with an orthorhombic unit cell and Pbn space group symmetry while Rh_2O_3 -III is a high temperature phase also with an orthorhombic unit cell and Pbc space group symmetry [4,5]. Rh_2O_3 -II has been found to be a semiconductor with an activation energy of ~ 0.16 eV [4], while Rh_2O_3 -III has also been found to be semiconducting but with a significantly lower activation energy of ~ 0.05 eV [6]. More recently, investigations by Roy et al. have shown that Rh_2O_3 -I is a p-type semiconductor like Rh_2O_3 -III with suggestions that the overlap of 4d orbitals of Rh^{3+} in Rh_2O_3 may lead to a formation of a narrow d-band and presence of Rh^{4+} ions as acceptor levels above the valence band, explaining the p-type nature of the oxide [6,7]. In more complex oxides of Rh such as ternary oxides, mixed valency of Rh^{3+} and Rh^{4+}

is very common. Examples include $\text{Ba}_9\text{Rh}_8\text{O}_{24}$, $\text{Ba}_{11}\text{Rh}_{10}\text{O}_{30}$, $\text{Sr}_6\text{Rh}_5\text{O}_{15}$ and $(\text{Bi}_6\text{O}_5)\text{Rh}_{12}\text{O}_{24}$ [8–11].

In most rhodates containing only Rh^{3+} such as RhCrO_3 and Rh_2MoO_6 , semiconducting behavior is usually expected as the full 4d t_{2g} band acts as a valence band and the empty 4d e_g band as the conduction band. The band gap is usually ~ 2 eV [1,11]. However this is not always the case as found in $\text{SrMg}_2\text{Rh}_6\text{O}_{12}$, which may be initially expected to possess only Rh^{3+} but shows p-type conductivity alluding to some presence of Rh^{4+} [11].

On the other hand, in most rhodates containing only Rh^{4+} or a high concentration of Rh^{4+} , metallic behavior is usually observed. Examples include $\text{Sc}_2\text{Rh}_2\text{O}_7$, $\text{Tl}_2\text{Rh}_2\text{O}_7$ and BaRhO_3 . The conductivity is p-type as a hole is present in the 4d t_{2g} band that is 5/6 full [1]. It should be noted that these Rh^{4+} oxides tend to require synthesis under high pressure and often in O_2 flow to stabilize the Rh^{4+} oxidation state and prevent reduction of Rh^{4+} to Rh^{3+} that tends to occur in air leading to mixed valency.

2.2.2 Mixed Valency

This refers to the presence of one or more elements in a compound occupying more than one oxidation state. It is very commonly found in TMOs. In fact, mixed valence compounds can be

grouped into useful classes prescribed by Robin and Day [12]. These classes are defined by the environment of the ions and their interactions.

In class I, different oxidation states of a particular element are found in very different crystallographic environments. This means that no interactions occur between them, which is key to the tendency of class I compounds to lack color as electrons cannot easily be transferred between the ions.

In class II compounds, the different oxidation states are still in different crystallographic sites, however the differences between the sites is not as significant as in class I compounds. This means lower energy requirements to transfer electrons between sites allowing the compounds to have color and leading to semiconducting behavior.

Lastly, in class III compounds, the different oxidation states of the element are in similar crystallographic sites and electrons are delocalized between the two oxidation states. If this occurs in a cluster, the compound can be classified as class IIIA but if instead the delocalization occurs throughout the compound the compound can be classified as class IIIB compound and will show metallic conduction.

2.2.3 Bond Valence

This is a concept stemming from Linus Pauling's proposal (second rule) that each bond can be assigned a valence which can be a

non-integer value and the sum of the bond valences around a specific atom will equal its oxidation state thus,

$$V_i = \sum S_{ij}$$

where v_i is the oxidation state of atom i and S_{ij} is the valence of the bond between atoms i and j [13].

This concept has been developed by inorganic chemists as a valid tool in determining valencies of elements in novel structures and coordinations. This is possible by developing a relationship between bond length (R) and bond valence (S) and by empirically determining bond valence parameters (R_o) and (B) that depend on the two atoms forming the bond [14]. The relationship is,

$$S = \exp((R_o - R)/B)$$

In some cases bond valence parameters for some ions are not well defined, such as for Rh^{4+} . Nonetheless, bond valences and bond valence sums are still a useful tool particularly if good X-ray or crystal data with a high level of accuracy in bond lengths is available.

2.2.4 Charge Ordering

Charge-ordering (CO) is a phenomena that was first proposed by E.P. Wigner in the late in the late 1930s [15]. This involves ionic charges being localized on distinct crystallographic sites below a

particular temperature. The charges can be ordered in a number of ways, both in 2-D and 3-D.

CO transitions tend to greatly influence the physical and structural properties. This is best seen in Magnetite (Fe_3O_4) that undergoes a CO transition at ~ 120 K named a Verwey transition (described in more detail in the next section), $\text{La}_{0.5}\text{Ca}_{0.5}\text{MnO}_3$ involving Mn^{3+} and Mn^{4+} ordering and also in Rhodium oxides like $(\text{Bi}_6\text{O}_5)\text{Rh}_8^{3+}\text{Rh}_4^{4+}\text{O}_{24}$ that involves Rh^{3+} and Rh^{4+} ordering at least partially [16–18].

It should be noted that bond valence calculations can be very useful in identifying CO phenomena particularly if crystal data is available [18]. Also of note is the difference between CO and orbital ordering. Orbital ordering involves ordering of individual d orbitals (d_z^2 in the case of $\text{La}_{0.5}\text{Ca}_{0.5}\text{MnO}_3$) [17,19]. CO is usually accompanied by orbital ordering.

2.2.5 The Verwey Transition

This can be described as a CO transition occurring in a mixed-valent system involving an ordering of formal valence states in the low temperature phase below the transition temperature (T_v) [20]. To be best understood, an analysis of the Verwey transition in Fe_3O_4 is essential.

Fe_3O_4 , nature's most common mixed valence mineral, is the prototype system for this type of transition as it was first identified in Fe_3O_4 , by E.J.W Verwey in 1939 [16]. Verwey proposed that in Fe_3O_4 a CO transition at temperatures ≤ 120 K occurs involving a localization of electrons. Nonetheless, it should be noted that earlier work on Fe_3O_4 revealing changes in magnetism in Fe_3O_4 at low temperatures had already been done by other investigators such as Renger in 1913 and Weiss and Forrer in 1914 showing spontaneous changes in magnetization near 120 K [21–23].

Fe_3O_4 has an inverse spinel structure. Above T_v , Fe_3O_4 which can be expressed as $\text{Fe}^{3+}[\text{Fe}^{2+},\text{Fe}^{3+}]\text{O}_4$ has Fe^{3+} in the tetrahedral voids and both Fe^{2+} and Fe^{3+} in a disordered arrangement in the octahedral voids of the structure. This disorder on the octahedral sites means a delocalization of electrons and this is observed in the electrical properties of Fe_3O_4 above T_v , where the compound is found to be metallic (having an electrical resistivity of ~ 4 m Ω cm, characteristic of a poor metal) [24].

At 119 K, the Fe^{2+} and Fe^{3+} ions on the octahedral sites become ordered and a localization of electrons occurs. This is observed crystallographically with a lowering of symmetry but is most prominently observed in the electrical properties where the compound becomes semiconducting and a sharp increase in resistivity is observed

as can be seen in figure 2.1, showing the different physical property manifestations of the the Verwey transition in Fe_3O_4 [25].

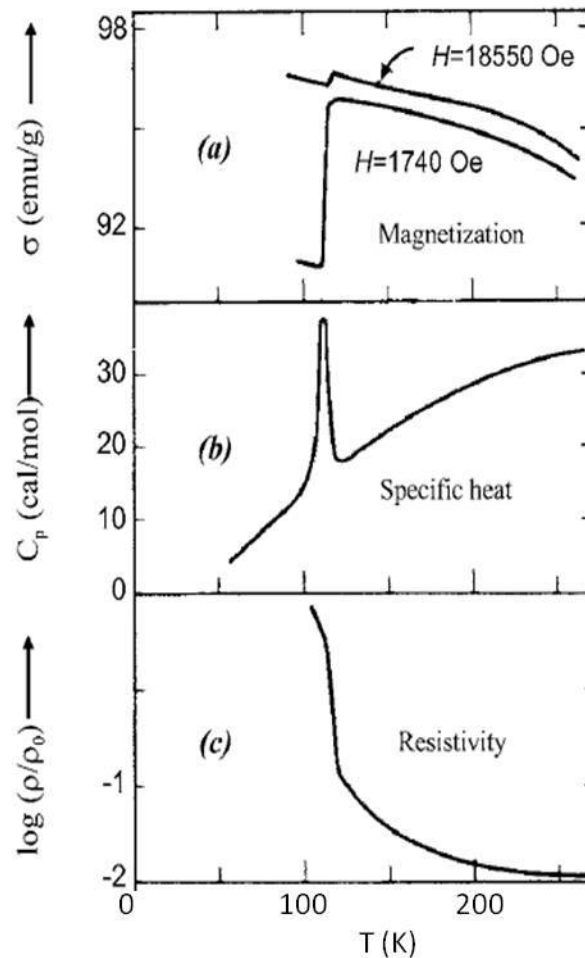


Figure 2.1. The Verwey Transition at 119 K in Magnetite is visible in a number of physical properties of the material include (a) the magnetization, (b) the specific heat and (c) the resistivity. Adapted from [25].

It should be noted that Verwey initially suggested that below T_v the crystal structure becomes tetragonal. However, this has been since disproved. Some investigators argued that an orthorhombic unit

cell was the best solution as it would lead to the minimal electrostatic repulsion (satisfying the Anderson criterion) [26]. More recent investigations have hinted at the likeliness of a monoclinic structure [27,28]. Nonetheless, no conclusive structural data has been given to fully explain the low temperature crystal structure of Fe_3O_4 and also CO mechanism below 120 K. This has led to a continued strong interest in the system.

2.3 Verwey-Type Transition within the $\text{Pb}_3\text{Rh}_{7-x}\text{Mn}_x\text{O}_{15}$ Solid Solution

2.3.1 Introduction

The same basic structure is found for both $\text{Pb}_3\text{Mn}_7\text{O}_{15}$ and $\text{Pb}_3\text{Rh}_7\text{O}_{15}$ (Figure 2.2), and apparently no other compounds have been synthesized with this structure [29–35]. Structural studies establish that all Pb is 2+ in both compounds; thus, there is mixed valency of Rh and Mn with an average oxidation state of 3.4+. There are four or more crystallographic sites for the Rh or Mn atoms. Bond valence calculations indicate some charge ordering of M^{3+} and M^{4+} cations for both $\text{Pb}_3\text{Mn}_7\text{O}_{15}$ and $\text{Pb}_3\text{Rh}_7\text{O}_{15}$, but a complete description of this charge ordering has been elusive for both compounds. The high electrical conductivity and magnetic properties of $\text{Pb}_3\text{Rh}_7\text{O}_{15}$ indicate some delocalization of the 4d electrons of Rh whereas the magnetic properties of $\text{Pb}_3\text{Mn}_7\text{O}_{15}$ indicate a lack of such delocalization for the 3d electrons of Mn [35,36]. The dielectric properties of $\text{Pb}_3\text{Mn}_7\text{O}_{15}$ have suggested possible interesting multiferroic properties for this compound [37].

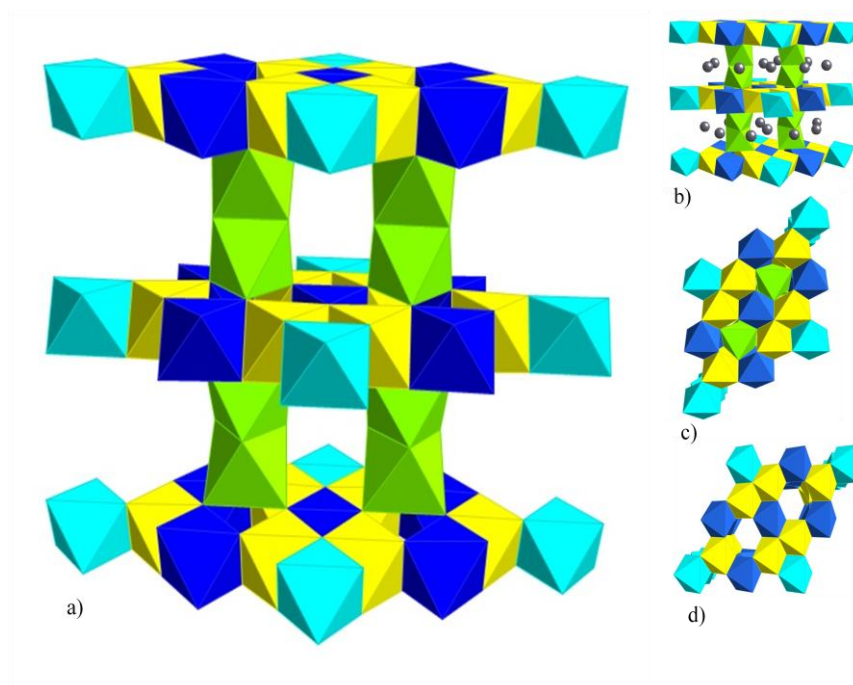


Figure 2.2. Structure of $\text{Pb}_3\text{Rh}_7\text{O}_{15}$ and $\text{Pb}_3\text{Mn}_7\text{O}_{15}$. Colors of octahedra indicate Rh valencies in $\text{Pb}_3\text{Rh}_7\text{O}_{15}$. Green represents Rh^{3+} in the 8h site, yellow represents $\text{Rh}^{3.5+}$ in the 12i site, cyan represents Rh^{3+} in the 2b site, and dark blue represents Rh^{4+} in the 6f site. B). The hexagonal structure with the Pb atoms shown in two sites within the interlayer region. C). A view along the c-axis of the structure with the interlayer Rh present and d). without the interlayer Rh present.

The ideal structures for both $\text{Pb}_3\text{Mn}_7\text{O}_{15}$ and $\text{Pb}_3\text{Rh}_7\text{O}_{15}$ are hexagonal. However, the first structure determination for $\text{Pb}_3\text{Mn}_7\text{O}_{15}$ by Darriet et al. concluded that the actual symmetry at room temperature is orthorhombic [29]. The orthorhombic description was later supported by Marsh et al. [30]. Le Page et al. subsequently argued that this structure is really hexagonal [31]. A very recent high resolution study by Rasch et al. using synchrotron data resolved this controversy in favor of orthorhombic symmetry [32]. The lattice of $\text{Pb}_3\text{Mn}_7\text{O}_{15}$ is metrically far from hexagonal at 15 K. With increasing temperature the lattice metrically approaches hexagonal, but is still not quite metrically hexagonal by 295 K [32].

The structure of $\text{Pb}_3\text{Rh}_7\text{O}_{15}$ at room temperature is clearly hexagonal with a space group of $\text{P6}_3/\text{mcm}$ [33–35]. However, there is a phase transition at 185 K. The space group changes below this phase transition, but extensive efforts have failed to reveal the correct space group below 185 K [35]. High resolution diffraction studies using synchrotron data show no detectable metric deviation from a hexagonal lattice down to 80 K [35]. Electrical conductivity and other measurements indicate that the transition for $\text{Pb}_3\text{Rh}_7\text{O}_{15}$ at 185 K is a Verwey-type transition with a change in charge ordering associated with Rh [35]. The primary motivation of this study was to examine the impact on this transition as Mn is substituted for Rh.

2.3.2 Results

All $\text{Pb}_3\text{Rh}_{7-x}\text{Mn}_x\text{O}_{15}$ compositions attempted yielded single phase products suggesting a complete solid solution between $\text{Pb}_3\text{Mn}_7\text{O}_{15}$ and $\text{Pb}_3\text{Rh}_7\text{O}_{15}$. Figure 2.3 shows the variation in the unit cell edges, c/a ratio, and unit cell volume for the $\text{Pb}_3\text{Rh}_{7-x}\text{Mn}_x\text{O}_{15}$ phases based on refinement of powder XRD data. Crystallographic results for $\text{Pb}_3\text{Rh}_{5.93}\text{Mn}_{1.07}\text{O}_{15}$ and $\text{Pb}_3\text{Rh}_{4.74}\text{Mn}_{2.26}\text{O}_{15}$ single crystals are summarized in Table 2.1. The refined atomic coordinates are given in Table 2.2, and the refined Rh/Mn occupations are in Table 2.3. The compositions of $\text{Pb}_3\text{Rh}_{5.93}\text{Mn}_{1.07}\text{O}_{15}$ and $\text{Pb}_3\text{Rh}_{4.74}\text{Mn}_{2.26}\text{O}_{15}$ are based on these occupation refinements. The c/a value of 1.32 for the $\text{Pb}_3\text{Rh}_{4.74}\text{Mn}_{2.26}\text{O}_{15}$ crystal fits well on the c/a plot (Figure 2.3)

providing independent verification of the composition. Some interatomic distances are given in Table 2.4 and plotted vs. composition in Figure 2.4.

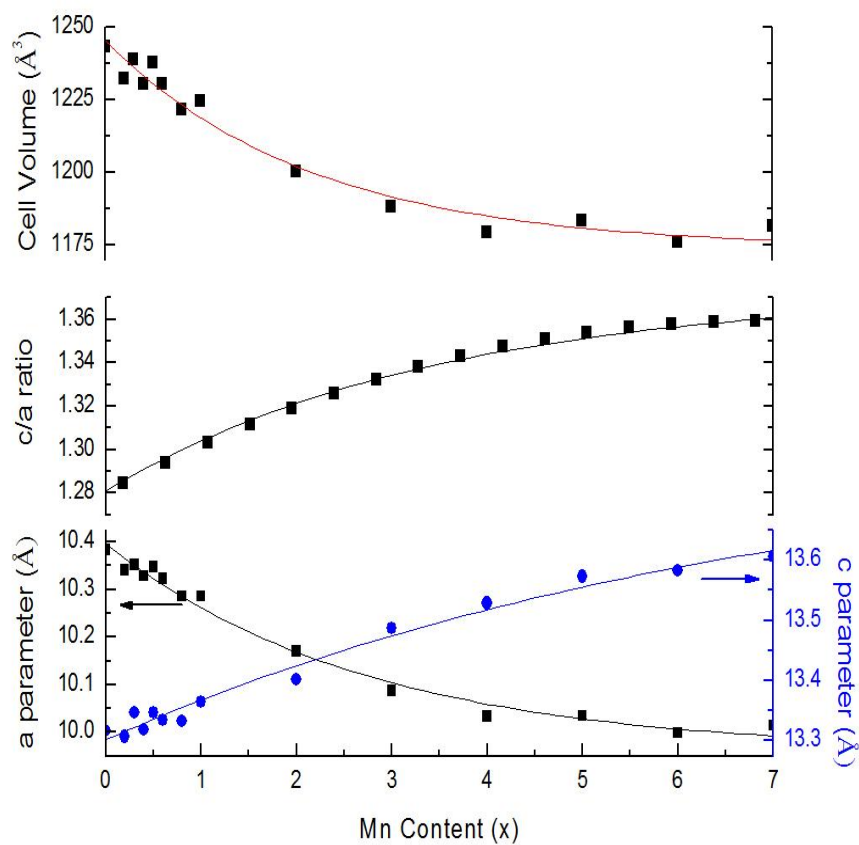


Figure 2.3. Cell edges, c/a , and unit cell volume for $\text{Pb}_3\text{Rh}_{7-x}\text{Mn}_x\text{O}_{15}$ phases.

Table 2.1. Summary of Crystallographic Results

Empirical formula	$\text{Pb}_3\text{Rh}_{5.93}\text{Mn}_{1.07}\text{O}_{15}$	$\text{Pb}_3\text{Rh}_{4.74}\text{Mn}_{2.26}\text{O}_{15}$
Formula weight	1530.85	1473.65
Temperature	173(2) K	233(2) K
Wavelength	0.71073 Å	0.71073 Å
Crystal system	Hexagonal	Hexagonal
Space group	$\text{P6}_3/\text{mcm}$	$\text{P6}_3/\text{mcm}$
Unit cell dimensions	a = 10.260(1) Å c = 13.342(3) Å	a = 10.150(2) Å c = 13.387(5) Å
Volume	1216.3(4) Å ³	1194.3(5) Å ³
Z	4	4
Density (calculated)	8.360 g/cc	8.196 g/cc
Absorption coefficient	50.345/mm	50.883/mm
F(000)	2639	2543
Crystal size	0.05 x 0.03 x 0.01 mm	0.05 x 0.04 x 0.02 mm
Theta range for data collection	2.29 to 26.99°	2.32 to 27.00°
Index ranges	-13 ≤ h ≤ 13, -13 ≤ k ≤ 13, -17 ≤ l ≤ 16	-12 ≤ h ≤ 12, -12 ≤ k ≤ 12, -17 ≤ l ≤ 17
Reflections collected	12491	12309
Independent reflections	515 [R(int) = 0.0585]	504 [R(int) = 0.0523]
Completeness to theta = 28.24°	100.00%	100.00%
Absorption correction	Semi-empirical from equivalents	SADABS
Max. and min. transmission	0.6329 and 0.1874	0.4293 and 0.1852
Refinement method	Full-matrix least-squares on F ²	Full-matrix least-squares on F ²
Data / restraints / parameters	515 / 4 / 59	504 / 4 / 59
Goodness-of-fit on F ²	1.182	1.165
Final R indices [I > 2σ(I)]	R1 = 0.0172, wR2 = 0.0395	R1 = 0.0162, wR2 = 0.0346
R indices (all data)	R1 = 0.0186, wR2 = 0.0404	R1 = 0.0176, wR2 = 0.0356
Extinction coefficient	0.00008(2)	0.00107(4)
Largest diff. peak and hole	1.317 and -1.654 e.Å ⁻³	1.061 and -1.176 e.Å ⁻³

Table 2.2. Atomic coordinates and isotropic displacement factors ($\text{\AA}^2 \times 10^3$)

	$\text{Pb}_3\text{Rh}_{5.93}\text{Mn}_{1.07}\text{O}_{15}$				$\text{Pb}_3\text{Rh}_{4.74}\text{Mn}_{2.26}\text{O}_{15}$			
	x	y	z	U(eq)*	x	y	z	U(eq)*
Pb1	0	0.3926(1)	1/4	8(1)	0	0.3894(1)	1/4	10(1)
Pb2	0.7374(1)	0	1/4	6(1)	0.7388(1)	0	1/4	8(1)
M1	2/3	1/3	0.1487(1)	3(1)	2/3	1/3	0.1490(1)	4(1)
M2	0.6639(1)	0.1681(1)	0	4(1)	0.6645(1)	0.1677(1)	0	4(1)
M3	0	0	0	4(1)	0	0	0	6(1)
M4	1/2	0	0	3(1)	1/2	0	0	5(1)
O1	0.6666(5)	0	0.0780(5)	7(1)	0.6673(5)	0	0.0764(4)	9(1)
O2	0.8321(5)	0.1679(5)	0.0772(4)	7(1)	0.8332(5)	0.1668(5)	0.0763(4)	9(1)
O3	0.8418(4)	0.3337(4)	0.0808(3)	8(1)	0.8423(4)	0.3329(4)	0.0815(3)	8(1)
O4	0.5205(6)	0.3430(6)	1/4	5(1)	0.6557(6)	0.1749(6)	1/4	7(1)

*U_(eq) is defined as one third of the trace of the orthogonalized U^{ij} tensor.

Table 2.3. Site percentage (%) occupied by Rh for the four octahedral sites

	position	$\text{Pb}_3\text{Rh}_{5.93(2)}\text{Mn}_{1.07(2)}\text{O}_{15}$	$\text{Pb}_3\text{Rh}_{4.74(2)}\text{Mn}_{2.26(2)}\text{O}_{15}$
M	all	84.7	67.7
M1	8h	96.6	89.3
M2	12i	79.0	55.5
M3	2b	77.2	49.9
M4	6f	82.3	66.0

Table 2.4. Interatomic distances in Å.

	Pb ₃ Rh ₇ O ₁₅	Pb ₃ Rh _{5.93} Mn _{1.07} O ₁₅	Pb ₃ Rh _{4.74} Mn _{2.26} O ₁₅
Pb1-O3 x 4	2.654(4)	2.667(4)	2.657(4)
Pb1-O4 x 2	2.403(6)	2.395(6)	2.379(6)
Pb1-O4 x 2	3.105(5)	3.080(5)	3.057(5)
Pb2-O1 x 2	2.384(5)	2.407(7)	2.435(5)
Pb2-O4 x 2	2.353(6)	2.345(6)	2.315(6)
M1-O3 x3	2.012(5)	2.011(4)	2.001(4)
M1-O4 x 3	2.068(5)	2.057(5)	2.061(5)
M2-O3 x 2	1.994(5)	1.972(4)	1.960(4)
M2-O2 x 2	2.017(5)	2.009(5)	1.990(5)
M2-O1 x 2	2.022(4)	2.002(4)	1.974(3)
M3-O2 x 6	2.027(5)	2.007(5)	1.977(5)
M4-O3 x 4	1.9989(5)	1.985(4)	1.978(4)
M4-O1 x 2	2.017(6)	2.001(6)	1.982(5)
M1-M1*	2.692(1)	2.702(1)	2.704(1)

*This M-M distance across the face shared octahedra has increased to 2.785(8) Å in Pb₃Mn₇O₁₅ [32].

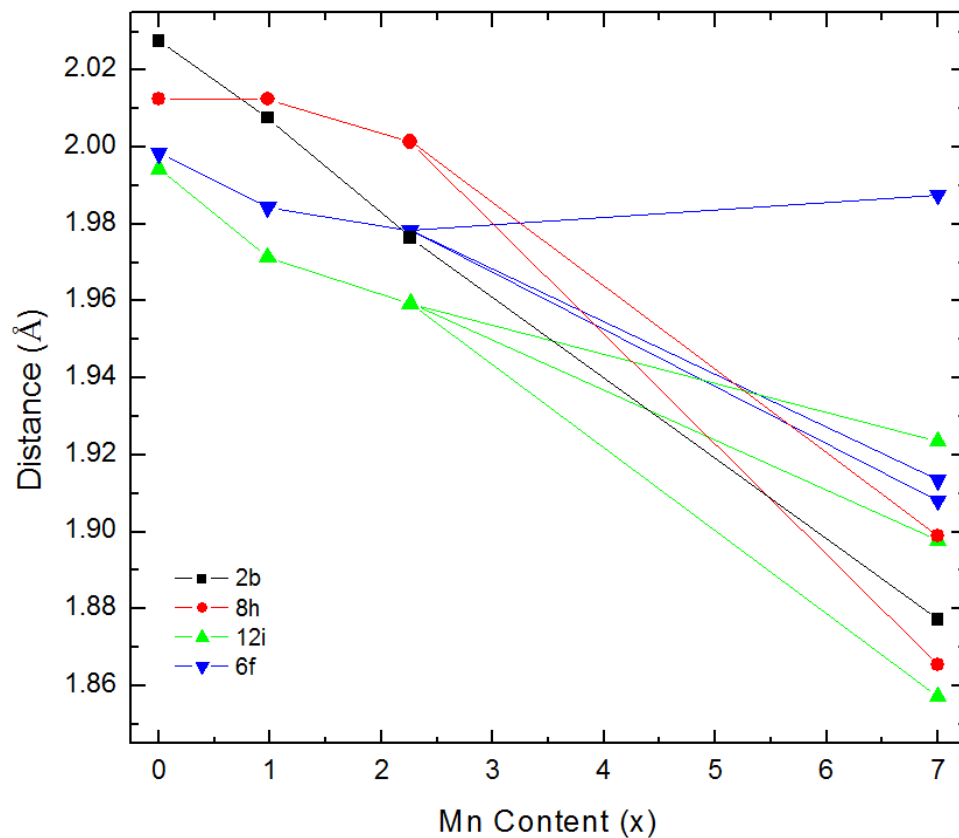


Figure 2.4. Some interatomic distances (Rh/Mn-O) vs. x for $\text{Pb}_3\text{Rh}_{7-x}\text{Mn}_x\text{O}_{15}$ phases. $X < 7$ phases are shown in hexagonal symmetry while the $x = 7$ phase is shown in orthorhombic symmetry.

Results of our four-probe electrical resistivity measurements on sintered polycrystalline bars are shown vs. temperature in figure 2.5. Resistivity values are normalized to 1.0 at room temperature to eliminate variations due to variable porosity and grain boundary contributions. The room temperature resistivities of $\text{Pb}_3\text{Mn}_7\text{O}_{15}$ and $\text{Pb}_3\text{Rh}_7\text{O}_{15}$ are 360 and 0.001 ohm-cm, respectively. Results of our magnetic susceptibility measurements for Mn-rich compositions using Curie Weiss fitting are presented in Table 2.5 and figure 2.6.

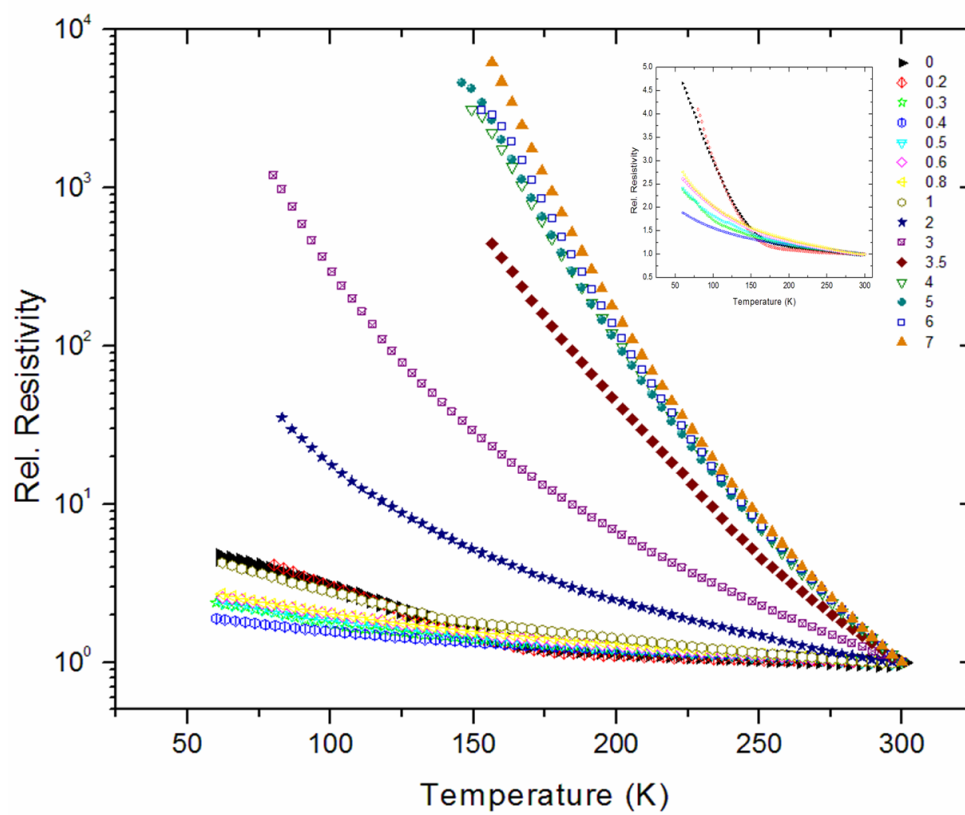


Figure 2.5. Resistivity vs. temperature for $\text{Pb}_3\text{Rh}_{7-x}\text{Mn}_x\text{O}_{15}$ phases. Inset shows linear data for the $x < 1$ phases.

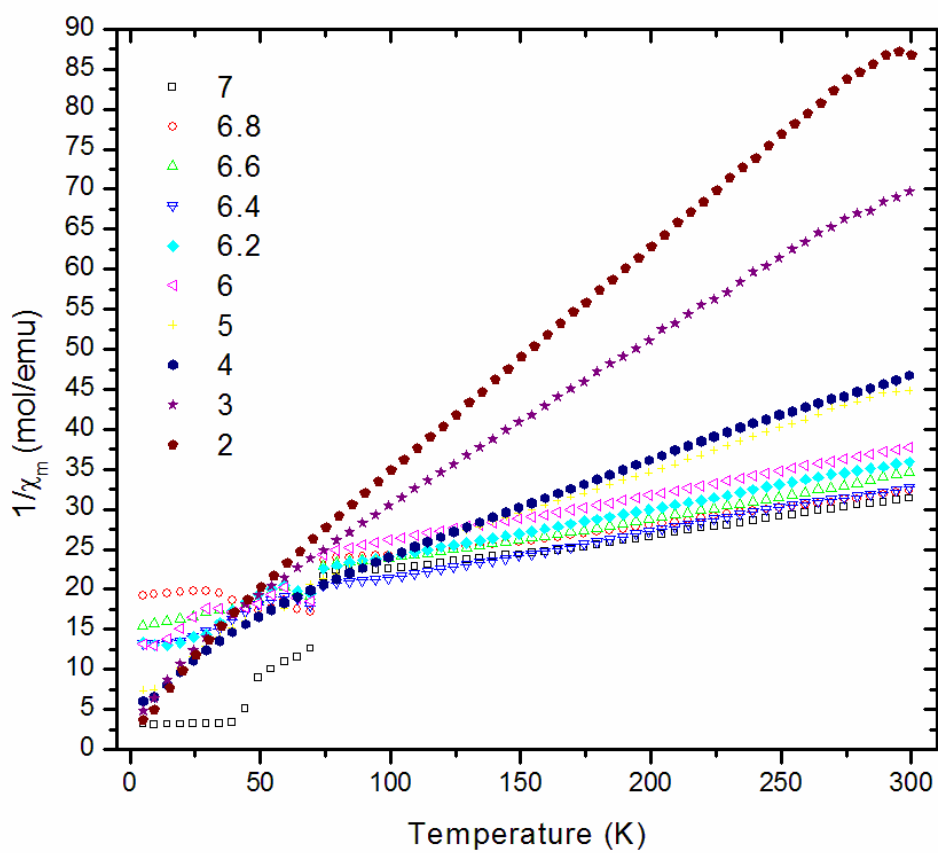


Figure 2.6. Magnetic susceptibility for $\text{Pb}_3\text{Rh}_{7-x}\text{Mn}_x\text{O}_{15}$ phases. χ_m is calculated in emu/mol.

Table 2.5. Summary of magnetic susceptibility measurements for $\text{Pb}_3\text{Rh}_{7-x}\text{Mn}_x\text{O}_{15}$ phases.

Pb ₃ Rh _{7-x} Mn _x O ₁₅ Effective Paramagnetic Moment Data											
x	1	2	3	4	5	6	6.2	6.4	6.6	6.8	7
θ_w (K)	-7.5	-25.1	-58.6	-128.1	-126.8	-346.8	-303.6	-259.9	-338.9	-509.7	-390.2
C	1.61	3.59	5.06	9.08	9.37	17.15	16.75	16.86	18.62	25.19	22.03
μ_{obs} (m _B)	3.6	5.38	6.39	8.56	8.69	11.76	11.62	11.66	12.26	14.25	13.33

2.3.3 Discussion

Given that Mn^{3+} and Mn^{4+} are smaller than Rh^{3+} and Rh^{4+} , respectively, we can expect that the average M-O distances for the MO_6 octahedra will decrease with increasing Mn content for the $\text{Pb}_3\text{Rh}_{7-x}\text{Mn}_x\text{O}_{15}$ phases. This is, in fact, the trend observed for all four of the crystallographically distinct M octahedra as shown in figure 2.4. Thus, we also have a decrease in unit cell volume with increasing Mn content (Figure 2.3). Given that all of these M-O bond distances have nearly equal contributions perpendicular and parallel to the c axis, we might expect that both a and c would decrease with increasing Mn content. In fact, a and b decrease with increasing Mn, but c increases. The M-M distances across the edge shared octahedra are all decreasing with decreasing Mn content because they have a component only perpendicular to the c axis. The M-M distances across the face shared octahedra, however, show an increase as the Mn concentration increases (Table 2.4), and this distance is aligned along the c axis. This then could be a partial explanation for the increase in c as the Mn

content increases. However, this increase in this M-M distance is only significant for the pure Mn phase, and the increase in c actually occurs over the entire solid solution (Figure 2.3). The answer to this increase in c lies with the Pb-O bonding (Figure 2.7). As the M-O sheets contract in the ab plane with increasing Mn content, the Pb-O4 distances in this plane all decrease (Table 2.4 and Figure 2.7). To compensate for this additional bonding power, the Pb-O distances that are essentially perpendicular to the ab plane (Pb1-O3 and Pb2-O1) increase (Table 2.4 and Figure 2.7) resulting an increase of c . There is another reason why the Pb-O bonding causes an increase in c . As the O atoms in the sheets become closer to one another with increasing Mn content, the O3-Pb1-O3 bonds angles to the sheets are forced to decrease. The decrease of this angle from 66.2° to 63.0° on going from $\text{Pb}_3\text{Rh}_7\text{O}_{15}$ to $\text{Pb}_3\text{Rh}_{4.74}\text{Mn}_{2.26}\text{O}_{15}$ without any change in Pb-O distances would force an increase of 0.14 \AA in c . Thus, the M-O sheets would be forced further apart even with no change in Pb-O distances. The M-O sheets themselves contract with increasing Mn content mainly perpendicular to c with little variation along c due to a constraint caused by the edge sharing of the octahedra [38].

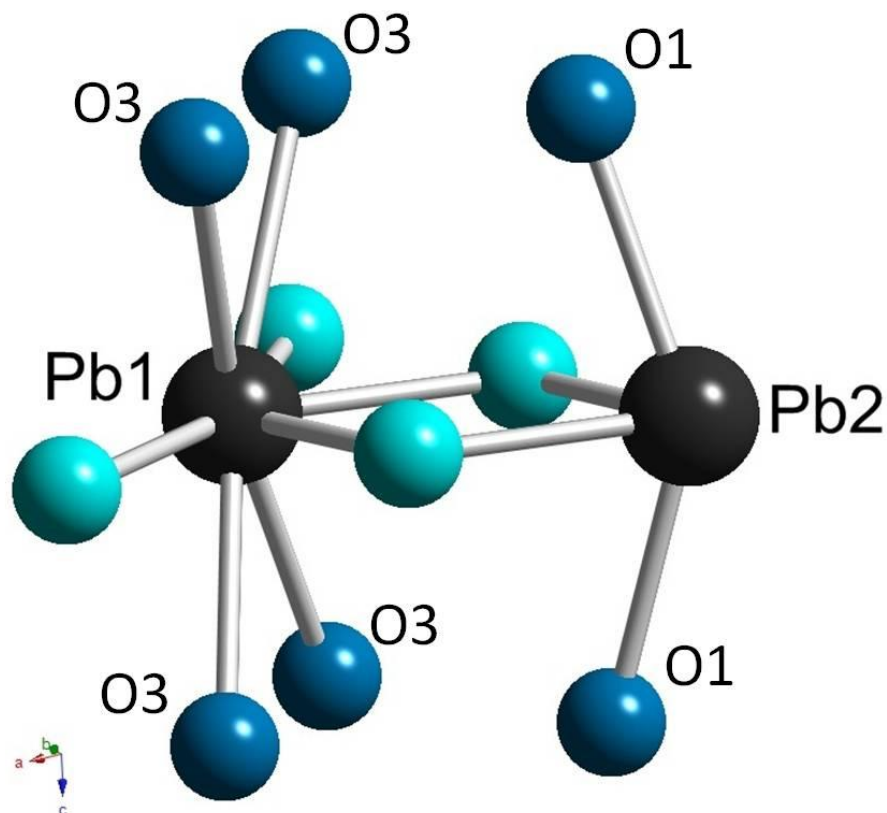


Figure 2.7. Pb-O bonding in $\text{Pb}_3\text{Rh}_{7-x}\text{Mn}_x\text{O}_{15}$ phases. Cyan spheres represent O4 atoms. Contraction of a with increasing x causes Pb-O distances in the ab plane to decrease, which is compensated by an increase in Pb-O bond lengths perpendicular to this plane resulting in an expansion of c . The decrease of the O3-Pb1-O3 angle with increasing x also contributes to an increase in c .

Refinements of the Rh/Mn ratio at each of the four crystallographic sites show that Rh has a very strong preference for the 8h site (Table 2.3). This is the site where two octahedra share a face, and thus the site of maximum M-M repulsion. Bond valence calculations for $\text{Pb}_3\text{Rh}_7\text{O}_{15}$ show that this site is Rh^{3+} [35], as would be expected because the presence of Rh^{4+} would increase the electrostatic repulsion. Similarly, bond valence calculations for $\text{Pb}_3\text{Mn}_7\text{O}_{15}$ indicate an oxidation state close to 3+ for Mn at

this site [32]. However, this M-M electrostatic repulsion depends on real charges, which are very different than oxidation states. Given the electronegativity values of 2.28 and 1.56 for Rh and Mn [39], respectively, the real positive charge for Rh^{3+} will be much less than that of Mn^{3+} . Thus, the electrostatic repulsion will be much less for $\text{Rh}^{3+} - \text{Rh}^{3+}$ than for $\text{Mn}^{3+} - \text{Mn}^{3+}$, and this is reflected in the relevant distances of 2.69 Å for $\text{Rh}^{3+} - \text{Rh}^{3+}$ and 2.78 Å for $\text{Mn}^{3+} - \text{Mn}^{3+}$. This much greater $\text{Mn}^{3+} - \text{Mn}^{3+}$ distance relative to the $\text{Rh}^{3+} - \text{Rh}^{3+}$ distance occurs despite the fact that Mn-O distances are considerably shorter than the Rh-O distances. This higher repulsion for $\text{Mn}^{3+} - \text{Mn}^{3+}$ relative to $\text{Rh}^{3+} - \text{Rh}^{3+}$ is then the explanation for the tendency of Mn to avoid this site in the solid solution (Table 2.3).

Our electrical resistivity measurements (Figure 2.5) show that very little Mn substitution destroys the Verwey-type transition of $\text{Pb}_3\text{Rh}_7\text{O}_{15}$. The transition is evident for 3% substitution but has disappeared for 4% substitution. This demonstrates the very fragile nature of the charge ordering in $\text{Pb}_3\text{Rh}_7\text{O}_{15}$. The Verwey-type transition in Fe_3O_4 is also very sensitive to substitution for Fe. Substitutions for Fe of 2% Ni, Co, Al, Cr, or Ti result in a significant drop in the transition temperature [40]. Even a substitution of only 0.3% Ga gives a detectable change.

The magnetic properties of $\text{Pb}_3\text{Mn}_7\text{O}_{15}$ using a single crystal have been reported and analyzed in detail [36]. Paramagnetism is observed above 250 K, and there are several magnetic transitions below 250 K. The first at about 250 K was interpreted as short-range antiferromagnetic ordering within the

layers only. Then at 70 K long-range, three-dimensional order occurs. Although this is basically antiferromagnetic ordering, weak ferromagnetism results due to an incomplete cancellation of spins. Finally, at 20 K there is another transition that has been interpreted as a reorientation of the spins. Our magnetic susceptibility data for polycrystalline $\text{Pb}_3\text{Mn}_7\text{O}_{15}$ (Figure 2.6) are in general agreement with that reported. We see no clear evidence for a transition at about 250 K, but that transition was reported to give only a small change in slope of the $1/\chi$ curve vs. temperature curve. We see the sharp drop in $1/\chi$ at about 70 K indicative of long range magnetic order for all the samples up to and including $\text{Pb}_3\text{Rh}_3\text{Mn}_4\text{O}_{15}$ but not for samples richer in Rh.

2.3.4 Conclusion

The Verwey-type transition in $\text{Pb}_3\text{Rh}_7\text{O}_{15}$ is found to be very sensitive to substitution, similar to first the reported Verwey transition in Fe_3O_4 . The formation of a complete $\text{Pb}_3\text{Rh}_{7-x}\text{Mn}_x\text{O}_{15}$ solid solution is found to be possible. With Mn substitution the unit cell volume and ab plane contracts, however the structure actually expands along the c direction. Site preference for Rh cations is also observed with Mn substitution and this results from the electrostatic repulsions involved between the cations.

2.3.5 Experimental

Reactants were PbO (99.9% Aldrich), Rh₂O₃ prepared from RhI₃ by heating in air at 1073 K for 10 hrs, and Mn₂O₃ (98% Johnson Matthey). Stoichiometric amounts of the oxides were ground under ethanol in an agate mortar and pestle. Pelletized samples were placed in an alumina boat and heated to 1073 K for Rh rich samples and 1148 K for Mn rich samples. X-ray powder diffraction data were collected with a RIGAKU MINIFLEX II using Cu K α radiation and a graphite monochromator.

Single crystals of composition Pb₃Rh_{5.93}Mn_{1.07}O₁₅ and Pb₃Rh_{4.74}Mn_{2.26}O₁₅ were grown in a PbO flux in an intimate mixture of PbO, Rh₂O₃ and Mn₂O₃ in a 1:10 and 1:5 sample:PbO excess ratio, respectively. Crystal growth was in a Pt crucible heated to 1373 K in air for 10 hrs then cooled to 1223 K at 3 K/hr. After holding at 1223 K for 0.5 hr, the crucible was cooled to room temperature at 200 K/hr. Excess flux was dissolved in HNO₃ (aq) at up to 473 K. Black plate-like crystals resulted with dimensions of up to 0.134 x 0.097 mm and 0.061 x 0.048 mm for the Pb₃Rh_{5.93}Mn_{1.07}O₁₅ and Pb₃Rh_{4.74}Mn_{2.26}O₁₅ compositions, respectively.

Single-crystal X-ray diffraction data for Pb₃Rh_{5.93}Mn_{1.07}O₁₅ and Pb₃Rh_{4.74}Mn_{2.26}O₁₅ were collected at 173 K and 233 K respectively using a Bruker SMART APEXII CCD system and an Oxford Cryostream Cooler. A fine focus tube was used with an anode power of 50 KV at 30 mA, a crystal to plate distance of 6.0 cm, 512 x 512 pixels/frame, beam center (256.52, 253.16), ϕ/ω scan with step of 0.30°, exposure/frame of 10.0 s/frame, and

SAINT integration. An absorption correction was applied by SADABS. Crystal structures were solved by direct methods and refined with full-matrix least-squares method using the SHELXTL package. Further measurements to higher angles were carried out using an Oxford-Diffraction Xcalibur2 CCD diffractometer equipped with a Cryojet cooling device.

Electrical conductivity measurements were conducted by the conventional four-probe method over the temperature region 60-300 K. Magnetic susceptibility data were obtained with a Quantum Design PPMS ACMS magnetometer using a field of 0.5 T.

2.4 Effects of Bi substitution in $\text{Pb}_{3-x}\text{Bi}_x\text{Mn}_7\text{O}_{15}$

2.4.1 Introduction

In the work investigating $\text{Pb}_3\text{Rh}_7\text{O}_{15}$ by Mizoguchi et al., it was found that Bi could be substituted for Pb up to $x = 1.2$ for $\text{Pb}_{3-x}\text{Bi}_x\text{Rh}_7\text{O}_{15}$ phases [35]. Furthermore crystals of $\text{Pb}_{2.04}\text{Bi}_{0.96}\text{Rh}_7\text{O}_{15}$ composition were successfully grown in a $\text{Bi}_2\text{O}_3/\text{V}_2\text{O}_5$ flux. Thus after successful synthesis of the $\text{Pb}_3\text{Rh}_{7-x}\text{Mn}_x\text{O}_{15}$ solid solution we found it worthwhile to investigate the possibility of Bi substitution for Pb in $\text{Pb}_3\text{Mn}_7\text{O}_{15}$ which to the best of our knowledge has not currently been reported.

Possible $\text{Pb}_{3-x}\text{Bi}_x\text{Mn}_7\text{O}_{15}$ phases would allow for further investigation of the magnetic transitions reported for $\text{Pb}_3\text{Mn}_7\text{O}_{15}$ [36] by disrupting the $\text{Mn}^{3+}/\text{Mn}^{4+}$ ratio that likely important for the electronic and magnetic phenomena observed. In manganates possessing Mn^{3+} and Mn^{4+} mixed valency, antiferromagnetic superexchange interactions can occur between Mn^{3+} ions while ferromagnetic double exchange interactions can occur between Mn^{3+} and Mn^{4+} ions through the $\text{Mn}^{3+} - \text{O} - \text{Mn}^{4+}$ path.

Thus, Bi substitution is expected to influence both the electrical and magnetic phenomena by influencing any double and superexchange interactions present. The substitution may also give further insights into the structure of $\text{Pb}_3\text{Mn}_7\text{O}_{15}$ and the possibility of Jahn Teller activity of the Mn in Mn^{3+} state.

2.4.2 Results and Discussion

Synthesis of $\text{Pb}_{3-x}\text{Bi}_x\text{Mn}_7\text{O}_{15}$ was found to be successful up to $x = 0.2$. The lattice parameters of the orthorhombic structure were found to remain fairly stable as shown in figure 2.8. Only the $x = 0.05$ composition showed a significant change in the a parameter.

For every Bi^{3+} ion substituted for Pb^{2+} , one Mn^{4+} ion is reduced to a Mn^{3+} ion. Mn^{3+} (0.645 Å ionic radius) is larger than Mn^{4+} (0.53 Å ionic radius), so the observation of a slight increase in the ab plane was expected [41]. Furthermore, with smaller Bi^{3+} ions occupying the interlayer regions of the structure, a decrease in the c parameter was also expected. However, with the low substitution levels possible (≤ 0.2) this is not clearly evident as shown in figure 2.8.

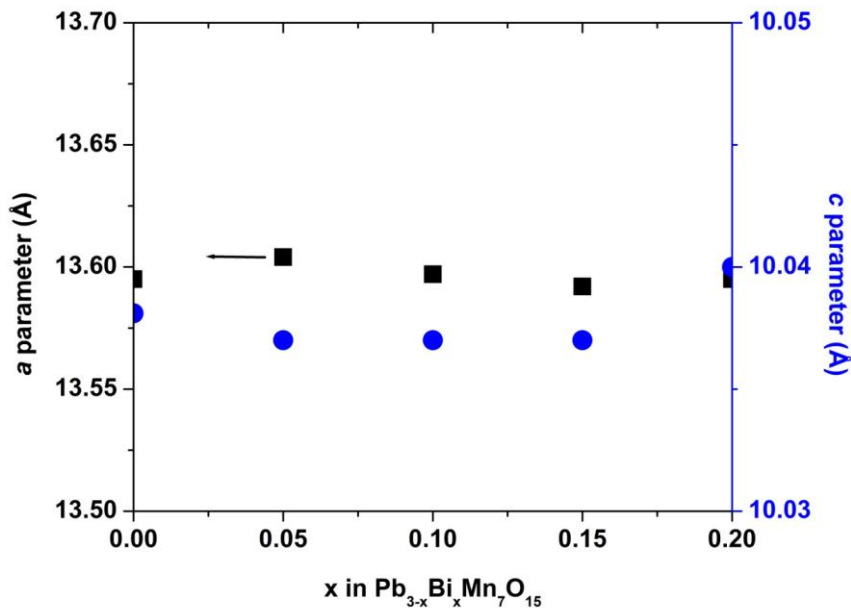


Figure 2.8. The lattice parameter trends for the $\text{Pb}_{3-x}\text{Bi}_x\text{Mn}_7\text{O}_{15}$ phases with $x \leq 0.2$

Figure 2.9 shows that the magnetic transitions at ~ 70 K, where the transition to long-range 3D antiferromagnetic order occurs, are maintained for x up to $x = 0.15$. As seen in the plot, the $x = 0.2$ sample shows dramatically different transitions at ~ 70 K, 40 K and 20 K.

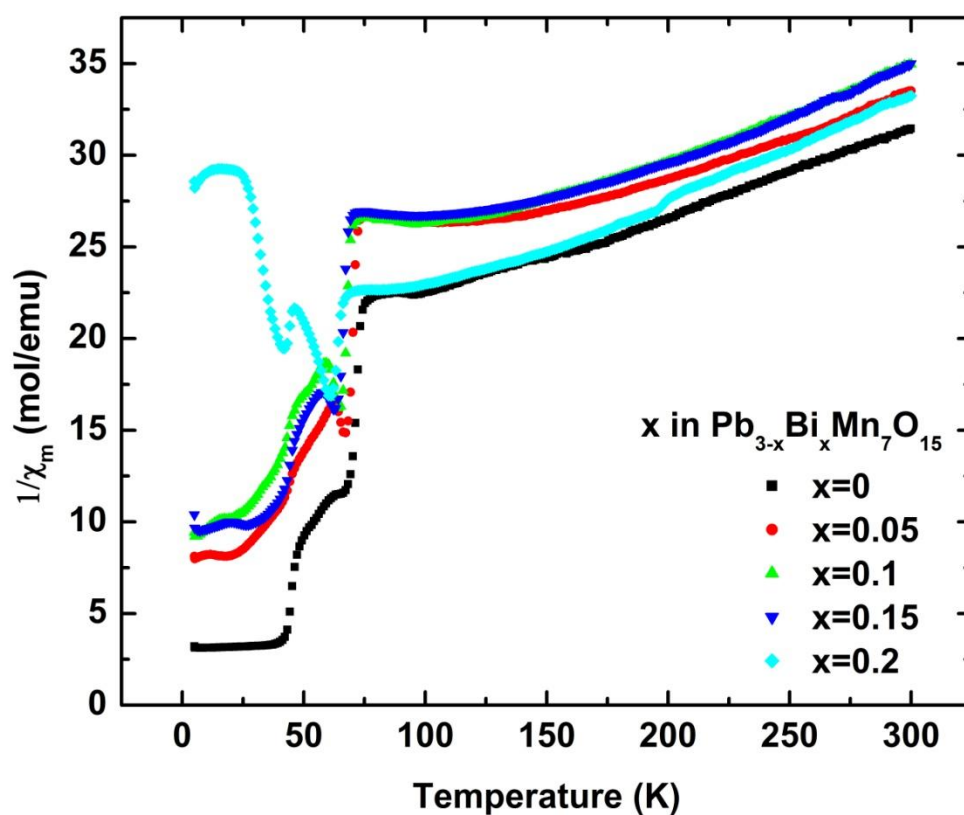


Figure 2.9. The magnetic susceptibility of $\text{Pb}_{3-x}\text{Bi}_x\text{Mn}_7\text{O}_{15}$ phases with $x \leq 0.2$ showing the dramatically different transitions at ~ 70 K, 40 K and 20 K for the $x = 0.2$ composition.

In attempting to investigate these transitions observed for the $x = 0.2$ composition further, we attempted to repeat the susceptibility measurements.

This was first repeated in a 0.5 T field similar to the initial measurement and then in a lower 0.25 T field. Figure 2.10 shows the field variation studies, which did not seem to lead to further revelations on the origin of the different transitions observed in the $x = 0.2$ sample.

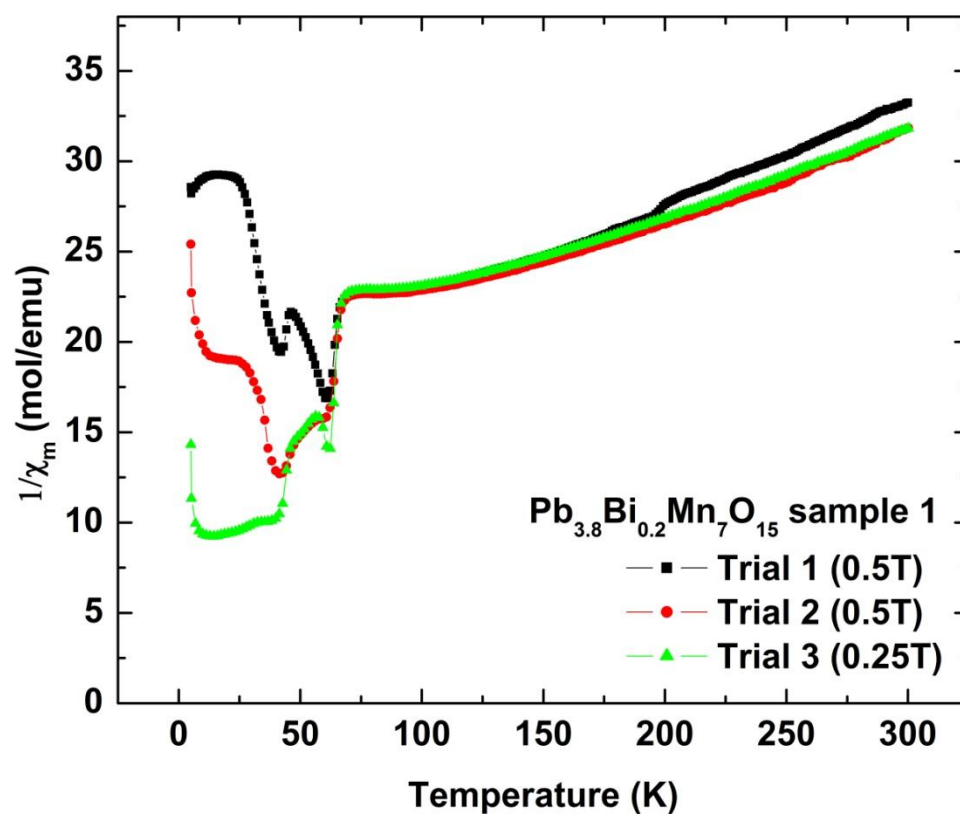


Figure 2.10. The magnetic susceptibility of $\text{Pb}_{2.8}\text{Bi}_{0.2}\text{Mn}_7\text{O}_{15}$ measured at the different fields shown.

Thus, a re-synthesis of the composition and a re-measurement of the susceptibility were performed to confirm the initial results observed. The new

$x = 0.2$ sample showed transitions similar to the parent $\text{Pb}_3\text{Mn}_7\text{O}_{15}$ and the other $\text{Pb}_{3-x}\text{Bi}_x\text{Mn}_7\text{O}_{15}$ compositions as shown in figure 2.11.

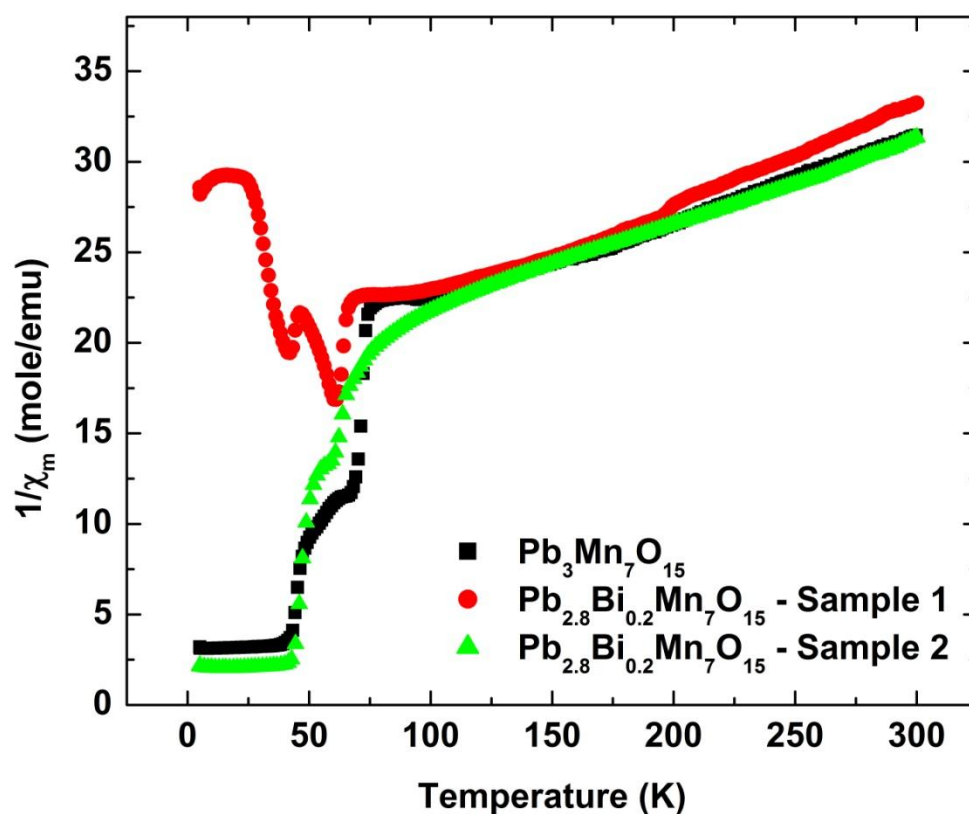


Figure 2.11. The magnetic susceptibility of the resynthesized $\text{Pb}_{2.8}\text{Bi}_{0.2}\text{Mn}_7\text{O}_{15}$ (sample 2) as compared to the original composition (sample 1) and the $\text{Pb}_3\text{Mn}_7\text{O}_{15}$ composition.

Thus it is likely that the original $x = 0.2$ sample possessed some minor impurities that were not easily detected in the x-ray patterns which led to the different magnetic properties exhibited. Nonetheless, we believe it is likely that the solubility range for Bi in $\text{Pb}_{3-x}\text{Bi}_x\text{Mn}_7\text{O}_{15}$ is $x < 0.2$.

Electrically, the low Bi substitution levels do not seem to influence the electronic properties of $\text{Pb}_3\text{Mn}_7\text{O}_{15}$ as shown in the plot depicting the evolution of electrical resistivity with temperature in figure 2.12.

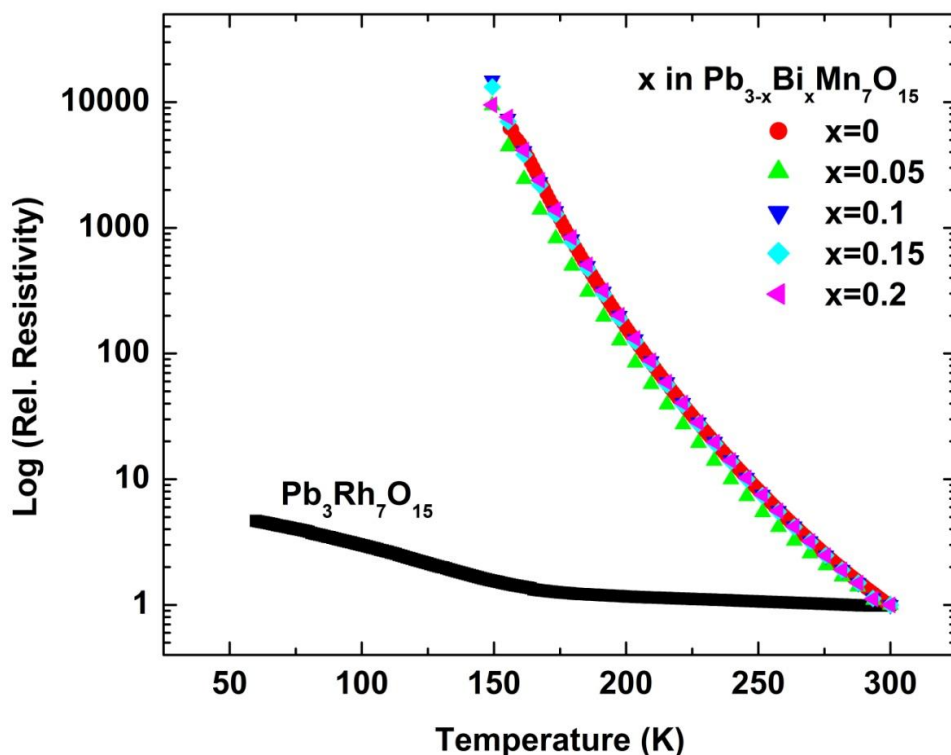


Figure 2.12. The electrical resistivity $\text{Pb}_{3-x}\text{Bi}_x\text{Mn}_7\text{O}_{15}$ compositions compared with that of $\text{Pb}_3\text{Rh}_7\text{O}_{15}$.

Hence, it is apparent the low substitution levels do not influence the $\text{Mn}^{3+}/\text{Mn}^{4+}$ ratio significantly to lead to notable changes in the magnetic and electronic properties of $\text{Pb}_3\text{Mn}_7\text{O}_{15}$. Furthermore, structurally it can be inferred that the hexagonal structure of $\text{Pb}_3\text{Rh}_7\text{O}_{15}$ is more tolerable to Bi substitution for Pb than the orthorhombic structure of $\text{Pb}_3\text{Mn}_7\text{O}_{15}$.

2.4.3 Conclusion

$\text{Pb}_3\text{Mn}_7\text{O}_{15}$ shows a significantly lower substitution range for Bi for Pb as compared to $\text{Pb}_3\text{Rh}_7\text{O}_{15}$ where crystals were able to be grown. This is likely a result of the different structures of the parent compositions. Current physical property measurements indicate that these low substitution levels have little effect on both the magnetic and electronic properties and hence little disruption to the $\text{Mn}^{3+}/\text{Mn}^{4+}$ ratio is inferred.

2.4.4 Experimental

Reactants were PbO (99.9% Aldrich), Bi_2O_3 (99.99% Aldrich), and Mn_2O_3 (98% Johnson Matthey). Stoichiometric amounts of the oxides were ground under ethanol in an agate mortar and pestle. Pelletized samples were placed in an alumina boat and heated to 1148 K. X-ray powder diffraction data were collected with a RIGAKU MINIFLEX II using Cu $K\alpha$ radiation and a graphite monochromator.

Electrical conductivity measurements were conducted by the conventional four-probe method over the temperature region 60-300 K. Magnetic susceptibility data were obtained with a Quantum Design PPMS ACMS magnetometer using a field of 0.5 T and 0.25 T.

2.5 References

- [1] I. Shaplygin, I. Prosychev, V. Lazarev, *Zh. Neorg. Khim.* 31 (1986) 2870.
- [2] G. Lunde, *Z. Anorg. Allg. Chem.* 163 (1927) 345.
- [3] J.M.D. Coey, *Acta Crystallogr., Sect. B: Struct. Sci.* 26 (1970) 1876.
- [4] R.D. Shannon, C.T. Prewitt, *J. Solid State Chem.* 2 (1970) 134–136.
- [5] J.W.M. Biesterbos, J. Hornstra, *J. Less Comm. Met.* 30 (1973) 121–125.
- [6] H. Leiva, R. Kershaw, K. Dwight, A. Wold, *Mater. Res. Bull.* 17 (1982) 1539–1544.
- [7] A. Roy, J. Ghose, *Mater. Res. Bull.* 33 (1998) 547–551.
- [8] T. Shimura, M. Itoh, T. Nakamura, *J. Solid State Chem.* 98 (1992) 198–200.
- [9] K.E. Stitzer, M.D. Smith, H.C. zur Loye, J. Darriet, *Chem. Commun.* (2001) 1680–1681.
- [10] J.B. Claridge, H.-C. zur Loye, *Chem. Mater.* 10 (1998) 2320–2322.
- [11] H. Mizoguchi, A.W. Sleight, M.A. Subramanian, *MRS Proceedings* 1148E (2008).
- [12] M.B. Robin, P. Day, *Adv. Inorg. Chem. and Radiochem.* 10 (1967) 247.
- [13] L. Pauling, *J. Am. Chem. Soc.* 51 (1929) 1010.
- [14] I.D. Brown, D. Altermatt, *Acta Crystallogr., Sect. B: Struct. Sci.* 41 (1985) 244–247.
- [15] M. Coey, *Nature* 430 (2004) 155–157.
- [16] E.J.W. Verwey, *Nature* 144 (1939) 327–328.
- [17] P.G. Radaelli, D.E. Cox, M. Marezio, S.-W. Cheong, *Phys. Rev. B* 55 (1997) 3015–3023.
- [18] H. Mizoguchi, W.J. Marshall, A.P. Ramirez, A.W. Sleight, M.A. Subramanian, *J. Solid State Chem.* 180 (2007) 3463–3468.
- [19] J.B. Goodenough, *Phys. Rev.* 100 (1955) 564–573.
- [20] A.D. McNaught, A. Wilkinson, *IUPAC Compendium of Chemical Terminology. The Gold Book.* (2nd Edition), Blackwell Science, 1997.
- [21] K. Renger, *Die Anf'angliche Suszeptibilit'at Von Eisen Und Magnetit in Abh'angigkeit Von Der Temperatur*, Zurich, 1913.
- [22] P. Weiss, K. Renger, *Arch. Elektrotechn.* 11 (1914) 406.
- [23] P. Weiss, R. Forrer, *Ann. Phys.* 12 (1929) 279.
- [24] I. Leonov, A.N. Yaresko, *J. Phys.: Condens. Matter* 19 (2007) 021001.
- [25] F. Walz, *J. Phys.: Condens. Matter* 14 (2002) R285–R340.
- [26] P.W. Anderson, *Phys. Rev.* 102 (1956) 1008–1013.
- [27] T. Yamada, K. Suzuki, S. Chikazumi, *Appl. Phys. Lett.* 13 (1968) 172.
- [28] J.P. Wright, J.P. Attfield, P.G. Radaelli, *Phys. Rev. B* 66 (2002) 214422.
- [29] B. Darriet, M. Devalette, B. Latourrette, *Acta Crystallogr., Sect. B: Struct. Sci.* B34 (1978) 3528.
- [30] R.E. Marsh, F.H. Herbststein, *Acta Crystallogr., B: Struct. Sci.* 39 (1983) 280–287.
- [31] Y. Le Page, L.D. Calvert, *Acta Crystallogr., Sect. C: Cryst. Struct. Commun.* 40 (1984) 1787–1789.

- [32] J.C.E. Rasch, D.V. Sheptyakov, J. Schefer, L. Keller, M. Boehm, F. Gozzo, N.V. Volkov, K.A. Sablina, G.A. Petrakovskii, H. Grimmer, K. Conder, J.F. Löffler, *J. Solid State Chem.* 182 (2009) 1188–1192.
- [33] A.W. Sleight, H.Y. Chen, J.L. Gillson, ACS/CSJ Chemical Congress, Honolulu, HI, April 1-6, 1979, American Chemical Society, Washington, DC. (1979) 75.
- [34] P.J. Omaly, R. Kohlmuller, P. Batail, R. Chevalier, *Acta Crystallogr., Sect. B: Struct. Sci.* B36 (1980) 1040.
- [35] H. Mizoguchi, A.P. Ramirez, T. Siegrist, L.N. Zakharov, A.W. Sleight, M.A. Subramanian, *Chem. Mater.* 21 (2009) 2300–2305.
- [36] N.V. Volkov, K.A. Sablina, O.A. Bayukov, E.V. Eremin, G.A. Petrakovskii, D.A. Velikanov, A.D. Balaev, A.F. Bovina, P. Böni, E. Clementyev, *J. Phys.: Condens. Matter* 20 (2008) 055217.
- [37] N.V. Volkov, K.A. Sablina, E.V. Eremin, P. Böni, V.R. Shah, I.N. Flerov, A. Kartashev, J.C.E. Rasch, M. Boehm, J. Schefer, *J. Phys.: Condens. Matter* 20 (2008) 445214.
- [38] N. Khosrovani, A.. Sleight, *Int. J. Inorg. Mater.* 1 (1999) 3–10.
- [39] A.L. Allred, *J. Inorg. Nucl. Chem.* 17 (1961) 215–221.
- [40] Y. Miyahara, *J. Phys. Soc. Jpn.* 32 (1972) 629–634.
- [41] R.D. Shannon, *Acta Cryst.* A32 (1976) 757 – 767.

CHAPTER 3

Investigating the thermoelectric properties of compositionally controlled oxide materials

3.1 Abstract

Perovskite materials provide a great platform for structure-property relationship studies and are likely to lead to a great deal of new technologically relevant materials. On the otherhand, thermoelectric materials have been at the forefront of materials research for the last few decades and with rising demand for new energy sources they will likely continue to be a field of interest.

SrRuO_3 a well known orthorhombic perovskite that shows itinerant ferromagnetism was synthesized via solid state reaction and Sr substitution by K, Rb and Cs was attempted. Low substitution phases were synthesized and characterized. All the phases show decreased ferromagnetic T_c temperatures and increased electrical resistivity. These properties are the result of the distorted nature of the perovskite structure. Seebeck coefficients were found to be relatively unchanged by the low substitution levels.

$\text{Sr}_{2-x}\text{La}_x\text{CoRuO}_6$ phases possessing the perovskite structure offer an interesting system where control of the B-site via A-site substitution can lead to significant changes in thermoelectric performance. A thermoelectric analysis of these phases currently shows $\text{Sr}_{1.1}\text{La}_{0.9}\text{CoRuO}_6$ with the best thermoelectric performance that can likely be further improved via optimizing processing techniques.

$(\text{RhV})_{1+x}\text{Ti}_{1-2x}\text{O}_6$ phases were also prepared by solid state reaction and found to crystallize in the rutile structure. All of the compositions appear to adopt the disordered trirutile structure. The phases were shown to be semiconducting with lower Ti content leading to higher conductivity. Seebeck coefficient measurements show electron carrier dominance and the carrier concentration is found to be dependent on Ti content. Electron carriers appear to become diminished at higher temperatures.

Publications based on this chapter:

1. Gatimu, A.J., Sleight, A.W., Subramanian, M.A. Structure-Property relationships in $\text{Sr}_{1-x}\text{M}_x\text{RuO}_3$ ($\text{M} = \text{K}, \text{Rb}, \text{Cs}$) perovskite oxides. (In progress).
2. Gatimu, A.J., Biswas, K., Sleight, A.W., Subramanian, M.A. Effect of substitution on the thermoelectric properties of $\text{Sr}_2\text{CoRuO}_6$. (In progress).
3. Gatimu, A.J., Biswas, K., Aun-anong, R., Sleight, A.W., Subramanian, M.A. Investigating the thermoelectric properties of the $(\text{RhV})_{1+x}\text{Ti}_{1-2x}\text{O}_6$ solid solution with the rutile-type structure. (In progress).

3.2 Introduction

3.2.1 Cation Arrangements in Perovskite Structures

Perovskites are the backbone of more than 20 Billion dollars per year generated by the electroceramics industry [1]. The aristotype (idealized, most symmetric) perovskite structure has a general formula ABX_3 with the $Pm\bar{3}m$ space group representing cubic symmetry. The A represents a large electropositive cation, B represents a small transition metal or a main group ion while X is commonly an oxide or halide ion. The structure consists of a framework of corner-shared BX_6 octahedra in three dimensions with the larger A-site cation occupying a 12-coordinate cubo-octahedral site.

Two factors make perovskites incredibly rich in properties and often choice materials for chemists to investigate. First is that distortions from the idealized structure are very common. In fact there are only about half a dozen perovskites with the idealized cubic structure [2]. These distortions influence the physical properties immensely.

The distortions primarily involve tilting of the BX_6 octahedra usually triggered by a smaller than ideal A-site cation for the cubo-octahedral site [3–7]. These distortions can influence conduction band widths and superexchange interactions [8,9]. Other possible distortions include cooperative Jahn-Teller (COJT) distortions, occurring when specific Jahn-Teller active ions like Mn^{3+} and Cu^{2+} are present, influencing orbital ordering. Second order Jahn-Teller (SOJT) distortions, occurring where high valent d^0 cations on the B-site and/or

lone pairs are present on the A-site, allow for the realization of ferroelectricity and piezoelectricity [10].

A second factor resulting in a variety of properties observed in perovskites is that perovskites allow for significant substitution with all three sites of the ideal structure available for chemical substitution. On the anion site, different anions and vacancies are possible, while a variety of cations can be on the A and B-sites. These substitutions can adopt a variety of arrangements.

If the cations are ordered at only one site, the compounds are commonly termed “double perovskites” while if the ordering occurs on both A and B-sites, the compounds are referred to as complex or quadruple perovskites [11]. Generally, B-site cations order more readily than A-site cations, with clear differences in how they order.

3.2.1.1 B-Site Ordering

Common B-site ordered perovskites have the general formulae $A_2BB'_2X_6$ and $A_3BB'_2X_9$ in which B and B' represent different octahedral cations in different crystallographic sites. A general rule for perovskite oxides is that when oxidation states of B and B' differ by less than two, a disordered/random arrangement is observed, while a difference of greater than two almost always produces an ordered arrangement. If the difference happens to be exactly two, either a disordered, partially ordered or fully

ordered arrangement can occur [10]. These will be dictated by other factors such as size difference and bonding preferences.

In addition to being disordered, there are three other sublattice types (patterns of ordering) that are known to occur on the B-site as shown in figure 3.1. These are Rock salt, Columnar and Layered ordering.

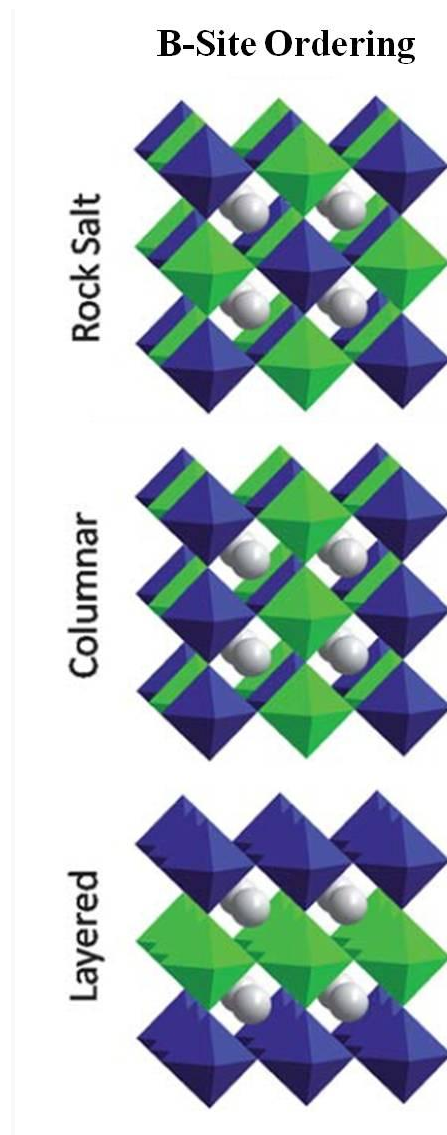


Figure 3.1. B-site ordering in perovskites. The most symmetric type of ordering is Rock salt ordering and can be considered as 0-Dimensional. Columnar ordering (1-Dimensional) and layered ordering (2-Dimensional) are less symmetric and also less common in B-site ordered perovskites. Adapted from [10].

A vast majority of $A_2BB'X_6$ perovskites have B and B' cations ordered in a rock salt sublattice. In fact, there are 400 reported examples of B-site rock salt ordered $A_2BB'X_6$ perovskites [12,13]. As the name suggests, the B and B' cations distribute in a pattern similar to cation and anion positions in a traditional rock salt structure (e.g NaCl). Thus each $B'X_6$ octahedron is isolated from all other $B'X_6$ octahedra by B cations as shown in figure 3.1. This arrangement is the most symmetric for B-site cations to adopt.

Perovskite oxides with rock salt sublattices on the B-site tend to have cubic (e.g Sr_2CuWO_6) or monoclinic (e.g Sr_2LuRuO_6) unit cells as shown in table 3.1. The monoclinic unit cell results from rotations of the BO_6 octahedra about the [011] and [100] cubic directions. Rock salt ordering in a cubic cell can be identified by a doubling of the unit cell parameters as suggested by table 3.1, while rock salt ordering in a monoclinic unit cell can be identified by systematic absences in X-ray diffraction patterns.

B-site Sublattice Type	Cell Parameters	Crystal System	Space Group
Disordered	$1a_c \times 1a_c \times 1a_c$	Cubic	$Pm\bar{3}m$
	$\sqrt{2}a_c \times \sqrt{2}a_c \times 2a_c$	Orthorhombic	Pbnm
Rock salt	$2a_c \times 2a_c \times 2a_c$	Cubic	$Fm\bar{3}m$
	$\sqrt{2}a_c \times \sqrt{2}a_c \times 2a_c$	Monoclinic	$P2_1/n$
Layered	$2a_c \times 2a_c \times 2a_c$	Monoclinic	$P2_1/m$

Table 3.1. Three common arrangements of B cations in perovskite oxides. A comparison of the cell parameters, crystal systems and common space groups is shown, with a_c representing the unit cell parameter of the ideal cubic ABX_3 perovskite structure.

The charge difference between B and B' is critical in explaining why the vast majority of perovskite oxides favor rock salt ordering. Rock salt ordering maximizes the separation of the more highly charge B/B' cations. In other ordering sublattice types this is not the case and electrostatic repulsions are involved.

Nonetheless, the effect of ionic size is also very significant in determining ordering the B-site cations adopt. Figure 3.2 allows for comparison of the effect of ionic size and ionic charge on the B-site sublattice [14]. The plot suggests that for stoichiometric double perovskite oxides, the cation arrangement on the B-site is influenced primarily by the ionic charge

difference and secondarily by the ionic size difference.

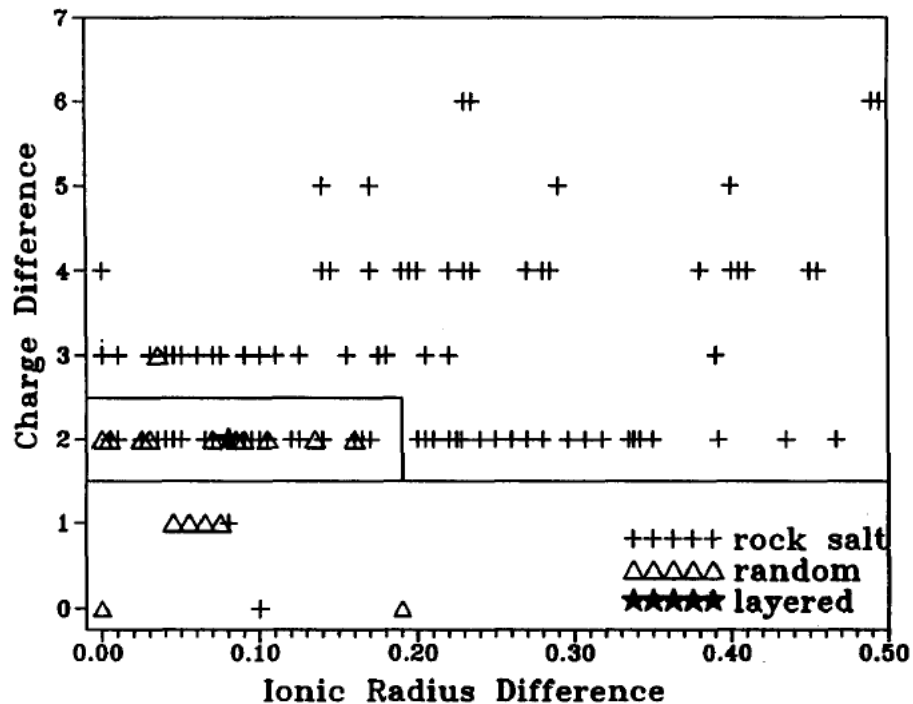


Figure 3.2. A plot of Charge Difference vs. Ionic Radius Difference for stoichiometric double perovskites. The plot shows that the type of B-site ordering observed is primarily influenced by the charge difference between the B cations. The plot is adapted from work by Anderson et al. [14].

Columnar ordering on the B-site of perovskites is rare with examples including $\text{LaCa}(\text{Mn}^{3+}\text{Mn}^{4+})\text{O}_6$ and $\text{NdSr}(\text{Mn}^{3+}\text{Mn}^{4+})\text{O}_6$ [15–17]. As suggested by these examples, the columnar ordering is driven by charge ordering in mixed valent perovskites. The sublattice type is also stabilized by lattice strains resulting from first order Jahn-Teller (FOJT) distortions of specific B cations (e.g Mn^{3+}) [10].

$\text{A}_3\text{BB}'_2\text{X}_9$ perovskites showing ordering on the B-site tend to show layered ordering. This 1:2 (B cation ratio) ordering is favored when SOJT distortions are possible allowing for bonding instabilities resulting from the

creation of two chemically distinct anion sites to be partially relieved. Layered ordering on the B-sites in $A_2BB'X_6$ (1:1) perovskites (e.g in Pr_2CuSnO_6) is also stabilized by FOJT distortions (of the Cu^{2+} in Pr_2CuSnO_6 example). Layered ordering can be distinguished from a disordered arrangement by the enlarged unit cell, lattice parameters and also by certain peak presences and absences in the X-ray diffraction patterns ([14] for more details).

3.2.1.2 A-Site Ordering

A-site ordering is not common in $AA'B_2X_6$ and $AA'BB'X_6$ perovskites. This results as differences in oxidation states for A-site cations tend to be much lower than for B-site cations. In B-site cations, the oxidation state differential can be as large as seven such as in Sr_2LiReO_6 , while most A-site oxidation state differentials are limited to two or less [10]. Rock salt, columnar and layered ordering on the A-site for $AA'B_2X_6$ perovskites is shown in figure 3.3.

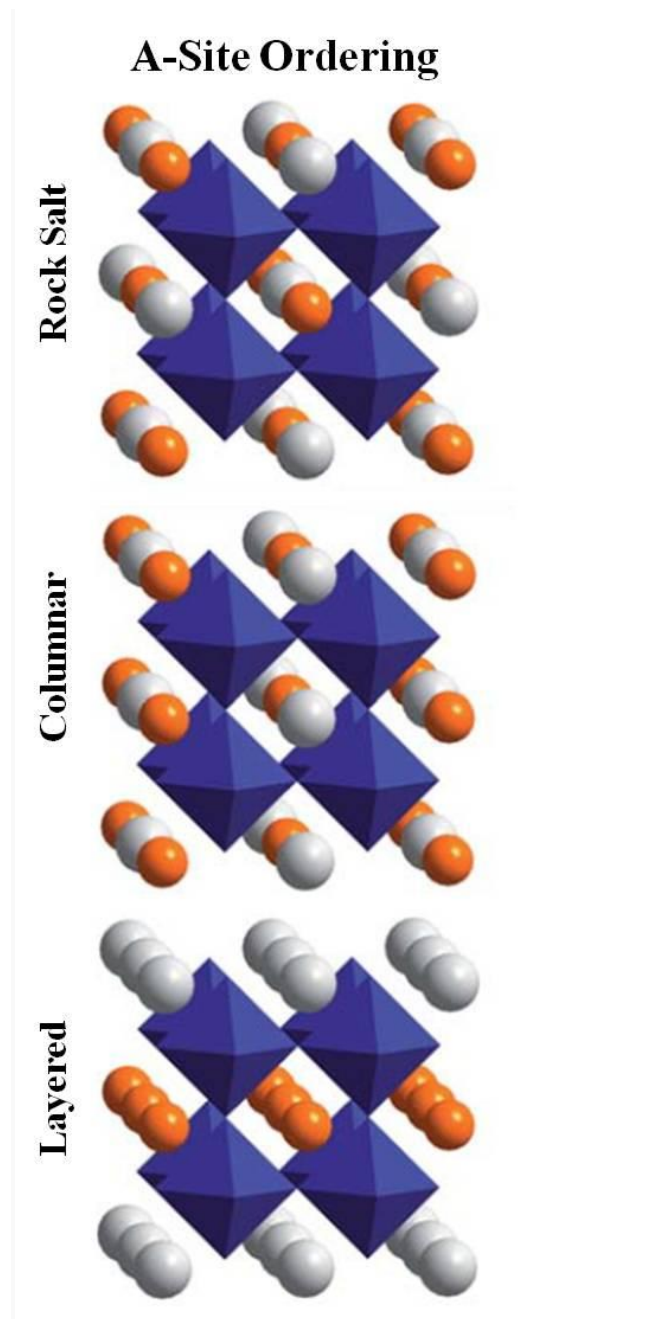


Figure 3.3. A-site ordering in $AA'B_2X_6$ perovskites. Rock salt, columnar and layered ordering are shown for $AA'B_2X_6$ perovskites. In comparison to B-site ordering, A-site ordering tends to prefer a layered sublattice type over rock salt sublattice type. Adapted from [10].

Unlike B-site ordering, A-site ordering tends to prefer a layered sublattice type over rock salt ordering. Examples include YBaMn_2O_5 and NaLaMgWO_6 . This can be explained by considering the anion sites and environments. Layered ordering on the B-site leads to chemically distinct anion environments in which the anions are over-bonded, and the cations under-bonded in the absence of distortions. This is a violation of Linus Pauling's fifth rule stating that all ions of the same type should have the same environment if possible [18].

Similarly, layered ordering on the A-site leads to distinct anion environments, however, the anion is capable of displacing depending on the size difference of A and A'. Despite this, SOJT distortions of the B cations and rock salt ordering on the B-sites are usually coupled with the layered ordering as they play a role in stabilizing the ordering. Other factors that stabilize layered A-site ordering are larger size and charge differences in A and A', A-site vacancies coupled with SOJT distortions on the B-site cations, and the presence of octahedral tilting.

Columnar ordering like rock salt ordering is rare on the A-site, but when present in a perovskite like $\text{CaFeTi}_2\text{O}_6$, it is stabilized by larger size and charge differences between A and A' and also by the presence of octahedral tilting.

3.3 Structure-Property relationships in $\text{Sr}_{1-x}\text{M}_x\text{RuO}_3$ ($\text{M} = \text{K}, \text{Rb}, \text{Cs}$) perovskite oxides

3.3.1 Introduction

Perovskite oxides continue to generate a wealth of interest within the material science community with new properties still being discovered and applications realized. These discoveries tend to originate from detailed structural studies of the perovskite structure. The ideal ABO_3 perovskite structure is described by a cubic unit cell with corner sharing BO_6 octahedra on the corners of the cubic unit cell and the larger A cations in the twelve-fold coordination site at the center of the unit cell. SrTiO_3 possesses this idealized cubic structure defined by $\text{Pm}\bar{3}\text{m}$ space group [3].

Nonetheless, most perovskite structures are distorted from this cubic structure as a result of varying A and B-site cation sizes from those required for the ideal cubic structure. In the case where the A cation size is decreased from ideality, the perovskite structure distorts towards a GdFeO_3 -type structure that is orthorhombic. This distorted structure involves a framework of corner-shared BO_6 octahedra that are tilted and rotated to compensate for the smaller cation in the A-site (figure 3.4). This results in a zig-zag linking of the BO_6 octahedra and variations in the B-O-B angle and A-O distances depending on the level of orthorhombic distortion. With regard to the A-O distances, the A-O distances separate into two groups (8 long, 4 short) with the difference in the two increasing with level of distortion [19].

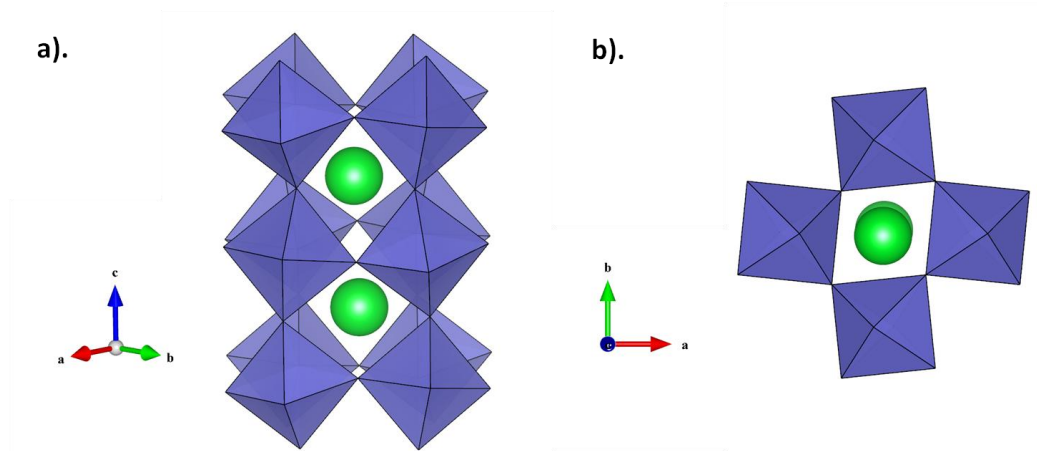


Figure 3.4. Orthorhombic perovskite structure resulting from distortions of the ideal cubic structure when the A cation is smaller than that required for the aristotype cubic structure. Tilting of the BO₆ octahedra is visible in (a) while (b) is a projection along the *c*-axis showing the rotations of the octahedra.

Well studied systems with the GdFeO₃-type structure have included the Ru perovskites, ARuO₃ (A = Sr, La, Ca, Pr) with key structure – property correlations being determined by investigators [19–21]. The level of distortion of the perovskite has been related to the A cation size and this has then been shown to have effects on the magnetic and electrical properties of the perovskites [20,21]. SrRuO₃ being one of the least distorted orthorhombic perovskites has been of great interest particularly because of the ferromagnetic interactions observed at up to a Curie temperature (*T_c*) of 160 K [19,22,23]. The origins of this high *T_c* have been motivation for many investigations involving Sr substitution. Substitution with M³⁺ cations such as La³⁺ and Pr³⁺ leads to a lowering of the *T_c* and eventual conversion to antiferromagnetism in the La substitution case [24,25]. Substitution with M²⁺ ions like Ca²⁺ has also been undertaken and this has also led to a suppression of the *T_c* [19,26]. The

suppression has been suggested to result from the higher acidic nature of Ca^{2+} , and thus greater ability to compete with Ru for oxygen anion orbitals; ultimately minimizing the superexchange interactions that drive the ferromagnetism [19,27].

Investigations attempting to achieve higher a T_c for SrRuO_3 as well as detailed studies on the complex ferromagnetism continue to be undertaken [28,29]. Few investigations have looked into the effects of substituting alkali metals for Sr in SrRuO_3 . In the following section, results from Sr substitution with K, Rb, and Cs are discussed. Structural, electrical and magnetic properties are reviewed.

3.3.2 Results and Discussion

The X-ray diffraction (XRD) patterns in figure 3.5 show the single phases that were synthesized. It is clear that in all three substitutions the solubility limits for the solid solution are low with $x \leq 0.3$ for $\text{Sr}_{1-x}\text{K}_x\text{RuO}_3$ and $x \leq 0.1$ for $\text{Sr}_{1-x}\text{Rb}_x\text{RuO}_3$ and $\text{Sr}_{1-x}\text{Cs}_x\text{RuO}_3$. The larger solubility range with K indicates that of the three alkali metals being substituted, K is the most suitable to replace Sr in the cubo-octahedral site of the perovskite structure. Some preliminary tolerance factor calculations show that with increasing K content the tolerance factor increases slightly, from 0.93 for SrRuO_3 to 0.96 for $\text{Sr}_{0.7}\text{K}_{0.3}\text{RuO}_3$. However for the Rb and Cs doped samples the tolerance factors are higher. This may hint as to why the higher Rb and Cs content cannot be achieved in the orthorhombic structure.

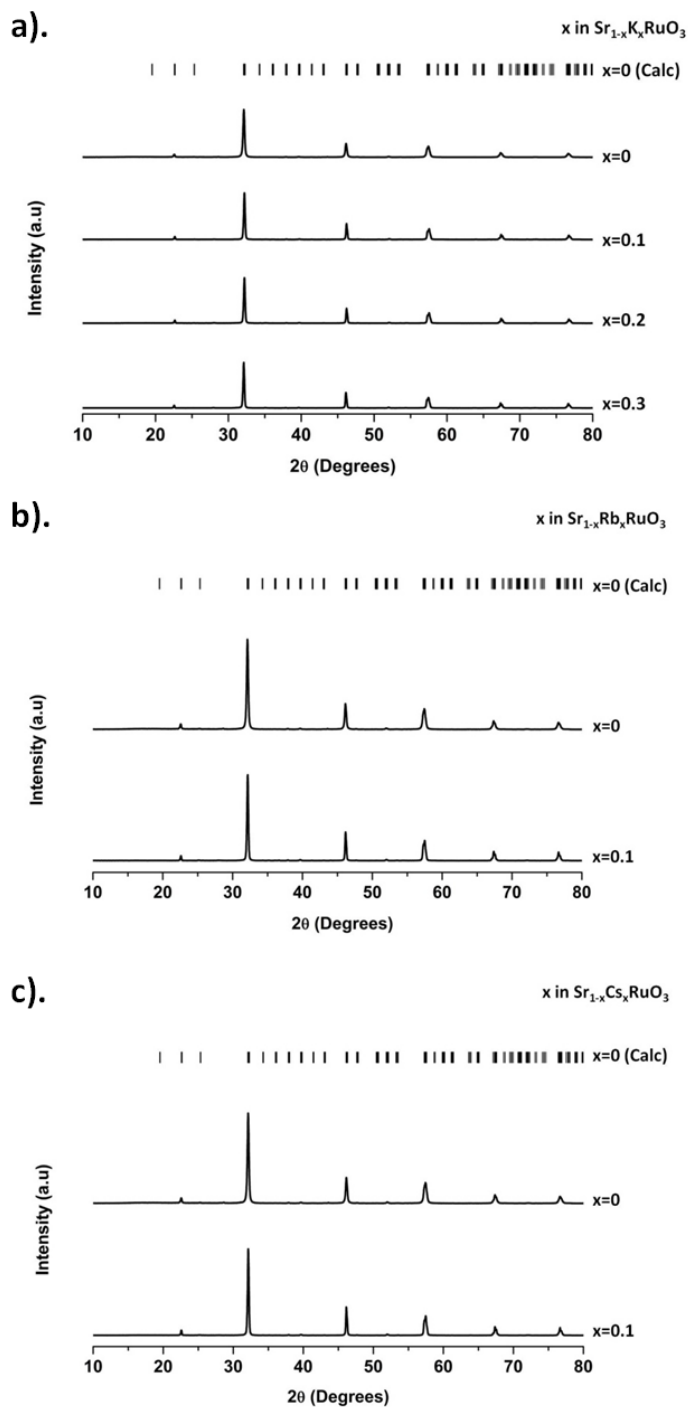


Figure 3.5. XRD patterns of $\text{Sr}_{1-x}\text{M}_x\text{RuO}_3$ ($M = \text{K}, \text{Rb}, \text{Cs}$) phases. The patterns show that only low solubility can be achieved for all three alkali metals with $x \leq 0.3$ for $\text{Sr}_{1-x}\text{K}_x\text{RuO}_3$ and $x \leq 0.1$ for $\text{Sr}_{1-x}\text{Rb}_x\text{RuO}_3$ and $\text{Sr}_{1-x}\text{Cs}_x\text{RuO}_3$.

Figure 3.6 and 3.7 give an indication of how these substitutions influence the orthorhombic unit cell. In figure 3.6, the a and b parameters are shown. In $\text{Sr}_{1-x}\text{K}_x\text{RuO}_3$, both the a and b parameters appear to decrease upon initial K substitution but increase for the $\text{Sr}_{0.7}\text{K}_{0.3}\text{RuO}_3$ composition. As is clearly evident, the decrease and increase is more pronounced for the b parameter than the a parameter. The $\text{Sr}_{1-x}\text{Rb}_x\text{RuO}_3$ substitution shows the a parameter staying relatively constant while the b parameter decreases slightly with Rb substitution. The $\text{Sr}_{1-x}\text{Cs}_x\text{RuO}_3$ substitution shows the a parameter remaining relatively constant while the b parameter decreases slightly. Thus very similar lattice behaviors are observed in the Rb and Cs substitutions. In figure 3.7, the c parameter and cell volume are shown. Similar to the a and b parameters, the c parameter and cell volume of the $\text{Sr}_{1-x}\text{K}_x\text{RuO}_3$ solid solution also initially decrease and then increase at the $x = 0.3$ composition. However in the $\text{Sr}_{1-x}\text{Rb}_x\text{RuO}_3$ solid solution the c parameter remains relatively constant while the cell volume decreases; while in the $\text{Sr}_{1-x}\text{Cs}_x\text{RuO}_3$ solid solution both the c parameter and cell volume decrease with substitution.

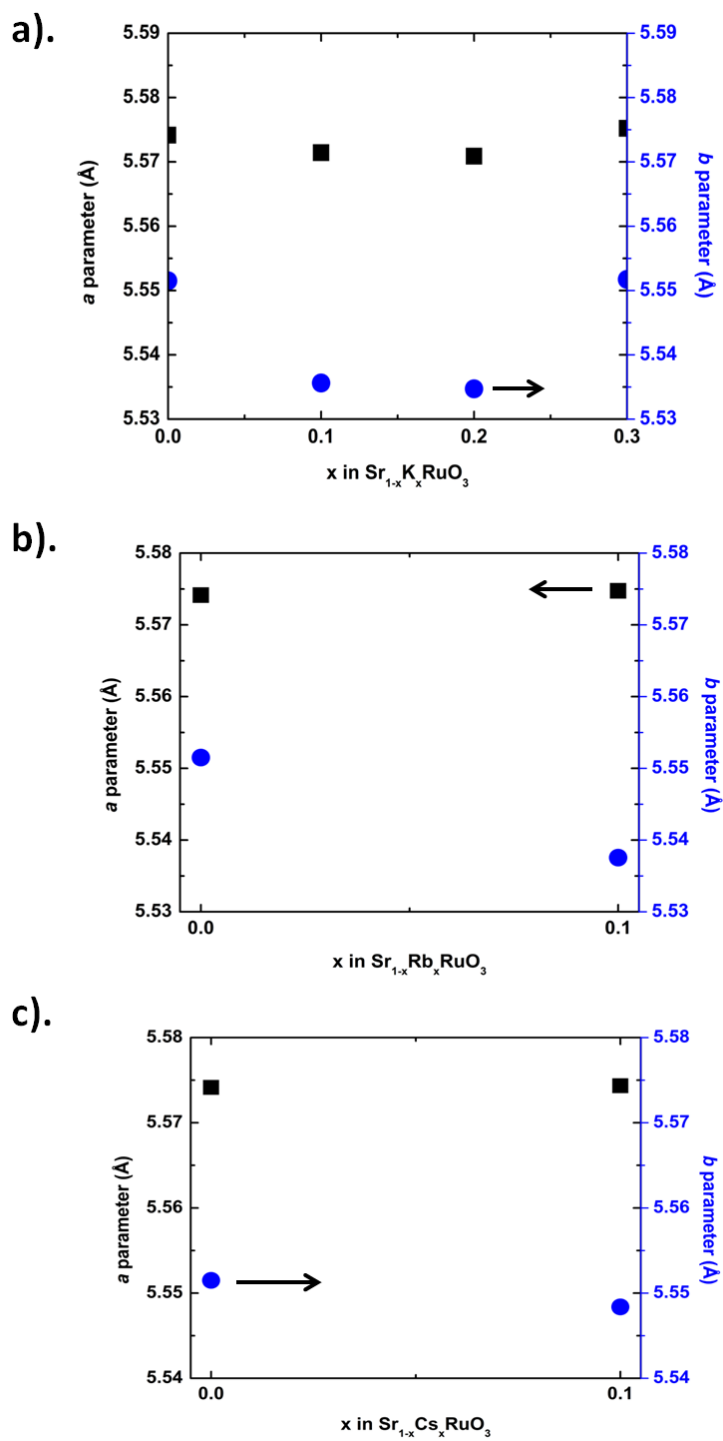


Figure 3.6. The evolution of the a and b cell parameters for the $\text{Sr}_{1-x}\text{K}_x\text{RuO}_3$ (a), $\text{Sr}_{1-x}\text{Rb}_x\text{RuO}_3$ (b) and $\text{Sr}_{1-x}\text{Cs}_x\text{RuO}_3$ (c) phases.

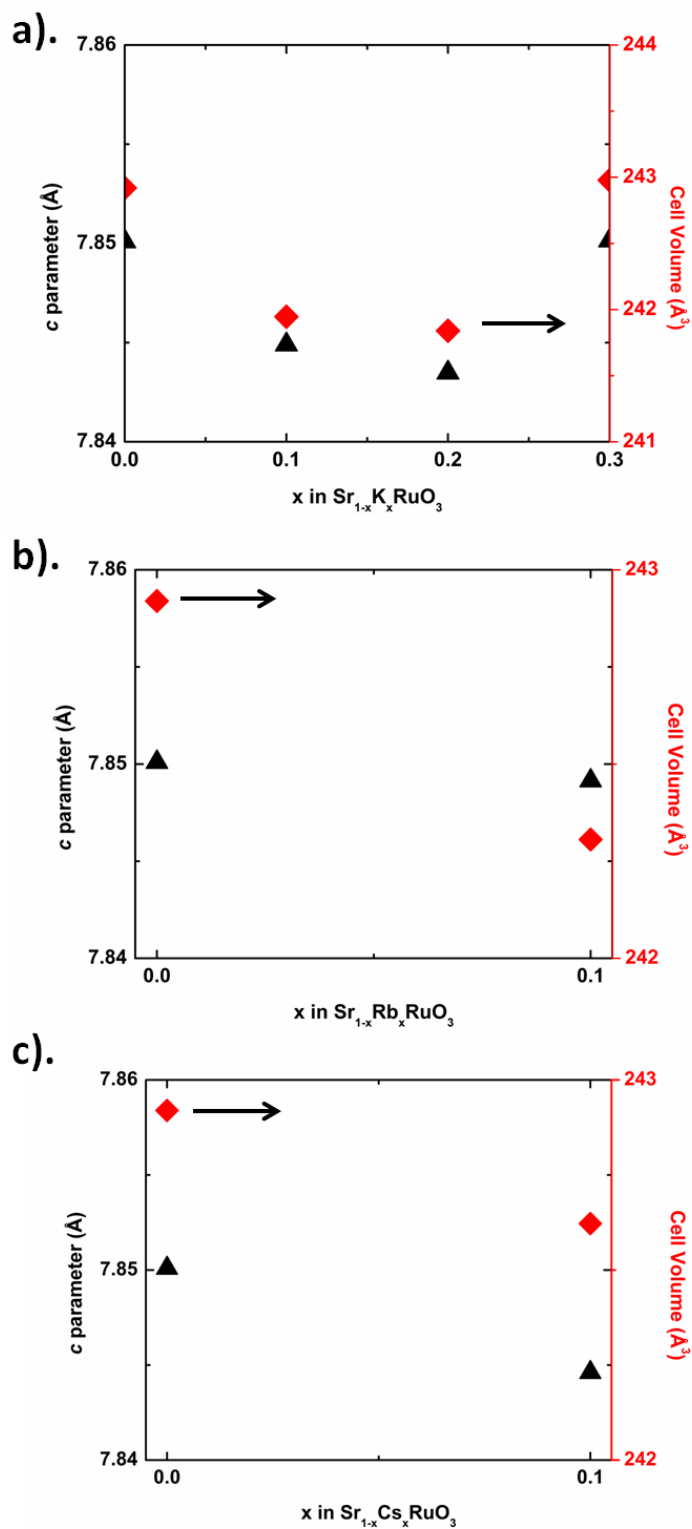


Figure 3.7. The evolution of the c cell parameter and cell volume for the $\text{Sr}_{1-x}\text{K}_x\text{RuO}_3$ (a), $\text{Sr}_{1-x}\text{Rb}_x\text{RuO}_3$ (b) and $\text{Sr}_{1-x}\text{Cs}_x\text{RuO}_3$ (c) phases.

In figures 3.8-3.10 the Time of Flight neutron diffraction data is shown. As can be seen in all the patterns and the refinement statistics, all the compositions fit well to the orthorhombic Pbnm space group. Sr occupancy in all the refined samples was found to be greater than 0.9 indicating that less alkali metal than initially believed was substituting for Sr. Thus the A-site of SrRuO_3 is found to be not as accommodating to alkali metal substitution as initially expected.

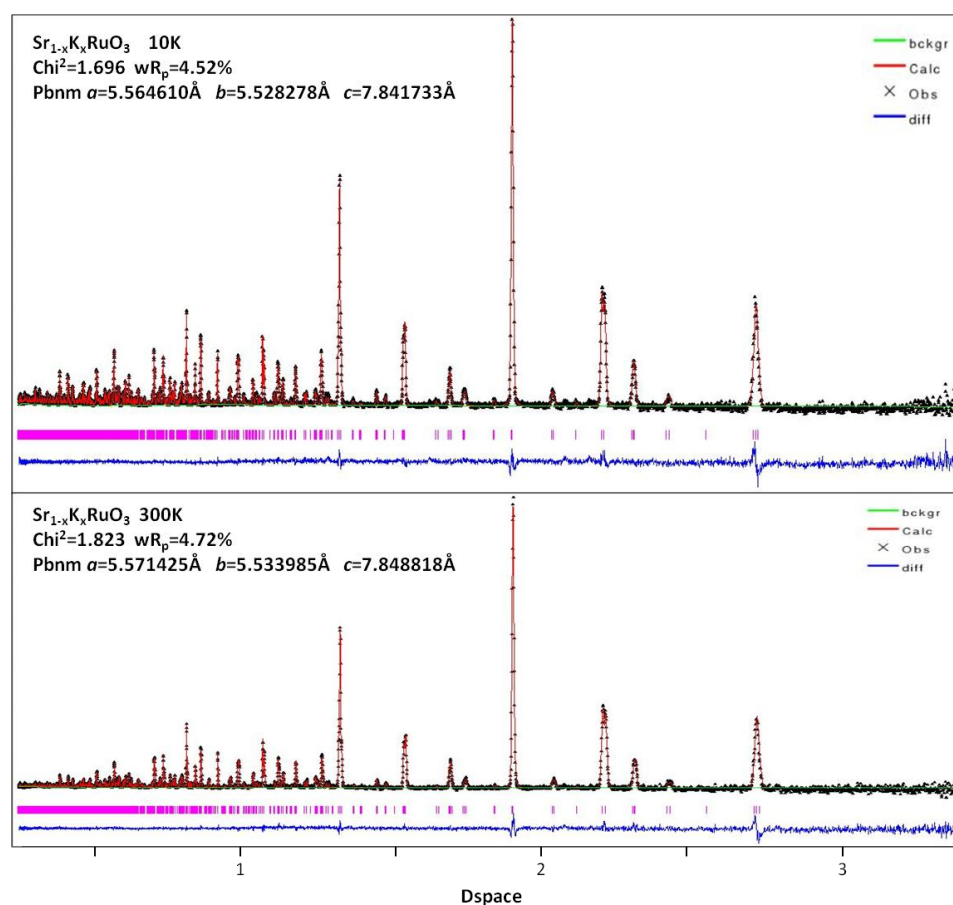


Figure 3.8. Time of flight neutron diffraction data for the $\text{Sr}_{0.9}\text{K}_{0.1}\text{RuO}_3$ composition collected at 10K and 300K. Rietveld refinement statistics determined by GSAS software are shown. Data was collected at Oak Ridge National Laboratory.

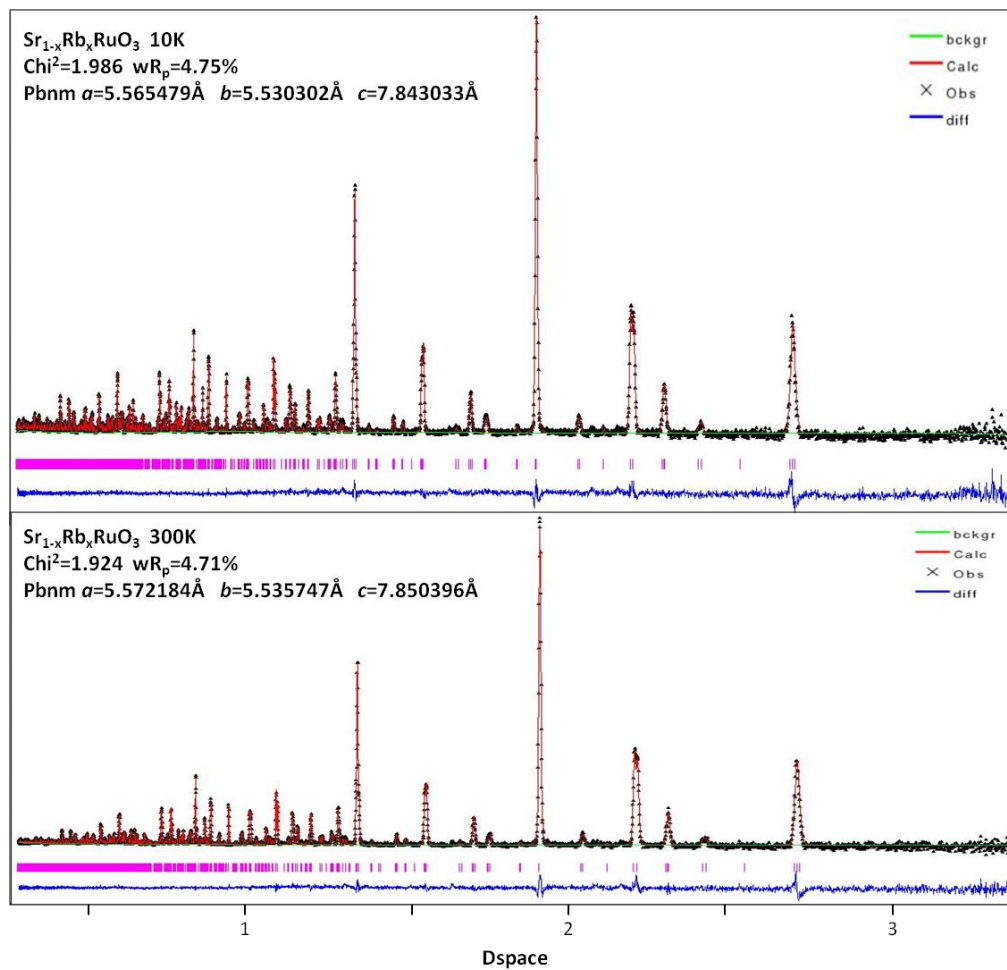


Figure 3.9. Time of flight neutron diffraction data for the $\text{Sr}_{0.9}\text{Rb}_{0.1}\text{RuO}_3$ composition collected at 10K and 300K. Rietveld refinement statistics determined by GSAS software are shown. Data was collected at Oak Ridge National Laboratory.

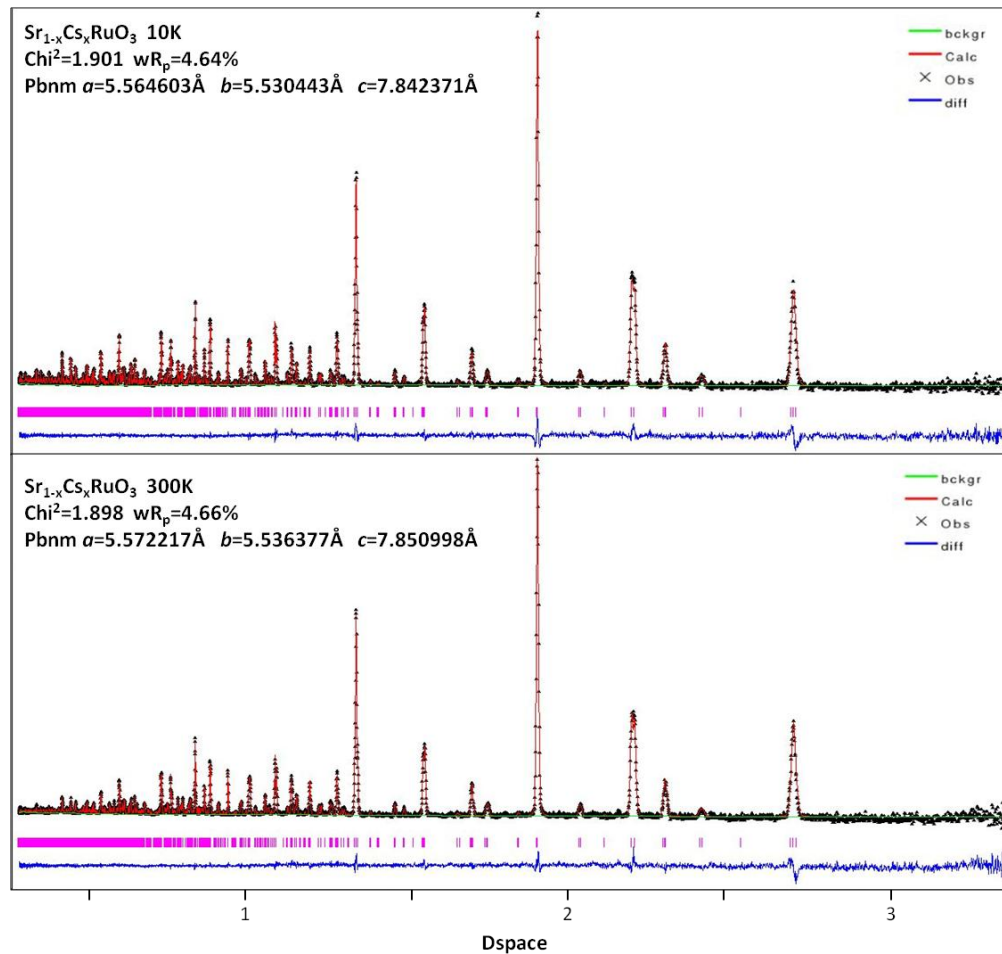


Figure 3.10. Time of flight neutron diffraction data for the Sr_{0.9}Cs_{0.1}RuO₃ composition collected at 10K and 300K. Rietveld refinement statistics determined by GSAS software are shown. Data was collected at Oak Ridge National Laboratory.

In figure 3.11, the magnetic susceptibility of the three solid solutions are depicted. In all the three solid solutions it is clear that Sr substitution leads to a decrease of the Curie temperature (T_c). In Sr_{1-x}K_xRuO₃, with increasing K content, the T_c decreases further. This decrease in T_c indicates a weakening of the ferromagnetic interactions with Sr substitution. This can be related to the effects of substitution on the Ru – O interactions. Substituting Sr²⁺ with a M¹⁺

cation was initially expected to favor an increase in the strength of Ru – O interactions as the A site would be less electropositive and thus less able to compete with Ru for oxygen electrons. Furthermore, the Ru⁵⁺ cations resulting from the substitution would allow for stronger Ru – O interactions and would imply three unpaired electrons in the Ru t_{2g} levels able to participate in ferromagnetic band interactions. These Ru – O interactions are expected to lead to the ferromagnetism observed [24]. Thus, the substitutions were expected to possibly strengthen the ferromagnetism and perhaps lead to an increase in T_c . The fact that this is not the case is very intriguing.

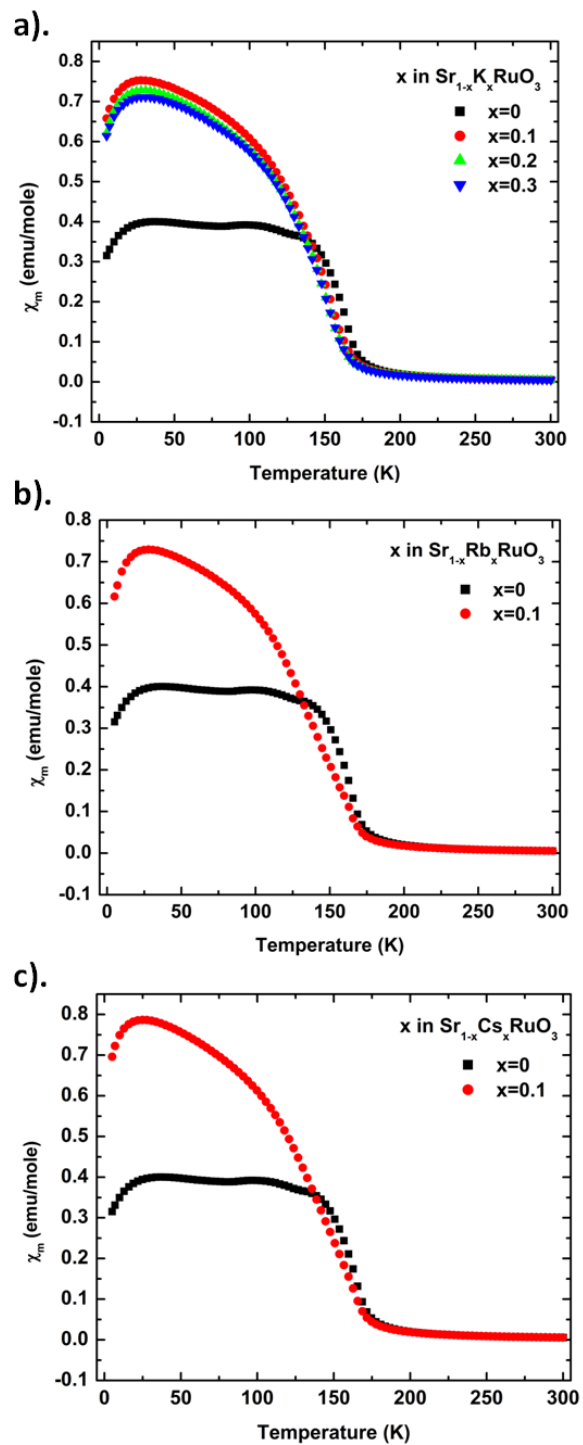


Figure 3.11. The molar magnetic susceptibility (χ_m) for the $\text{Sr}_{1-x}\text{K}_x\text{RuO}_3$ (a), $\text{Sr}_{1-x}\text{Rb}_x\text{RuO}_3$ (b), and $\text{Sr}_{1-x}\text{Cs}_x\text{RuO}_3$ (c) phases.

The number of unpaired electrons that can be contributed to the π^* band is not as relevant to the ferromagnetism as the Ru – O covalency as proved by CaRuO_3 studies [22]. Thus we postulate that the structural effects of M^{1+} substitution are significant enough to lead a weakening of the Ru – O interactions that drive ferromagnetism.

Figure 3.12 depicts the Seebeck coefficient and resistivity data for the $\text{Sr}_{0.9}\text{M}_{0.1}\text{RuO}_3$ compositions. The Seebeck coefficient is found to be in the 30 – 40 $\mu\text{V}/\text{K}$ range for all compositions and to generally decrease with increasing temperature. This positive Seebeck coefficient alludes to the presence of majority hole carriers in the compositions. A more dynamic change in Seebeck was initially expected with the formation of Ru^{5+} ions with an extra hole in the t_{2g} band expected to lead to a higher positive Seebeck coefficient. This increase may be attained in higher alkali metal content phases.

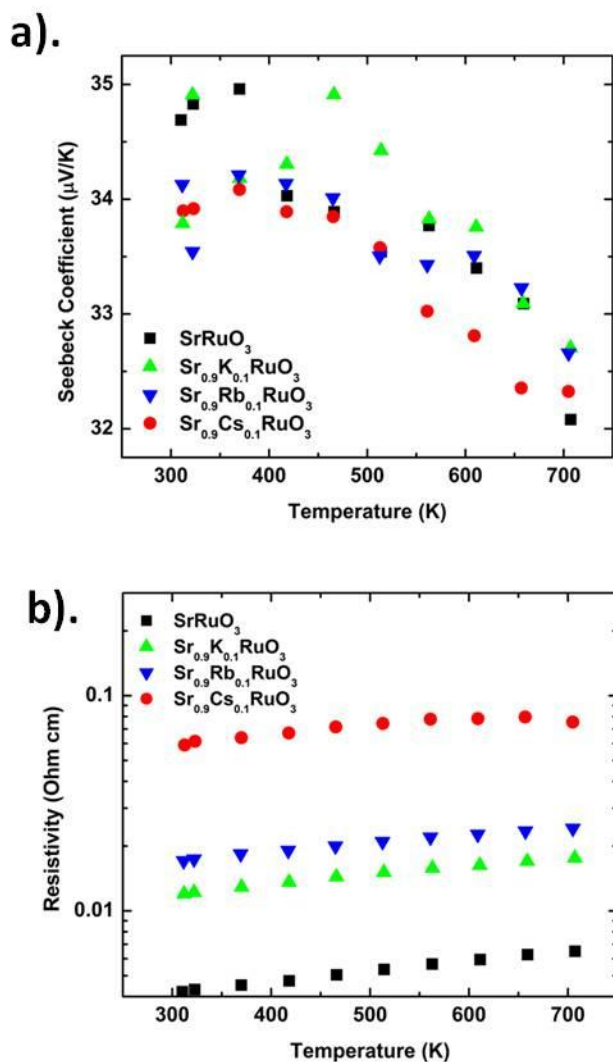


Figure 3.12. Evolution of Seebeck coefficient (a) and electrical resistivity (b) with temperature for the $\text{Sr}_{0.9}\text{M}_{0.1}\text{RuO}_3$ ($\text{M} = \text{K}, \text{Rb}, \text{Cs}$) phases.

In terms of the resistivity, a much clearer trend is observed, with increasing alkali cation size leading to higher resistivity. This likely results from the alkali cation contributing to distortion of the unit cell which impedes the carrier mobility through the $\text{Ru} - \text{O} - \text{Ru}$ pathway. The larger the alkali species, the more the unit cell is distorted and in turn the poorer the carrier mobility.

3.3.3 Conclusion

The $\text{Sr}_{1-x}\text{M}_x\text{RuO}_3$ ($M = \text{K}, \text{Rb}, \text{Cs}$) phases show low substitution levels are possible with $x \leq 0.3$ for $\text{Sr}_{1-x}\text{K}_x\text{RuO}_3$ and $x \leq 0.1$ for $\text{Sr}_{1-x}\text{Rb}_x\text{RuO}_3$ and $\text{Sr}_{1-x}\text{Cs}_x\text{RuO}_3$. The ferromagnetic T_c of SrRuO_3 was found to be decreased by all the substituted phases. The distortions resulting from the substitutions are found to decrease the electrical conductivity. Nonetheless, the Seebeck coefficient is found to be relatively unchanged by the low substitution levels. Higher substitution levels may allow for more significant changes in the Seebeck coefficient.

3.3.4 Experimental

$\text{Sr}_{1-x}\text{M}_x\text{RuO}_3$ ($M = \text{K}, \text{Rb}, \text{Cs}$) phases were prepared by solid state reactions in air from dried carbonates of Sr, K, Rb and Cs (preheated overnight at 120 °C to prevent moisture contamination), and RuO_2 (>99%). The stoichiometric mixtures were ground in an agate mortar with a pestle and the resulting powders initially annealed at 950 °C for 24 hr. The powders were then reground and pressed into pellets that were heated at 950 °C for 24 hr.

Powder X-ray diffraction (PXRD) data were obtained by a Rigaku MiniFlex II diffractometer with $\text{Cu K}\alpha$ radiation and a graphite monochromator. Time of flight Neutron Diffraction data was obtained from the Powder Diffractometer (POWGEN) at Oak Ridge National Laboratory. Le-Bail and Rietveld refinements were done with GSAS software [30,31]. Seebeck coefficient and 4 – probe electrical resistivity measurements were

carried out on an ULVAC - RIKO ZEM-3 under helium atmosphere. Magnetic susceptibility measurements were done on encapsulated powder samples in a magnetic field of 0.5 Tesla from 5 to 300 K (zero-field-cooled) on a Quantum Design Physical Property Measurement System (PPMS) magnetometer.

3.4 Effect of substitution on the thermoelectric properties of $\text{Sr}_2\text{CoRuO}_6$

3.4.1 Introduction

Perovskite materials with the general formula ABO_3 continue to be a great field of interest among solid state chemists. Their highly tunable structure, varying properties and relative stability have made them very desirable for technological applications. A sub-set of the perovskite materials are the “double perovskites” with the general formula $\text{AA}'\text{BB}'\text{O}_6$ and pseudocubic symmetry in which two different species occupy both the A and B site as the dictated by the formula. A great variety of compositions are known to exist in this sub-set, showing an equally diverse range of properties. The properties are dictated by the A and B site species' size, valence, ordering, and the presence of potential interactions between them. The wide array of properties exhibited by double perovskites include ferrimagnetism as shown by $\text{Ca}_2\text{FeReO}_6$ and $\text{Sr}_2\text{FeMoO}_6$ [14,32], weak ferromagnetism in $\text{Sr}_2\text{ErRuO}_6$ [33], antiferromagnetism in $\text{La}_2\text{LiRuO}_6$ and Sr_2YRuO_6 [34,35], and superconductivity in $\text{Sr}_2\text{HoRu}_{1-x}\text{Cu}_x\text{O}_6$ [36–38].

Of particular interest in recent years have been the $\text{AA}'\text{CoRuO}_6$ perovskites [36,39–41]. This interest has been driven by the unique interplay occurring between the B-site species resulting in interesting properties being observed [42,43]. Within these compositions, Co can exist in a High Spin (HS) Co^{2+} or a combination of HS and Intermediate Spin (IS) Co^{3+} states, while Ru tends to remain in the Low Spin (LS) Ru^{5+} and Ru^{4+} states [36,39].

The ionic size and valence deviations of the Co and Ru species can be dictated by the A-site species and this has been well reported [33,40,41].

One key feature affected by the ionic size and valence of the A-site species is the cation ordering between the Co and Ru in the octahedral B-site. SrLaCoRuO_6 has been shown to possess a high ordering percentage (80-90%) on the B-site, with a rocksalt type ordering of Ru^{5+} and Co^{2+} . Within this rocksalt arrangement each $(\text{Co/Ru})\text{O}_6$ octahedron is isolated from all other $(\text{Co/Ru})\text{O}_6$ octahedra as shown in figure 3.13a. The structure is in turn defined by a monoclinic $\text{P}2_1/\text{n}$ space group with an enlarged unit cell of $\sqrt{2}a_p \times \sqrt{2}a_p \times 2a_p$, with a_p describing the lattice parameter of the simple cubic perovskite [39,40]. It should also be noted that the difference in A-site species in SrLaCoRuO_6 leads to a tilting of the $(\text{Co/Ru})\text{O}_6$ octahedra. Conversely, in $\text{Sr}_2\text{CoRuO}_6$ the Co^{3+} and Ru^{5+} have less of a difference in ionic size and valence and thus no ordering in the B-site species occurs and the simple perovskite structure is described by the monoclinic $\text{I}2/\text{c}$ space group [40]. Figure 3.13b depicts the disorder in the B-site and absence of tilted octahedra due to only Sr in the A-site.

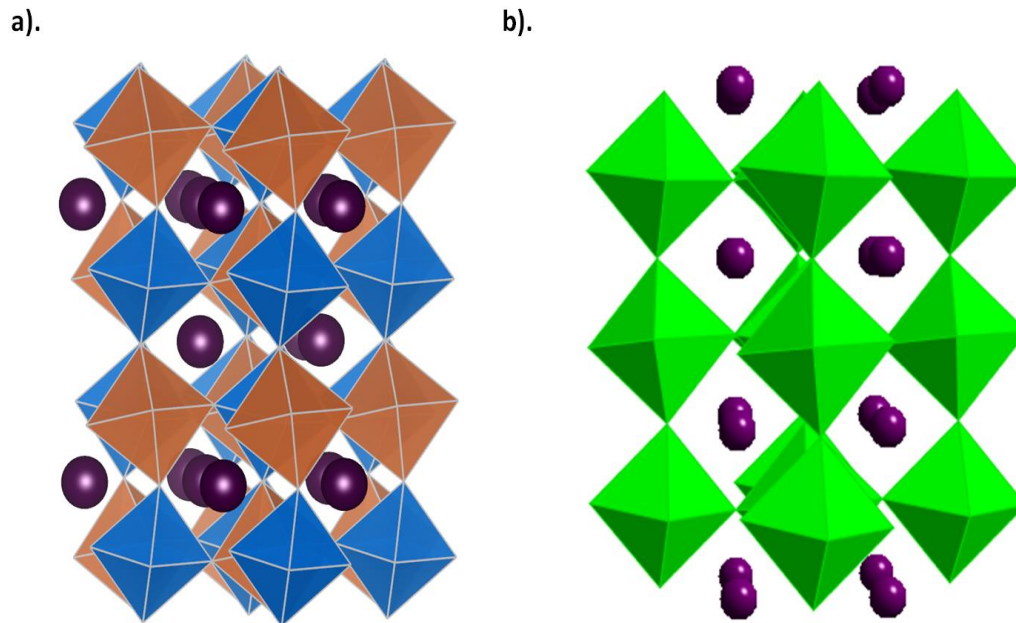


Figure 3.13. Crystal structures of SrLaCoRuO₆ (a) and Sr₂CoRuO₆ (b). In (a) the rocksalt arrangement of the B-site cations in the SrLaCoRuO₆ structure is shown with each CoO₆ octahedron (orange in color) isolated from all other CoO₆ octahedra and each RuO₆ octahedron (blue) isolated from all other RuO₆ octahedra. This structure is defined by a monoclinic P2₁/n space group. Disorder on the B-site in Sr₂CoRuO₆ is depicted in (b) with both Co or Ru octahedra represented by green octahedra. This structure is defined by a monoclinic I2/c space group.

Thermoelectrics are a promising group of materials with the capability to convert waste heat into electricity via the Seebeck effect. Alternatively, and currently more common, thermoelectrics can convert an applied voltage difference to a proportional temperature difference via the Peltier effect. With rising global demand for energy, research in the thermoelectrics field continues to be crucial. Currently, apart from the well reported oxides NaCo₂O₄ and Ca₃Co₄O₉ [44–46] not many promising oxide thermoelectric materials have been reported. Oxide thermoelectric materials could play a key role in high temperature applications due to their durability at elevated

temperatures where the thermoelectric performance of intermetallic compositions tends to be diminished [47].

The interplay between cation ordering and the thermoelectric power in $\text{Sr}_{2-x}\text{La}_x\text{CoRuO}_6$ phases has been shown to be very interesting [40,48]. However, currently no complete investigation evaluating the actual viability of the materials as thermoelectrics involving a thermal conductivity and thermoelectric figure of merit (ZT) analysis has been done. In the following section, results from high temperature thermoelectric measurements of $\text{Sr}_{2-x}\text{La}_x\text{CoRuO}_6$ phases are presented. In addition structural and magnetic data are also discussed.

3.4.2 Results and Discussion

3.4.2.1 Structure

The XRD patterns shown in figure 3.14 show the how the diffraction peaks evolve in the $\text{Sr}_{2-x}\text{La}_x\text{CoRuO}_6$ solid solution. The presence of new peaks at $x = 0.5$, specifically the peak at $19^\circ 2\theta$, likely indicates a change in structure from the monoclinic $I2/c$ to $P2_1/n$ structure. This loss in symmetry results as ordering on the B-site occurs for La rich compositions, while a disordered arrangement of Sr^{2+} and La^{3+} on the A-site is retained in this new space group. Our X-ray data indicates that this transition likely occurs at the $\text{La}_{0.5}$ composition. Other investigations have found this transition to be closer to the $\text{La}_{0.6}$ composition and also the $\text{La}_{0.4}$ composition [40,48].

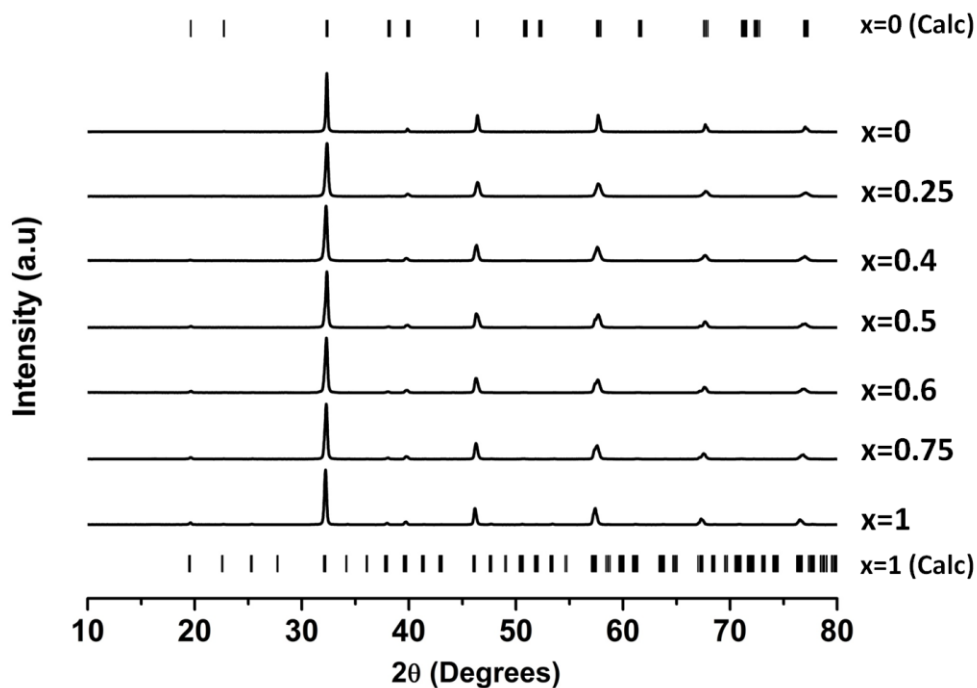


Figure 3.14. The XRD pattern evolution of the $\text{Sr}_{2-x}\text{La}_x\text{CoRuO}_6$ solid solution. The presence of these new peaks at $x = 0.5$ likely indicates a change in structure from the monoclinic $I2/c$ to $P2_1/n$ structure.

Figure 3.15 shows the changes in refined lattice parameters as well as cell volume and c/a ratio with La content. In figure 3.15a, the a parameter is observed to remain fairly constant at 5.53 \AA between $x = 0$ to $x = 0.5$. The a parameter then increases for higher La content to a value of 5.56 \AA for $x = 1$. The b parameter is shown to gradually increase from $x = 0$ to $x = 1$. Figure 3.15b shows the initial decrease in the c parameter to a value of 7.74 \AA for the $x = 0.5$ composition. The c parameter then increases for higher La content. Figure 3.15c shows the cell volume evolution with La content. Initially the cell volume decreases to a value of 237 \AA^3 for the $x = 0.25$ composition and

then increases for higher La content. Figure 3.15d plots the c/a ratio within the solid solution and shows two regions, at $x \leq 0.5$ where the c/a ratio is decreasing and $x > 0.5$ where the c/a ratio is increasing. This trend suggests that initial La substitution may lead to significant distortions of the unit cell.

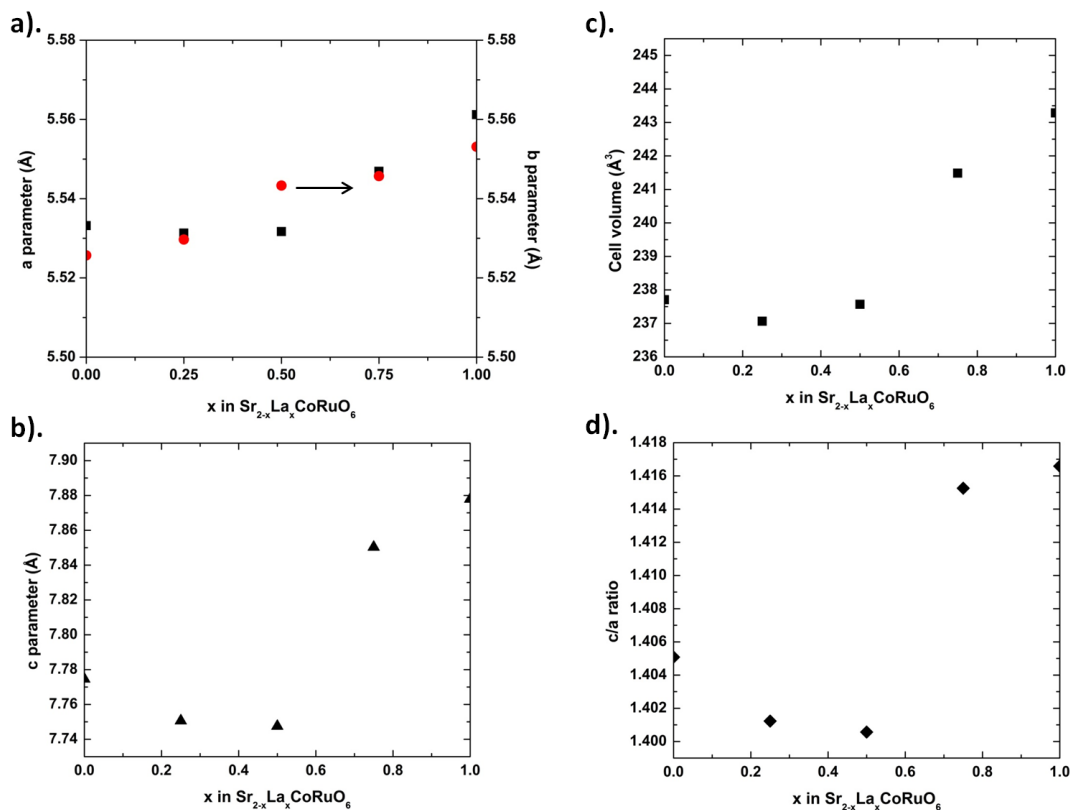


Figure 3.15. Changes in the lattice parameter evolution with La content. The a and b parameter changes are shown in (a), c parameter changes are shown in (b), cell volume changes in (c) and the c/a ratio evolution in (d).

Given the change in structure occurring from $I2/c$ to the enlarged $P2_1/n$, it is expected that the lattice parameters and overall cell volume increase with La content. Thus the observed initial decrease in the c parameter

despite a continued increase in the b parameter is of interest. The ionic radii of Sr^{2+} and La^{3+} with a coordination of eight are 1.26 Å and 1.16 Å respectively [49]. This initial decrease in c parameter may thus evolve from the induced octahedral tilting with La substitution to accommodate the smaller ion. Octahedral tilting has been shown to affect the unit cell dimensions in other structures such as tetragonal Sr_2IrO_4 [50] and Sr_2RhO_4 [51].

3.4.2.2 Physical Properties

Figure 3.16 plots the evolution of the Seebeck coefficient and resistivity with temperature. The $x = 0.85$ and $x = 0.9$ compositions show the highest Seebeck coefficient as seen in figure 3.16a. Figure 3.16b depicts all compositions in the solid solution showing semiconducting behavior with the $x = 1$ composition showing the highest resistivity in the 300 – 700 K range. In comparing the end members, the $x = 0$ composition has the greater absolute Seebeck coefficient than that of the $x = 1$ composition in the temperature range measured. Both samples however possess a majority of electron carriers in the 300 – 700 K temperature range. It is also evident that an increase in Seebeck coefficient occurs with La content up to $x = 0.9$ where the highest Seebeck coefficient is observed in the temperature range measured. The positive Seebeck coefficient for $0.5 \leq x \leq 0.95$ compositions indicates a majority of hole carriers. In attempting to understand this behavior in thermopower, it is important to consider the effects of Metal-Oxygen-Metal (M-O-M) connectivity on the electronic properties. Without any La substitution, there is

no ordering in the octahedral species and thus $\text{Ru}^{5+} - \text{O} - \text{Ru}^{5+}$, $\text{Co}^{3+} - \text{O} - \text{Co}^{3+}$ and $\text{Ru}^{5+} - \text{O} - \text{Co}^{3+}$ connectivity are all possibly present. In this scenario, electron conduction is possible in the $\text{Ru}^{5+} - \text{O} - \text{Ru}^{5+}$ interactions via the π bond with the oxygen. This may help explain the negative Seebeck observed for the $x < 0.5$ compositions. For higher La contents, ordering in the octahedral species is present and thus $\text{Ru}^{5+} - \text{O} - \text{Co}^{2+}$ and $\text{Ru}^{5+} - \text{O} - \text{Co}^{3+}$ interactions are primarily present. This connectivity may be more conducive to hole carrier mobility and may thus explain the higher La contents show the positive Seebeck measured.

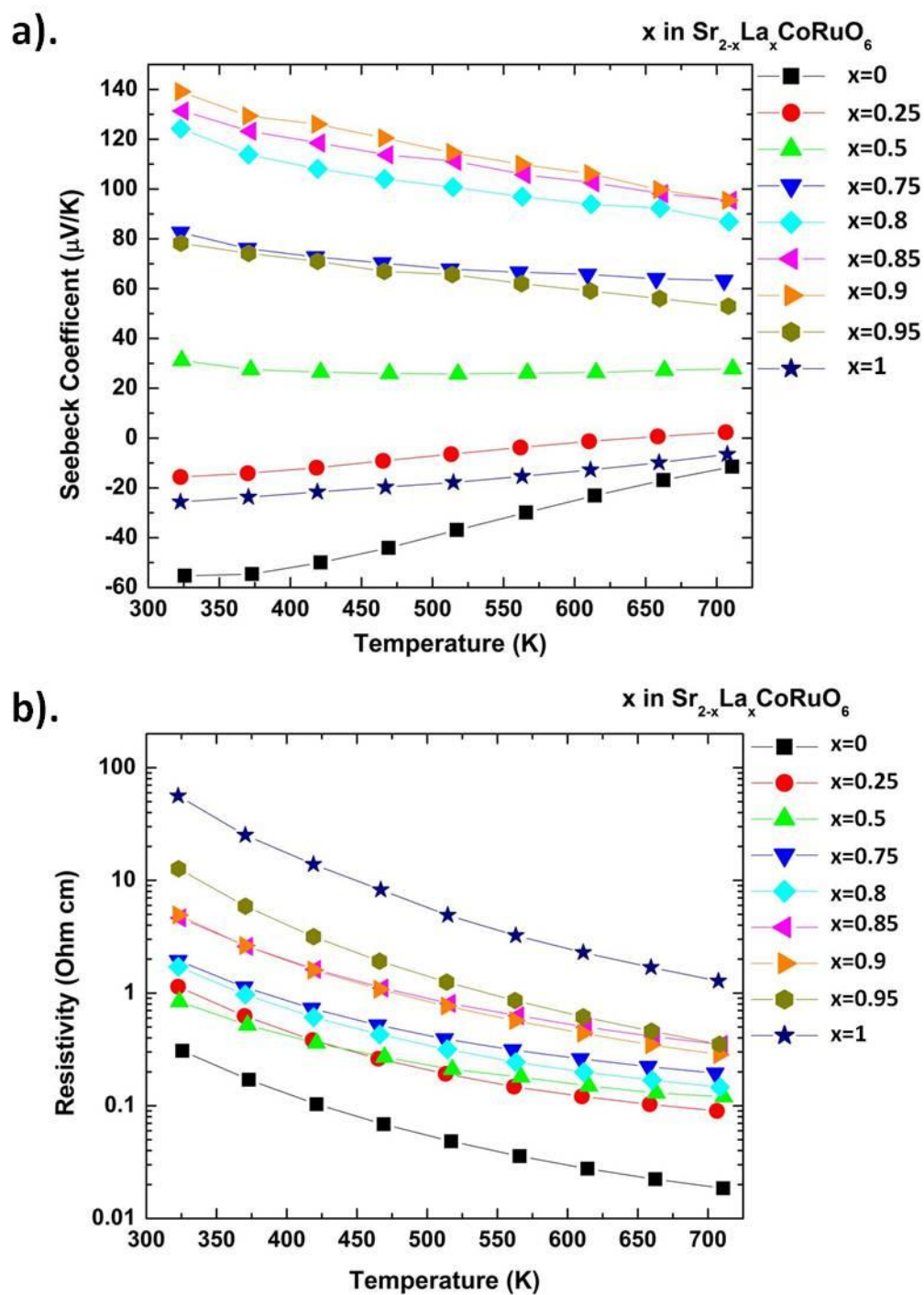


Figure 3.16. The evolution of the Seebeck coefficient (a) and resistivity (b) with temperature.

The evolution of the thermopower in this system has been suggested to be also dependent on the carrier mobility [48]. A higher carrier mobility is usually correlated to a low effective mass and covalent character. A nearest neighbor hopping mechanism for electrons between Co^{3+} and Ru^{5+} ions and a next nearest neighbor hopping mechanism for electrons between Ru^{5+} ions in $\text{Sr}_2\text{CoRuO}_6$ may influence carrier mobility and ultimately lead to the negative thermopower.

M-M interactions in perovskites are generally very weak and often negligible. Nonetheless with the octahedral distortions observed in the $\text{Sr}_{2-x}\text{La}_x\text{CoRuO}_6$ phases, they may be worth consideration. Considering the presence of metal-metal (M-M) interactions and also the electronegativity of La^{3+} may help in understanding the trend in majority carriers observed. Stronger M-M interactions may indicate weaker metal-oxygen (M-O) interactions, and possibly the presence of oxygen deficiencies within the structure. This may then lead to more n-type character. Further studies involving Neutron diffraction to investigate this possibility are in consideration. On the other hand, the La^{3+} cation is more electronegative than the Sr^{2+} cation and thus, with a higher La content there is likely more electron localization and thus a decrease in the electron carriers, ultimately leading to more p-type character.

Hence in the solid solution range $x = 0 - 1$, these two factors may be competing and at $x < 0.5$ compositions, the presences of strong M-M interactions and oxygen deficiencies may take precedent and thus lead to the

n-type character observed. Contrastingly, at higher La concentrations, the stronger electronegativity of La^{3+} in comparison to Sr^{2+} may take precedent and lead to the overall p-type character observed.

The $x = 1$ composition shows the highest resistivity in the temperature range measured and has been described as the ideal single-valent insulator composition as the Co and Ru are distinctly in one oxidation state these being $2+$ and $5+$ respectively [40]. The $x = 0$ composition shows the lowest resistivity as seen in figure 3.16b. This may be the result of the delocalization of one more electron with Co^{3+} in the $x = 0$ composition than with the Co^{2+} in the $x = 1$ composition. This delocalized electron may then be free to move into the conduction band and participate in conduction.

Figure 3.17a and 3.17b depict the thermal conductivity and thermoelectric figure of merit (ZT) with temperature respectively. The $x = 0.9$ composition is shown to have the lowest thermal conductivity in the 300 – 700 K range and shows the highest ZT value in the 475 – 700 K range. These findings indicate that among the compositions investigated, $\text{Sr}_{1.1}\text{La}_{0.9}\text{CoRuO}_6$ shows the best thermoelectric performance at high temperature. Wiedemann-Franz calculations currently suggest that the lattice thermal conductivity is on average 99 % of the total thermal conductivity measured. This means that further processing to decrease the lattice thermal conductivity via methods such as nanostructuring to scatter phonons may lead to improvements in the overall thermoelectric performance of the compositions studied.

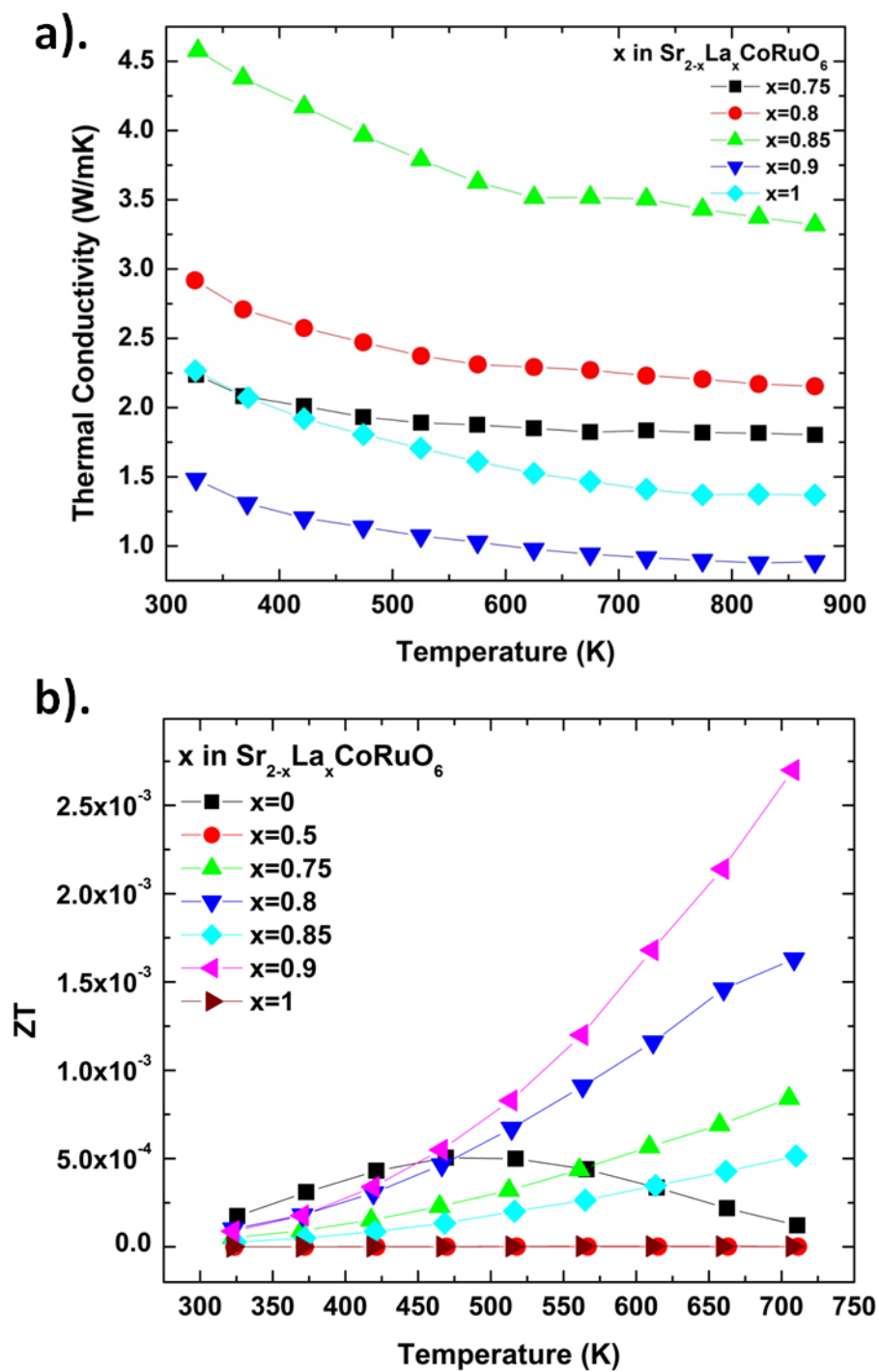


Figure 3.17. The evolution of thermal conductivity (a) and thermoelectric figure of merit (ZT) (b) with temperature.

Figure 3.18 shows the magnetism data for the $\text{Sr}_{2-x}\text{La}_x\text{CoRuO}_6$ solid solution. Figure 3.18a depicts the molar magnetic susceptibility with temperature while figure 3.18b shows the evolution of inverse molar magnetic susceptibility with temperature. Figure 3.18c-e tracks fitted Curie – Weiss data with (c) showing Curie constant, (d) showing the Weiss constant, and (e) showing the calculated spin-only magnetic moment with La content. It is evident that the $x = 0.25$ compound shows the highest molar susceptibility while the $x = 0$ composition has the lowest below 150 K. The large ferromagnetic signal of the $x = 0.25$ sample was initially assumed to result from a possible SrRuO_3 impurity, however this impurity phase was not evident in the XRD data. Neutron or Synchrotron studies may be required to investigate this further. In addition, it is possible that ferromagnetic Ru - Ru interactions may be responsible for the ferromagnetic features observed for $x \leq 0.5$ compositions with itinerant-electron π^* band formation occurring [48].

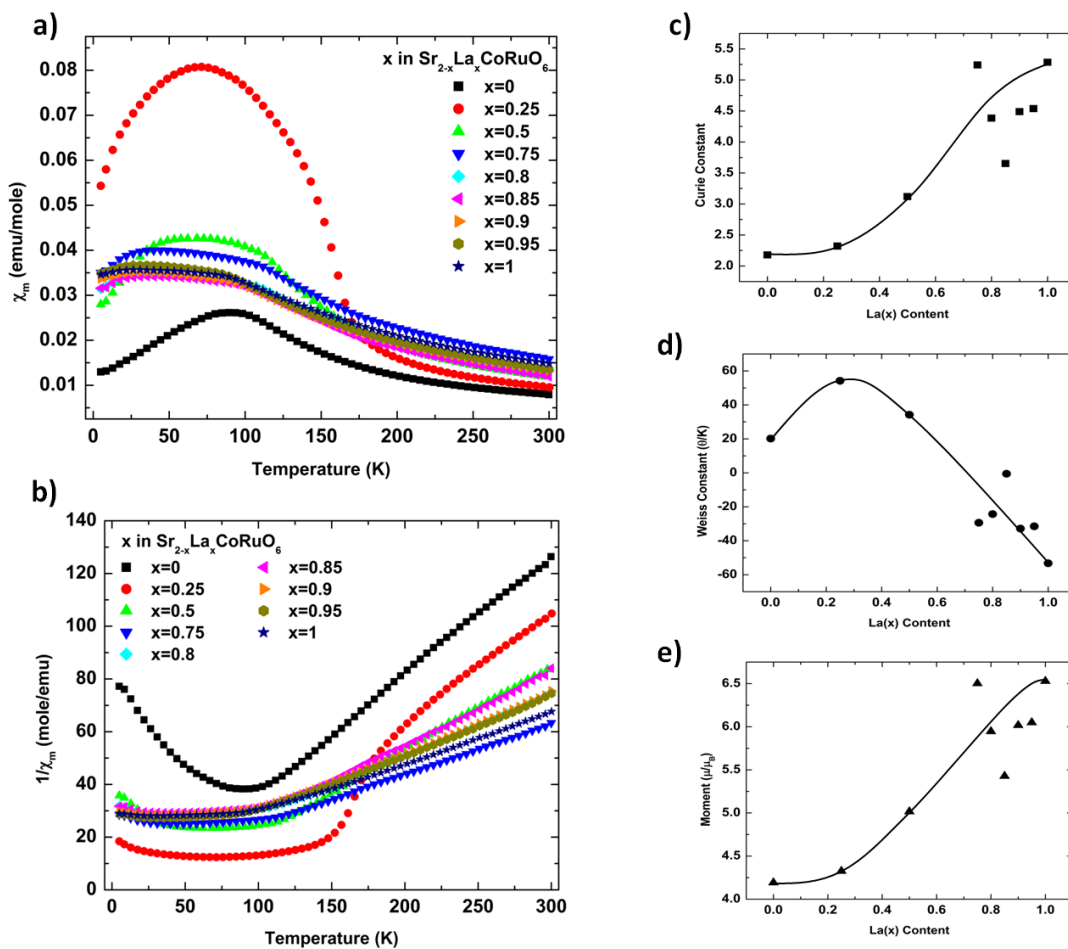


Figure 3.18. The magnetism data for the $\text{Sr}_{2-x}\text{La}_x\text{CoRuO}_6$ solid solution. The molar magnetic susceptibility with temperature is shown in (a) and inverse molar magnetic susceptibility with temperature is shown in (b). Plot (c) shows the Curie constant, (d) shows the Weiss constant, and (e) shows the magnetic moment with La content.

The Weiss constant values in (d) indicate that compositions with $x \leq 0.5$ primarily possess ferromagnetic interactions while those with $x > 0.5$ primarily possess antiferromagnetic interactions. It is necessary to consider why the $x = 0.25$ composition shows such a high susceptibility and significantly higher Curie temperature as compared to the other composition. It seems that a small La substitution is leading to a stronger correlation

between unpaired electrons at low temperature. This may be correlated to structural changes occurring with the La substitution such as the octahedral tilting which may enhance the interaction between the unpaired electrons. It has also been suggested that phases in the $x = 0 - 1$ range do possess Co ions in both HS and IS states and Ru ions in the LS state. The scenario is complicated further with the possible presence of spin-orbit coupling [40,52,53]. This is worthy of further investigation beyond the scope of this investigation.

3.4.3 Conclusion

$\text{Sr}_{2-x}\text{La}_x\text{CoRuO}_6$ ($0 \leq x \leq 1$) phases possess the perovskite structure and are defined by monoclinic space groups $I2/c$ for $x < 0.5$ and $P2_1/n$ for higher La contents. The first complete thermoelectric analysis of the phases involving k_T determination via diffusivity measurements was performed. Thermoelectric studies show that the complexity in B-site size and valency affects carrier type and mobility. Currently, $\text{Sr}_{1.1}\text{La}_{0.9}\text{CoRuO}_6$ shows the best high temperature thermoelectric performance. Further improvements via careful sample processing and also further structural studies are likely to help improving the thermoelectric performance of these phases.

3.4.4 Experimental

Polycrystalline samples were prepared by conventional solid-state synthesis. Reactants were SrCO_3 (Alfa 99.9%) dried at 120°C overnight to

avoid moisture contamination, La_2O_3 (Alfa 99.99%) preheated at 875 °C for 12 hr to decrease moisture contamination, Co_3O_4 (Alfa 99.7%), and RuO_2 (> 99%). Stoichiometric amounts of the oxides were ground in an agate mortar and pestle and then pelletized and placed in an alumina boat to be heated to a maximum temperature of 1200 °C for up to 48 hr.

X-ray powder diffraction data were collected with a Rigaku MiniFlex II using $\text{Cu K}\alpha$ radiation and a graphite monochromator. Le-Bail refinements were done with GSAS software [30,31]. Thermoelectric properties; Seebeck coefficient, electrical resistivity, and thermal conductivity were measured at 300 K up to 900 K. The Seebeck coefficient and electrical resistivity were collected on an ULVAC - RIKO ZEM-3 under helium atmosphere. Thermal diffusivity (α) was measured on a Netzsch LFA 457 Micro Flash under flowing Nitrogen. Specific heat (C_p) was measured on a Mettler Toledo 821e Differential Scanning Calorimeter with an alumina calibration standard under flowing Nitrogen. Thermal conductivity (k_T) was determined by the relation $k_T = C_p \alpha d$, where d is the sample bulk density.

Magnetic susceptibility measurements were done on encapsulated powder samples in a magnetic field of 0.5 Tesla from 5 to 300 K (zero-field-cooled) with a Quantum Design Physical Property Measurement System (PPMS) magnetometer.

3.5 Investigating the thermoelectric properties of $(\text{RhV})_{1+x}\text{Ti}_{1-2x}\text{O}_6$ phases with the Rutile-type structure.

3.5.1 Introduction

Rutile-type structures have been under investigation by solid state chemists for almost a century now and new derivatives of this structure continue to be discovered showing promise for current and future technological applications [54–57]. These include in pigments, electrochemistry, and catalysis [57].

One group of compounds that are derived from the rutile-type structure are the $\text{AA}'\text{MO}_6$ compounds where three different species are present in half the octahedral sites in the hexagonally close packed oxygen framework. Within this structure, the octahedra share corners in the ab plane while edge sharing occurs along the c – axis (Figure 3.19).

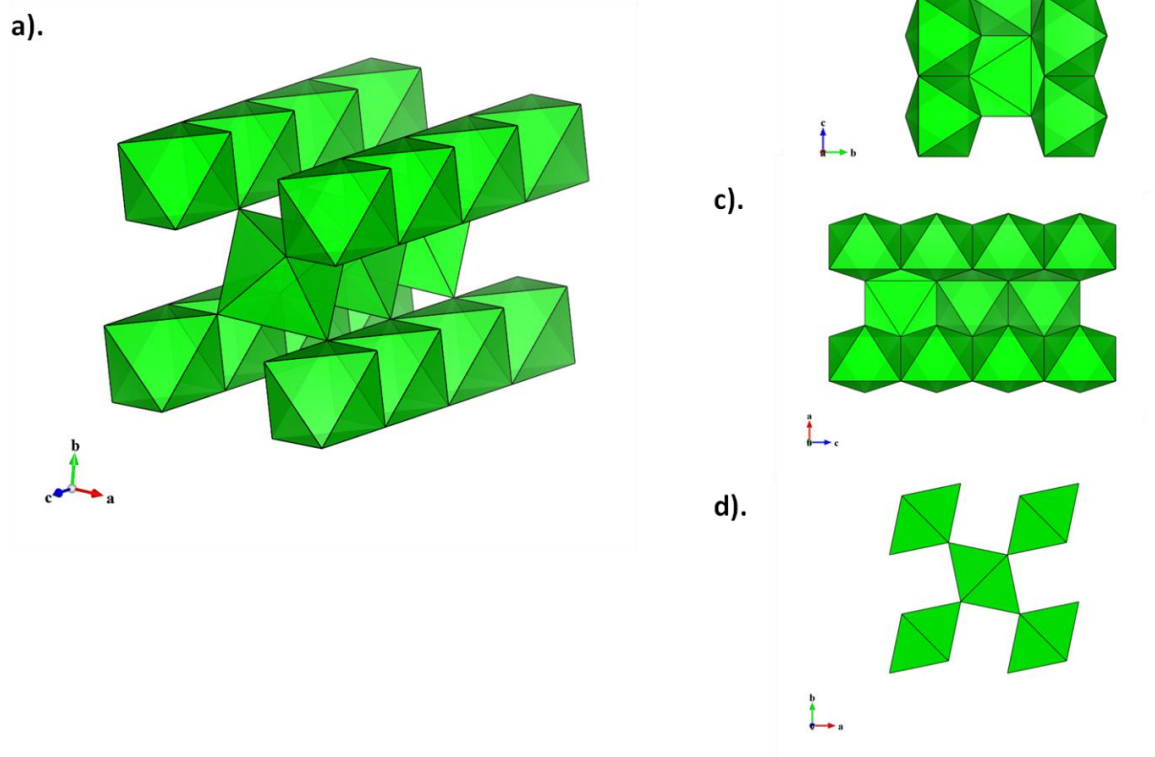


Figure 3.19. Depiction of the tetragonal P42/mmm (136) rutile structure. In (a) the corner sharing in the *ab* plane and edge sharing along the *c*-axis is shown. The structure is displayed along the *a*, *b*, and *c* direction in (b), (c) and (d) respectively.

Of particular interest within this family of compounds has been the Rh_2MO_6 compounds with $M = \text{Mo}, \text{W}$ and Te , where a number of investigations have attempted to correctly describe the rutile-type structure [58–61]. These investigations have shown that Rh_2MO_6 compounds can either possess an ordered trirutile structure where ordering occurs between the Rh and M species or a disordered rutile structure where the Rh and M species have a disordered arrangement on the octahedral sites. The ordering in the

trirutile structure leads to a tripling of the c unit cell parameter while the a unit cell parameter remains similar to that of the disordered rutile structure [62].

Siritanon et al have recently shown that the properties of these Rh_2MO_6 compounds are reliant on the both the Rh connectivity through Rh – O – Rh bonding and the M cation's oxidizing power [62]. Within the structure of the Rh_2MO_6 compounds, there is three-dimensional Rh connectivity through the Rh – O – Rh bonding that is unaffected by the presence and degree of ordering. The stronger the oxidizing power of the M cation, the more Rh^{3+} to Rh^{4+} conversion occurs. Rh^{3+} has a full 4d t_{2g} band while Rh^{4+} has one hole in its 4d t_{2g} band. Thus with the Rh – O – Rh connectivity presence, hole conduction (p - type conductivity) can occur and as one would expect, the stronger the oxidizing power of the M cation, the more hole conduction present. It should also be noted that some electron conduction is present as a result of the M cation being reduced, however due to the weaker connectivity of the M species, the n - type contribution to overall conductivity is lower. This connection between the M cation oxidizing power and the conductivity has been observed in Rh_2MO_6 (M = Mo, W and Te) investigations where Rh_2TeO_6 shows the highest conductivity as a result of Te^{6+} having the greatest oxidizing power, while Rh_2WO_6 shows the lowest conductivity resulting from W^{6+} having the lowest oxidizing power of the three [62].

$\text{MM}'\text{O}_4$ oxides are also derivatives of the rutile-type structure with two species in half the octahedral sites of the hexagonal close packed oxygen

framework. Within these compounds the M and M' cations tend to be either disordered as seen in RhVO₄ [63] or take up different coordinations as seen in CrVO₄ [63,64] where the Cr is in octahedral coordination while V is in VO₄ tetrahedra. This difference in coordination in some MM'O₄ structures has also been observed in LnVO₄ (Ln = La - Lu) where the lanthanide species can be in an eight or nine coordination [63,65,66]. The presence of disorder on the crystallographic 2a site of the MM'O₄ rutile-type structures or the difference in coordination has been related to the mean radius ratio between the M and M' species where a large mean radius ratio leads to a disorder of M and M' octahedra on the 2a site of the rutile-type structure but a mean ratio of ≤ 0.35 leads to distortions that allow for differences in coordination to occur [63].

Thermoelectric materials provide a unique avenue for power generation where waste heat can be converted to electrical power via the Seebeck effect or alternatively an applied voltage difference can be converted to a temperature gradient via the Peltier effect. In general, oxide materials tend to be poor thermoelectrics due to high effective masses and lower carrier mobilities. Some of the best performing thermoelectric oxides are Na₂Co₂O₄ and Ca₃Co₄O₉ that both possess Co in a mixed valency state of Co³⁺/Co⁴⁺ [44–46]. This mixed valency nature of Co is analogous and isoelectronic to that exhibited in the in the Rh₂MO₆ (M = Mo, W, Te) compounds where Rh is in a mixed valency state of Rh³⁺/Rh⁴⁺. Thermoelectric investigations of these compounds showed lower Seebeck coefficients and power factors than those of NaCo₂O₄ and Ca₃Co₄O₉ but proved that in both the Mo and W case, two

types of carriers were present while only one type of carrier was present in Rh_2TeO_6 [62].

Other investigations have suggested that a large entropy of low-spin-state Co^{4+} in the background of low-spin Co^{3+} may lead to the high thermoelectric power and electrical conductivity in the Co oxides [67]. Nonetheless, it still is worthwhile to investigate the effects on thermoelectric power and electrical conductivity when no valence degeneracy in the $\text{AA}'\text{MO}_6$ compounds is present. Investigations of $(\text{RhV})_{1+x}\text{Ti}_{1-2x}\text{O}_6$ phases, which have currently not been reported in literature, are discussed in the next section. Structural data and electronic properties, including thermoelectric performance are reviewed.

3.5.2 Results and Discussion

The XRD patterns shown in figure 3.20 depict the successful formation of the solid solution ($x = 0 - 0.45$) compositions. Close observation of the patterns shows no presence of superstructure peaks that would be expected if any ordering of the $(\text{Rh/V})\text{O}_6$ and TiO_6 octahedra occurs. For example, we examined the $45^\circ 2\theta$ region, where a superstructure peak would be expected if some level of ordering was present, however no hint of a peak was observed. Thus all the $(\text{RhV})_{1+x}\text{V}_{1-2x}\text{O}_6$ phases are thought to possess the disordered rutile-type structure with corner sharing octahedra in the ab plane and edge sharing along the c – direction.

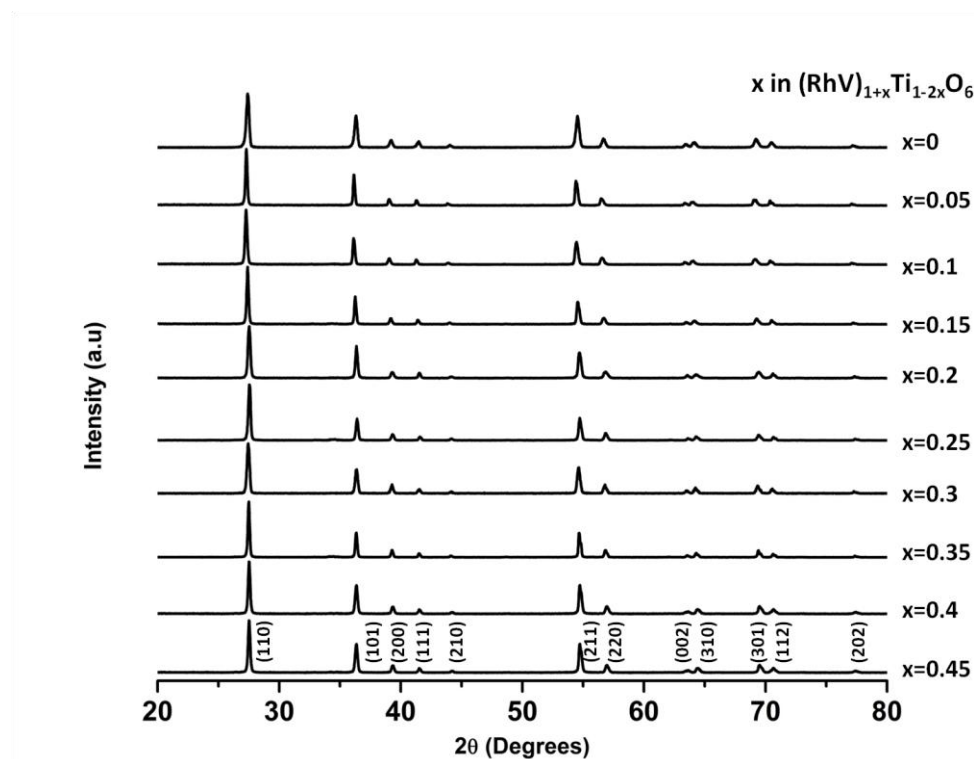


Figure 3.20. XRD patterns of the $(\text{RhV})_{1+x}\text{V}_{1-2x}\text{O}_6$ solid solution with the (hkl) values to show the formation of the tetragonal rutile structure.

Given that Rh_2WO_6 is found to be partially ordered with Rh^{3+} (0.665 Å) and W^{6+} (0.6 Å) species, it was expected that some ordering may be possible in the $(\text{RhV})_{1+x}\text{Ti}_{1-2x}\text{O}_6$ phases. Despite possessing dissimilar valence and ionic size differences: Rh^{3+} (0.665 Å) / V^{5+} (0.54 Å) and Ti^{4+} (0.605 Å), the lack of valence degeneracy in the $(\text{RhV})_{1+x}\text{Ti}_{1-2x}\text{O}_6$ phases was expected to allow for ordering to occur [49,62]. It is important to consider the scattering powers of the species present when considering the observation (or lack thereof) superstructure peaks. A significant difference in species' scattering powers may lead to a masking of superstructure peaks. Thus, the fact that the scattering powers of V and Ti are relatively weak as compared to that of Rh, may be leading to the superstructure peaks being currently undetectable.

Figure 3.21 depicts the changes in lattice parameters, cell volume and c/a ratio with Ti content. Both the a and c parameters decrease with increasing x (decreasing Ti content) up to an $x = 0.25$ representing the $(\text{RhV})_{1.25}\text{Ti}_{0.5}\text{O}_6$ composition. This composition is shown to possess the smallest unit cell with a and c parameters at their lowest within the solid solution at values of 4.58 \AA and 2.92 \AA respectively. This is correlated to the lowest cell volume of 61.3 \AA^3 as shown in figure 3.21b. With further decrease in Ti content the the a parameter shows a slight increase and then levels off while the c parameter also shows a gradual increase. These trends are depicted in the cell volume as a slight increase is observed after the $x = 0.25$ composition. The c/a ratio shown in figure 3.21c depicts an increasing c/a ratio with decreasing Ti content, however its clear after the $x = 0.25$ composition the slope of increase does change. This trend in lattice parameters alludes to the fact that with Ti substitution the rutile-type structure of the $(\text{RhV})_{1+x}\text{V}_{1-2x}\text{O}_6$ phases is retained. The $(\text{RhV})_{1.25}\text{V}_{0.5}\text{O}_6$ composition likely possesses the most distorted octahedra with most of the distortion happening along the ab plane where corner sharing occurs.

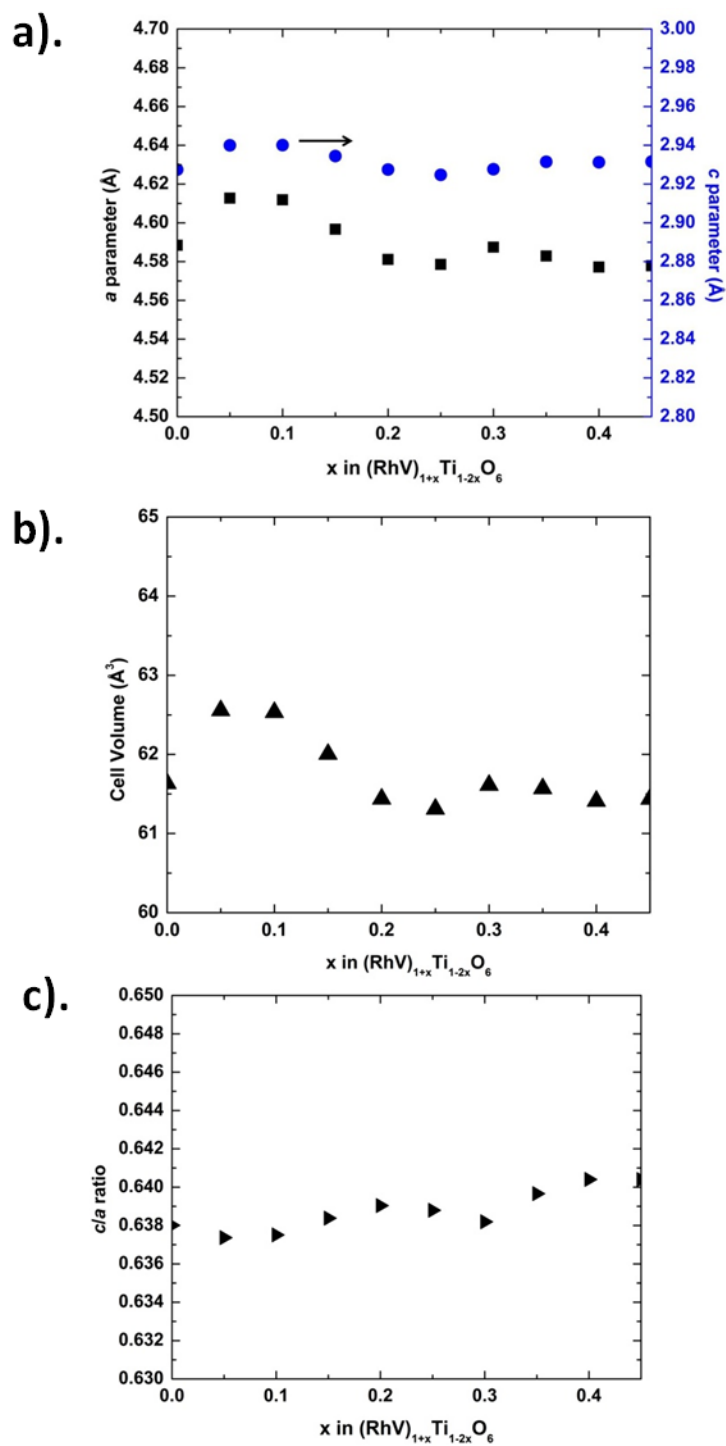


Figure 3.21. Refined values of the a (black squares) and c (blue circles) cell parameters of the tetragonal unit cell (a), cell volume (b) and c/a ratio (c).

In figure 3.22 the conductivity, Seebeck coefficient, and thermal conductivity of the compositions in the 300 – 900 K range are plotted. In (a) we see that all compositions show semiconducting behavior in the temperature range measured. It is also observed that the lower Ti content compositions ($x \geq 0.35$) show the higher conductivity. In (b) we see that essentially all the compositions show a negative Seebeck coefficient in the temperature range measured. Only the $x = 0.45$ at ~ 300 K has a slightly positive Seebeck coefficient which quickly becomes negative with increasing temperature. This indicates that the compositions possess a majority of n-type carriers. The 400 – 500 K region appears to be where the absolute Seebeck is highest in most of the compositions with the $x = 0$ sample (containing the highest Ti content) showing the highest absolute Seebeck coefficient of over $200 \mu\text{V/K}$ at approximately 420 K. In figure 3.22c we see that the $x = 0$ composition possesses the highest thermal conductivity while the $x = 0.05$ composition possesses the lowest thermal conductivity in the 300 – 900 K temperature range measured. The $x = 0.35$ with the relatively high electrical conductivity has a relatively median thermal conductivity ranging from about $1.5 - 4 \text{ W/mK}$ in the temperature range measured.

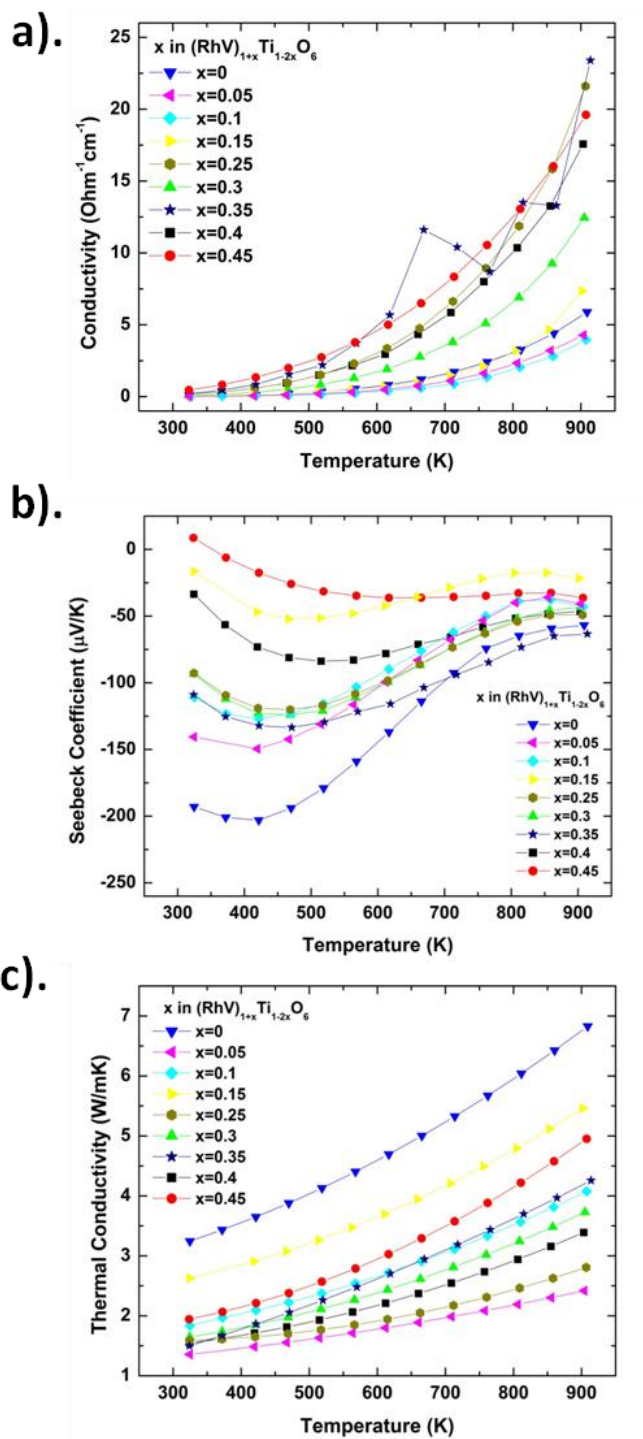


Figure 3.22. Electrical conductivity (a), Seebeck Coefficient (b) and Thermal conductivity (c) evolution with temperature from 300 – 900 K of $(\text{RhV})_{1+x}\text{V}_{1-2x}\text{O}_6$ phases.

In figure 3.23 the calculated dimensionless figure of merit (ZT) for the compositions within the temperature range measured is shown. It is clear that the $(\text{RhV})_{1.35}\text{Ti}_{0.3}\text{O}_6$ composition shows the best thermoelectric performance specifically in the 600 – 700 K range.

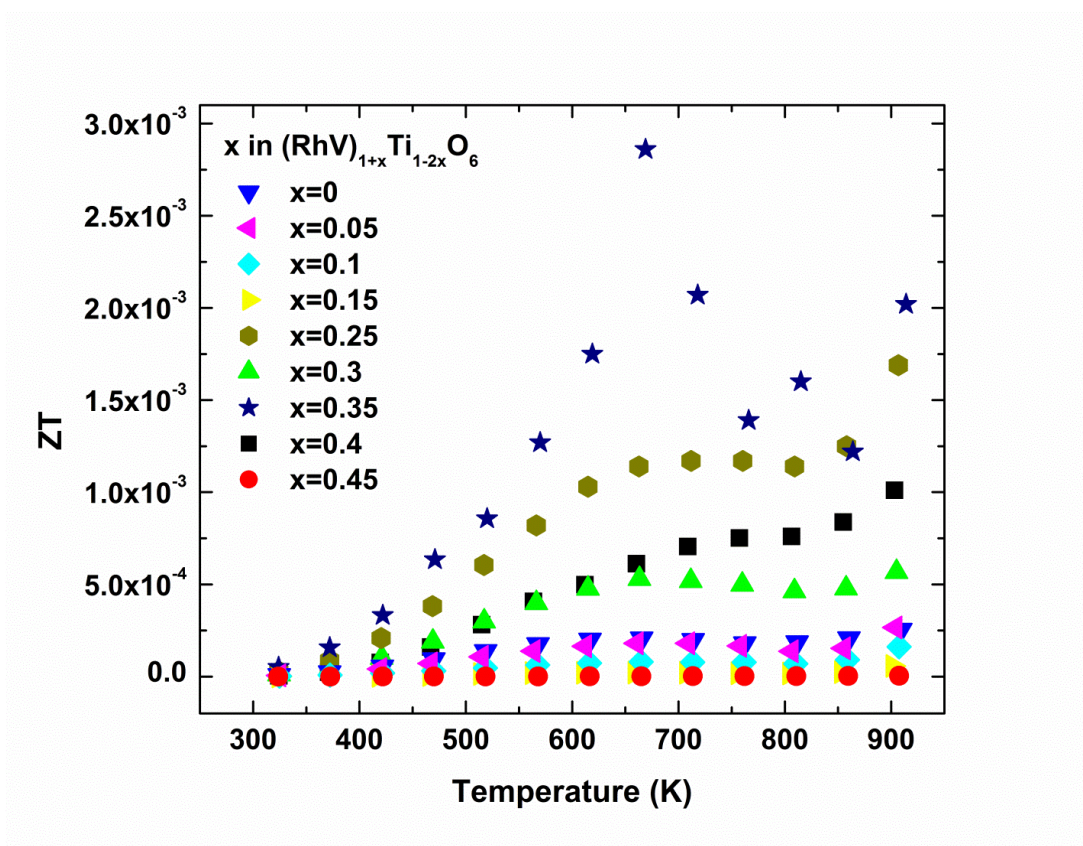


Figure 3.23. Figure of merit (ZT) of the $(\text{RhV})_{1+x}\text{V}_{1-2x}\text{O}_6$ samples in the 300 – 900 K temperature range.

In attempting to understand these electrical properties, it is worthwhile to consider the electrical properties of the Rh_2MO_6 ($\text{M} = \text{Mo}, \text{W}, \text{Te}$) series. As previously mentioned, the oxidizing power of the M cation is key to hole conductivity observed in these compounds. The p-type nature results from the oxidation of Rh^{3+} to Rh^{4+} by the M cation. With the $(\text{RhV})_{1+x}\text{Ti}_{1-2x}\text{O}_6$ compositions the majority carriers are electrons. Oxidation of Rh^{3+} by V^{5+} would result in p-type conduction not the n-type conduction observed. Thus, it is possible that the Rh 4d orbitals overlapping with the 3d orbitals of V and/or Ti leads to the conductivity observed. This is plausible given that in the rutile-type structure, the presence of corner shared octahedra in the ab plane and edge shared octahedra along the c – axis results in inter-atomic distances that lead to both the M – M and M – O – M interactions influencing the physical properties. The presence of the 4d – 3d overlap may allow for some electron delocalization that in turn results in the n-type conductivity shown. Given that we observe a general decrease in conductivity with increasing Ti content, it is likely that the overlap between the Rh 4d and V 3d orbitals is primarily responsible for conduction observed and is inhibited with Ti substitution. In order to give further insight on this, activation energies of the compositions are plotted in figure 3.24. It can be seen that the activation energy does increase with Ti content suggesting that it is actually the Rh 4d – V 3d orbital overlap that is primarily responsible for the conduction observed.

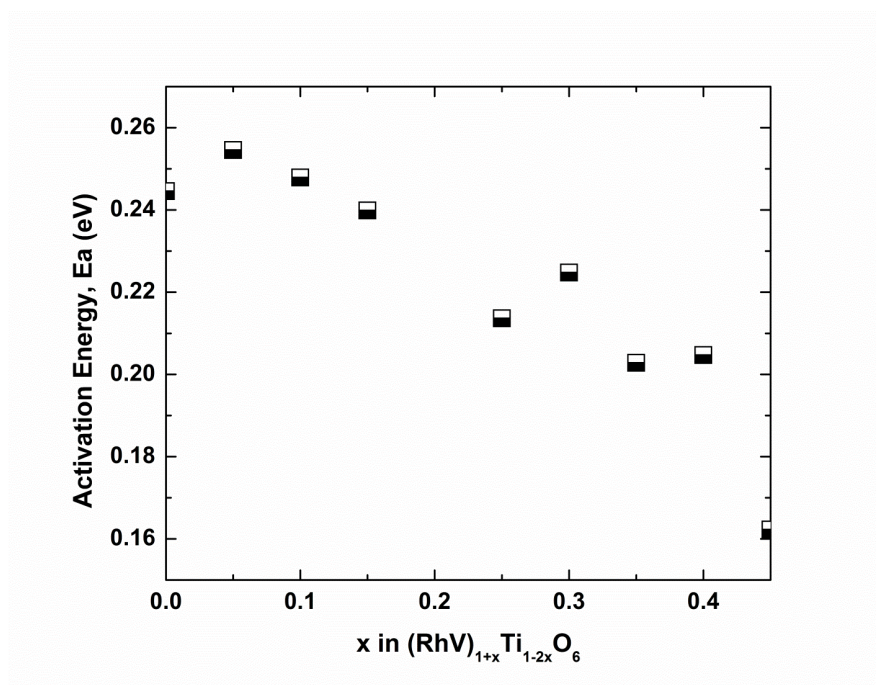


Figure 3.24. The activation energy in eV of the $(\text{RhV})_{1+x}\text{V}_{1-2x}\text{O}_6$ compositions.

In terms of the carriers, figure 3.22b leads us to believe that the carrier concentration is changing with temperature as evidenced by the changing slopes of the curves. Above 600 K the electron carriers begin to be depleted rather dramatically for all compositions.

Preliminary investigations of the thermal conductivity using the Wiedemann-Franz relationship show that the lattice thermal conductivity makes up > 99 % of the total thermal conductivity. This suggests that further processing of these compositions via methods such as nanostructuring could go a long way in improving the overall thermoelectric performance of the materials.

3.5.3 Conclusion

(RhV)_{1+x}Ti_{1-2x}O₆ compounds are found to crystallize in the disordered rutile-type structure with no ordering of octahedral species. This results despite little or no valence degeneracy occurring. Electronic data indicates a majority of electron carriers likely resulting from Rh 4d – V 3d orbital overlap. Thermal conductivity and ZT analysis show possibility of improved thermoelectric performance via processing techniques.

3.5.4 Experimental

(RhV)_{1+x}Ti_{1-2x}O₆ phases were prepared by solid state reactions in air from Rh₂O₃ (prepared from heating RhI₃ in air), V₂O₅ (Aldrich, 99.99%) and TiO₂ (JMC, 99.99%). The stoichiometric mixtures were ground in an agate mortar with a pestle and the resulting powders were pressed into pellets and heated at 800 – 850 °C for 12 – 24 hours with intermediate grindings.

Powder X-ray diffraction (PXRD) data were obtained by a Rigaku MiniFlex II diffractometer with Cu K α radiation and a graphite monochromator. Seebeck coefficient and 4 – probe electrical resistivity measurements were carried out on an ULVAC - RIKO ZEM-3 under helium atmosphere (with an error limit of 5%). Thermal diffusivity (α) was measured on a Netzsch LFA 457 Micro Flash under flowing Nitrogen (with an error limit of 10%). Specific heat (C_p) was measured on a Mettler Toledo 821e Differential Scanning Calorimeter with an alumina calibration standard under

flowing Nitrogen. Thermal conductivity (k_T) was determined by the relation $k_T = C_p \alpha d$, where d is the sample bulk density.

3.6 References

- [1] R.M. Hazen, *Sci. Am.* 258 (1988) 74–80.
- [2] Aristotype - Online Dictionary of Crystallography. Accessed April 2012.
- [3] A.M. Glazer, *Acta Crystallogr., Sect. B: Struct. Sci.* 28 (1972) 3384–3392.
- [4] P.M. Woodward, *Acta Crystallogr., Sect. B: Struct. Sci.* 53 (1997) 32–43.
- [5] P.M. Woodward, *Acta Crystallogr., Sect. B: Struct. Sci.* 53 (1997) 44–66.
- [6] C.J. Howard, H.T. Stokes, *Acta Crystallogr., Sect. B: Struct. Sci.* 54 (1998) 782–789.
- [7] M.W. Lufaso, P.M. Woodward, *Acta Crystallogr., Sect. B: Struct. Sci.* 57 (2001) 725–738.
- [8] H.W. Eng, P.W. Barnes, B.M. Auer, P.M. Woodward, *J. Solid State Chem.* 175 (2003) 94–109.
- [9] B.H. Kim, B.I. Min, *Phys. Rev. B* 80 (2009) 064416.
- [10] G. King, P.M. Woodward, *J. Mater. Chem.* 20 (2010) 5785.
- [11] R.H. Mitchell, *Perovskites: Modern and Ancient*, Almaz, 2003.
- [12] M.W. Lufaso, P.W. Barnes, P.M. Woodward, *Acta Crystallogr., Sect. B: Struct. Sci.* 62 (2006) 397–410.
- [13] C.J. Howard, B.J. Kennedy, P.M. Woodward, *Acta Crystallogr., Sect. B: Struct. Sci.* 59 (2003) 463–471.
- [14] M. Anderson, K. Greenwood, G. Taylor, K. Poepelmeier, *Prog. Solid State Chem.* 22 (1993) 197–233.
- [15] V. Caignaert, F. Millange, M. Hervieu, E. Suard, B. Raveau, *Solid State Commun.* 99 (1996) 173–177.
- [16] P.M. Woodward, T. Vogt, D.E. Cox, A. Arulraj, C.N.R. Rao, P. Karen, A.K. Cheetham, *Chem. Mater.* 10 (1998) 3652–3665.
- [17] P.G. Radaelli, D.E. Cox, M. Marezio, S.-W. Cheong, *Phys. Rev. B* 55 (1997) 3015–3023.
- [18] L. Pauling, *J. Am. Chem. Soc.* 51 (1929) 1010.
- [19] H. Kobayashi, M. Nagata, R. Kanno, Y. Kawamoto, *Mater. Res. Bull.* 29 (1994) 1271–1280.
- [20] T. Sugiyama, N. Tsuda, *J. Phys. Soc. Jpn.* 68 (1999) 3980–3987.
- [21] I. Felner, U. Asaf, *Physica B: Condens. Matter* 337 (2003) 310–317.
- [22] J.M. Longo, P.M. Raccah, J.B. Goodenough, *J. Appl. Phys.* 39 (1968) 1327–1328.
- [23] R.J. Bouchard, J.L. Gillson, *Mater. Res. Bull.* 7 (1972) 873–878.
- [24] R.J. Bouchard, J.F. Weiher, *J. Solid State Chem.* 4 (1972) 80–86.
- [25] R.J. Bouchard, J.F. Weiher, J.L. Gillson, *J. Solid State Chem.* 6 (1973) 519–525.
- [26] A. Kanbayasi, *J. Phys. Soc. Jpn.* 44 (1978) 108–113.
- [27] R. Greatrex, G. Hu, D.C. Munro, *Mater. Res. Bull.* 21 (1986) 797–802.
- [28] S. Shuba, A. Mamchik, I.-W. Chen, *J. Phys.: Condens. Matter* 18 (2006) 9215–9220.
- [29] I.I. Mazin, D.J. Singh, *Phys. Rev. B* 56 (1997) 2556–2571.
- [30] A.C. Larson, R.B. Von Dreele, Los Alamos National Laboratory Report LAUR (2004) 86–748.

- [31] B.H. Toby, *J. Appl. Cryst.* 34 (2001) 210–213.
- [32] W. Westerburg, O. Lang, C. Ritter, C. Felser, W. Tremel, G. Jakob, *Solid State Commun.* 122 (2002) 201–206.
- [33] P.D. Battle, C.W. Jones, F. Studer, *J. Solid State Chem.* 90 (1991) 302–312.
- [34] P.D. Battle, C.P. Grey, M. Hervieu, C. Martin, C.A. Moore, Y. Paik, *J. Solid State Chem.* 175 (2003) 20–26.
- [35] P.D. Battle, W.J. Macklin, *J. Solid State Chem.* 52 (1984) 138–145.
- [36] S.H. Kim, P.D. Battle, *J. Solid State Chem.* 114 (1995) 174–183.
- [37] P.D. Battle, T.C. Gibb, C.W. Jones, F. Studer, *J. Solid State Chem.* 78 (1989) 281–293.
- [38] S.H. Kim, P.D. Battle, *J. Magn. Magn. Mater.* 123 (1993) 273–282.
- [39] P.S.R. Murthy, K.R. Priolkar, P.A. Bhobe, A. Das, P.R. Sarode, A.K. Nigam, *Eur. Phys. J. B* 78 (2010) 275–282.
- [40] M. Dlouhá, J. Hejtmánek, Z. Jiráček, K. Knížek, P. Tomeš, S. Vratislav, *J. Magn. Magn. Mater.* 322 1189–1191.
- [41] J.-W.G. Bos, J.P. Attfield, T.-S. Chan, R.-S. Liu, L.-Y. Jang, *Phys. Rev. B* 72 (2005) 014101.
- [42] J.-W.G. Bos, J.P. Attfield, *Chem. Mater.* 16 (2004) 1822–1827.
- [43] A. Mamchik, W. Dmowski, T. Egami, I.-W. Chen, *Phys. Rev. B* 70 (2004) 104410.
- [44] I. Terasaki, Y. Sasago, K. Uchinokura, *Phys. Rev. B* 56 (1997) R12685–R12687.
- [45] T.M.M. Tritt, *Proceedings - Electrochem. Soc.* 2003-27 (2004) 257.
- [46] M. Shikano, R. Funahashi, *Appl. Phys. Lett.* 82 (2003) 1851.
- [47] M. Ohtaki, Eighteenth International Conference On Thermoelectrics, 1999, 565–568.
- [48] P. Tomeš, J. Hejtmánek, K. Knížek, *Solid State Sci.* 10 (2008) 486–490.
- [49] R.D. Shannon, *Acta Cryst.* A32 (1976) 757 – 767.
- [50] M.K. Crawford, M.A. Subramanian, R.L. Harlow, J.A. Fernandez-Baca, Z.R. Wang, D.C. Johnston, *Phys. Rev. B* 49 (1994) 9198–9201.
- [51] M.A. Subramanian, M.K. Crawford, R.L. Harlow, T. Ami, J.A. Fernandez-Baca, Z.R. Wang, D.C. Johnston, *Physica C* 235-240 (1994) 743–744.
- [52] Z. Ropka, R. Radwanski, *Phys. Rev. B* 67 (2003).
- [53] R.J. Radwanski, Z. Ropka, *Physica B: Condens. Matter* 345 (2004) 107–110.
- [54] J.A. García, M.E. Villafuerte-Castrejón, J. Andrade, R. Valenzuela, A.R. West, *Mater. Res. Bull.* 19 (1984) 649–654.
- [55] D. Mikhailova, H. Ehrenberg, G. Miehe, D. Trots, C. Hess, R. Schneider, H. Fuess, *J. Solid State Chem.* 181 (2008) 190–198.
- [56] A.L. Ivanovskii, T.I. Chupakhina, V.G. Zubkov, A.P. Tyutyunnik, V.N. Krasilnikov, G.V. Bazuev, S.V. Okatov, A.I. Lichtenstein, *Phys. Lett. A* 348 (2005) 66–70.
- [57] W.H. Baur, *Crystallogr. Rev.* 13 (2007) 65–113.
- [58] J.P. Badaud, *Comptes Rendus Hebdomadaires Des Séances De l'Académie Des Sciences. Série C. Sciences Chimiques* 278 (1974) 521.
- [59] H. Leiva, R. Kershaw, K. Dwight, A. Wold, *J. Solid State Chem.* 47 (1983) 293–300.

- [60] L. Degueldre, Y. Gobillon, L. Clerbols, L. Bourgeois, U.S. Patent 3,736,270.
- [61] V.. Lazarev, I.. Prosychev, S.. Shaplygin, *Zh. Neorg. Khim.* 24 (1979) 313.
- [62] T. Siritanon, K. Biswas, A.W. Sleight, M.A. Subramanian, *Mater. Res. Bull.* 46 (2011) 2016–2020.
- [63] J. Isasi, M.L. López, M.L. Veiga, C. Pico, *J. Alloys Compd.* 232 (1996) 36–42.
- [64] M.J. Isasi, R. Sáez-Puche, M.L. Veiga, C. Pico, A. Jerez, *Mater. Res. Bull.* 23 (1988) 595–601.
- [65] J. Isasi, M.L. Veiga, Y. Laureiro, R. Saez-Puche, C. Pico, *J. Alloys Compd.* 177 (1991) 143–147.
- [66] J. Isasi, M.L. Veiga, F. Fernandez, C. Pico, *J. Mater. Sci.* 31 (1996) 4689–4692.
- [67] H. Mizoguchi, L.N. Zakharov, W.J. Marshall, A.W. Sleight, M.A. Subramanian, *Chem. Mater.* 21 (2009) 994–999.

CHAPTER 4

Structure – Property relationships in the K_2NiF_4 - type structure of Sr_2IrO_4 and Sr_2TiO_4 .

4.1 Abstract

Ir is a 5d transition metal that is part of the platinum group of metals. Its fascinating history is reviewed as well the variety of ternary and quaternary Ir oxides formed. One of the more unique structures adopted by an Ir oxide is the K_2NiF_4 -type structure. This structure is briefly discussed and Sr_2IrO_4 adopting the K_2NiF_4 -type structure is investigated in detail. In particular the effects of Ti, Fe and Co substitutions for Ir on the structure and on the physical properties of Sr_2IrO_4 are investigated. A complete solid solution $Sr_2Ir_{1-x}Ti_xO_4$ is obtained while both Fe and Co doping are relatively limited. In each case however, the c -axis cell parameter and the initial IrO_6 octahedra tilting decreases with substitution. Doping with Ti, Fe and Co results in a decrease of the magnetic susceptibility and in an increase in the paramagnetic effective moment for Co and Fe doped samples and a suppression of the weak ferromagnetic ordering observed for Sr_2IrO_4 . Further investigations into $Sr_2Ti_{1-x}Rh_xO_4$ phases reveal an incomplete solid solution of up to $x = 0.6$ with effects of octahedral tilting present in Sr_2RhO_4 observed with higher Rh content. Compositions with higher Rh content show higher magnetic susceptibilities and electrical conductivities; however, all the compositions show paramagnetic and semiconducting behavior in the 5 – 300 K temperature regime.

Publications based on this chapter:

- [1] A.J. Gatimu, R. Berthelot, S. Muir, A.W. Sleight, M.A. Subramanian, *Journal of Solid State Chemistry* 190 (2012) 257–263.

4.2 Introduction

4.2.1 Ir and its oxides.

Ir is a transition metal element in the 5d block of the periodic table (electronic configuration: $[\text{Xe}]4f^{14}5d^76s^2$). It is commonly referred to as one of the six members of the platinum group of metals, with Ru, Rh, Pd, Os and Pt being the other members of the collection. Of these metals, Ir is the most resistant to corrosion and oxidation. It is also insoluble in mineral acids including aqua regia and is also impervious to molten metals and high temperature silicates [1].

Mechanically, Ir also has a very high modulus of elasticity and rigidity, coupled with a very low Poisson's ratio, and thus exemplifies high stiffness and deformation resistance. These mechanical properties are sustained in air at temperatures above 1600 °C which is a unique property of Ir [1].

Joseph Louis Proust, while working under the patronage of King Carlos IV in Madrid, was first to notice Ir as insoluble residue from the dissolution of Pt ore in aqua regia in 1799. However, he failed to identify the residue as Ir but instead described it as "Nothing else than graphite or plumbago" (plumbago being a reference to mineral graphite) [1]. It was not until June 21st 1804 that Smithson Tennant identified that the insoluble residue was a mixture of Osmium and Iridium in a Royal Science publication [2].

Early applications of Iridium were as tips for pens with John Isaac Hawkins succeeding in manufacturing a gold pen with Ir tips in 1834 [1]. This was a significant accomplishment given the high mechanical strength of Ir. More recent applications have included temperature measurement in thermocouples. One obvious advantage of using Ir thermocouples is measurement of higher temperatures up to ~ 2000 °C in air [3]. This results from the very high melting point of Ir (~ 2460 °C). Similarly, Ir can be used as the main element for a furnace, allowing for very high temperature investigations.

The high melting point of Ir has proved very useful in its use as a crucible for growing oxide single crystals for electronics such as Gadolinium Gallium Garnet (GGG) and Yttrium Aluminium Garnet (YAG) in oxidizing conditions at up to 2100 °C. These crystals tend to be grown by the Czochralski technique and Ir crucibles can size up to hold 6280 ml and have a thickness of up to 4.00 mm [4]. Figure 4.1 shows the large size of these Ir crucibles.

Space travel has introduced a new application for Ir as shields for nuclear thermoelectric generators that power space probes such as the Voyager. The Ir encapsulation is necessary due to its high melting point and great mechanical strength that are necessary to withstand the conditions in outer space [5]. Addition of 60 ppm of Thorium to Ir halves the rate of oxidation and increases the stress rupture life and is thus utilized in a majority of probes.



Figure 4.1. Typical flat bottomed Ir crucible used for growth of metal oxide single crystals such as Gadolinium Gallium Garnet (GGG). The crucible pictured has a diameter of 180 mm and a capacity of 4330 ml.

Further uses of Ir have included radioactive isotope Ir-192 as a portable gamma ray source for use in radiography in civil engineering structures and for cancer radiotherapy treatment [4].

Binary, ternary and quaternary Ir oxides are well known. In the majority of the oxides, the Ir oxidation state is 4+, however, oxides with Ir in 5+ and 6+ oxidation states are known. Many of the oxides can be prepared by rapid solid state reactions [6] and have a variety of electrical and magnetic properties. Furthermore, despite the current prohibitive high cost, likely potential future applications could become apparent.

In considering Ir(IV) oxides, structurally, most of the oxides will adopt either a LiSnO_3 -type structure such as in Li_2IrO_3 [7], a perovskite structure, or a pyrochlore structure such as in $\text{Bi}_2\text{Ir}_2\text{O}_7$ [8]. Other common structures of Ir(IV) oxides include derivatives of the perovskite structure such as multilayer

hexagonal or orthorhombic structures. The K_2NiF_4 structure such as in Sr_2IrO_4 is also well known for Ir(IV) oxides. This variety of Ir(IV) oxide structures is shown in table 4.1.

Ir (IV) Oxide Compound	Structure type	Unit cell Symmetry	a cell parameter (Å)	b cell parameter (Å)	c cell parameter (Å)
Li_2IrO_3	Li_2SnO_3	Monoclinic	5.163	8.923	9.821
Na_2IrO_3	Li_2SnO_3	Monoclinic	5.435	9.416	10.76
Ca_4IrO_6	K_4CdCl_6	Hexagonal	9.329		11.24
$SrIrO_3$	$BaTiO_3$ (Distorted Perovskite)	Monoclinic	5.603	9.612	14.16
Sr_2IrO_4	K_2NiF_4	Tetragonal	3.883		12.89
$Y_2Ir_2O_7$	Pyrochlore	Cubic	10.16		
$Pb_2Ir_2O_6$	Pyrochlore	Cubic	10.26		
IrO_2	Rutile	Tetragonal	4.495		3.149

Table 4.1. Structure types and unit cell dimensions of some Ir(IV) oxides. Adapted from [6].

One of the few examples of known of an Ir(VI) oxide is Ca_3IrO_6 [9]. $Ca_2Ir_2O_7$, $Cd_2Ir_2O_7$, $Ba_{0.5}IrO_3$ and $Sr_{0.5}IrO_3$ synthesized hydrothermally by Sleight are some known examples of Ir(V) oxides. It is important to note that mixed valent Ir oxides are known in which Ir tends to be in both a 4+ and 5+ oxidation state. Examples include $Pb_2Ir_2O_{6.5}$ [10] which lies in the $Pb_2Ir_2O_{7-x}$ ($x = 0 - 1$) solid solution.

Electrically, most Ir oxides show delocalized electron behavior with metallic and semiconducting behavior exhibited [6]. Magnetically,

ferromagnetism and antiferromagnetism are observed for many Ir oxides. This is particularly true for Ir(IV) oxides with the perovskite structure which allows for 3-dimensional magnetic interactions to occur and for Ir(IV) oxides with the K_2NiF_4 structure which allows for 2-dimensional magnetic interactions to occur.

4.2.2 K_2NiF_4 Structure

Potassium Nickel Fluoride (K_2NiF_4) crystallizes in a tetragonal, body centered unit cell with an a cell parameter of 4.00 Å and a c cell parameter of 13.07 Å [11]. The structure is related to that of an ideal cubic perovskite in that octahedral (BO_6) layers similar to those in an ABO_3 perovskite are now separated by rock salt layers. Specifically, NiF_6 octahedra layers are separated by rocksalt layers of K as shown in figure 4.2.

It should be noted that tolerance factors for A_2BO_4 compounds with the K_2NiF_4 structure like Sr_2TiO_4 , Ca_2MnO_4 and $SrLaAlO_4$ are very close to 1 (between 0.95 – 0.985 for the examples listed) [12]. This high tolerance factor suggests more stringent A cation size conditions for the K_2NiF_4 structure compared to the perovskite structure.

Deviations from the ideal K_2NiF_4 – type structure are known. Octahedral tilting within the structure can occur and this leads to a lowering in symmetry from the ideal tetragonal $I4/mmm$ space group symmetry. A key example of this is in Sr_2IrO_4 which is investigated in detail in this chapter. Other deviations can result with ordering such as in $Sr_2In_{0.5}Sb_{0.5}O_4$ where

ordering between In^{3+} and Sb^{5+} lead to an expanded unit cell and small orthorhombic distortion, in addition to octahedral tilting [12].

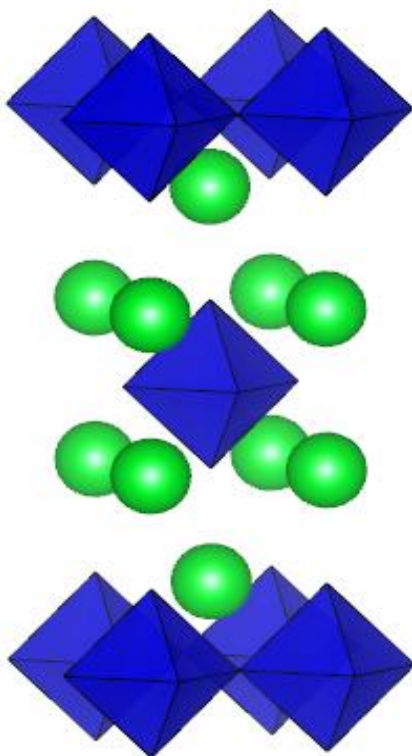


Figure 4.2. Depiction of the K_2NiF_4 structure. The green spheres represent the rock salt layers of K separating the blue NiF_6 octahedra which corner share in a similar fashion to BO_6 octahedra in the cubic ABO_3 perovskite structure. The presence of rock salt layers contributes to an extension of the c cell parameter and a tetragonal unit cell.

4.3 Synthesis and characterization of $\text{Sr}_2\text{Ir}_{1-x}\text{M}_x\text{O}_4$ ($\text{M} = \text{Ti}, \text{Fe}, \text{Co}$) solid solutions.

4.3.1 Introduction

Transition metal oxides display a wide variety of structural and physical properties and continue to be of great interest to researchers. Oxides with a K_2NiF_4 -type structure have been intensively investigated following the discovery of superconductivity in $\text{La}_{2-x}\text{Ba}_x\text{CuO}_4$ compositions [13]. Soon after, researchers identified Sr_2IrO_4 as another intriguing composition due to its structural and electronic similarities with La_2CuO_4 [14–16]. Both are Mott insulators at room temperature and contain a transition metal with spin $\frac{1}{2}$ and a half filled d -band. These similarities have led some researchers to theorize that doped Sr_2IrO_4 compounds can exhibit interesting behaviors including high temperature superconductivity, as in the case of doped cuprates [17].

Numerous studies have therefore explored the influence of electron and hole doping in Sr_2IrO_4 , as well as aliovalent substitution, in search of superconductivity and other interesting phenomena. Electron doping can be achieved by La^{3+} substitution on the Sr site; however the doping limit differs from one study to another with less than 5% according to Klein and Terasaki [18] and up to 20% for Cosio-Castaneda and coworkers [19]. This substitution led to a notable decrease of the resistivity although keeping a semiconducting dependence. Introduction of very dilute oxygen vacancies can also lead to electron doping; single-crystals of $\text{Sr}_2\text{IrO}_{4-\delta}$ with $\delta \leq 0.04$ demonstrated reduced lattice parameters and an insulator-to-metal transition at 105 K [20–22]. As Sr_2RuO_4 also adopts the K_2NiF_4 -type structure, Ir substitution by Ru

(hole doping for small Ru fractions) has been also investigated through the complete solid solution $\text{Sr}_2\text{Ir}_{1-x}\text{Ru}_x\text{O}_4$ [16]. These compositions exhibit an interesting insulator-to-metal transition for $x \sim 0.6 - 0.8$ coinciding with a maximum in the effective paramagnetic moment observed. It is also reported that Ca^{2+} and Ba^{2+} can be substituted for Sr^{2+} in small fractions with little influence on magnetic and transport properties [23].

Structurally, Sr_2IrO_4 was first assumed to adopt the ideal K_2NiF_4 -type structure, *i.e.* a perovskite framework of IrO_6 corner-shared octahedra forming IrO_2 planes and separated by a SrO double layer [24] (Figure 4.3a-b). However, further electron and neutron diffraction studies on polycrystalline samples revealed some superstructure peaks and indicated a modified crystal structure due to a low rotation of IrO_6 octahedra of about $\theta = 11^\circ$ about the crystallographic c -axis (Figure 4.3c) [14,25]. This structural change results in a less symmetric space group $I4_1/acd$ compared to the initial $I4/mmm$, and the larger modified unit cell with the dimensions $a = 5.4979(2)\text{\AA} = \sqrt{2} a_0$ and $c = 25.798(1)\text{\AA} = 2 c_0$ where a_0 and c_0 stand for the cell parameters of the initial unit cell. Note that a similar structural distortion has been observed in Sr_2RhO_4 [15] and Ca_2MnO_4 [26,27]. To our knowledge Sr_2IrO_4 is the only K_2NiF_4 -type transition metal oxide containing a 5d cation.

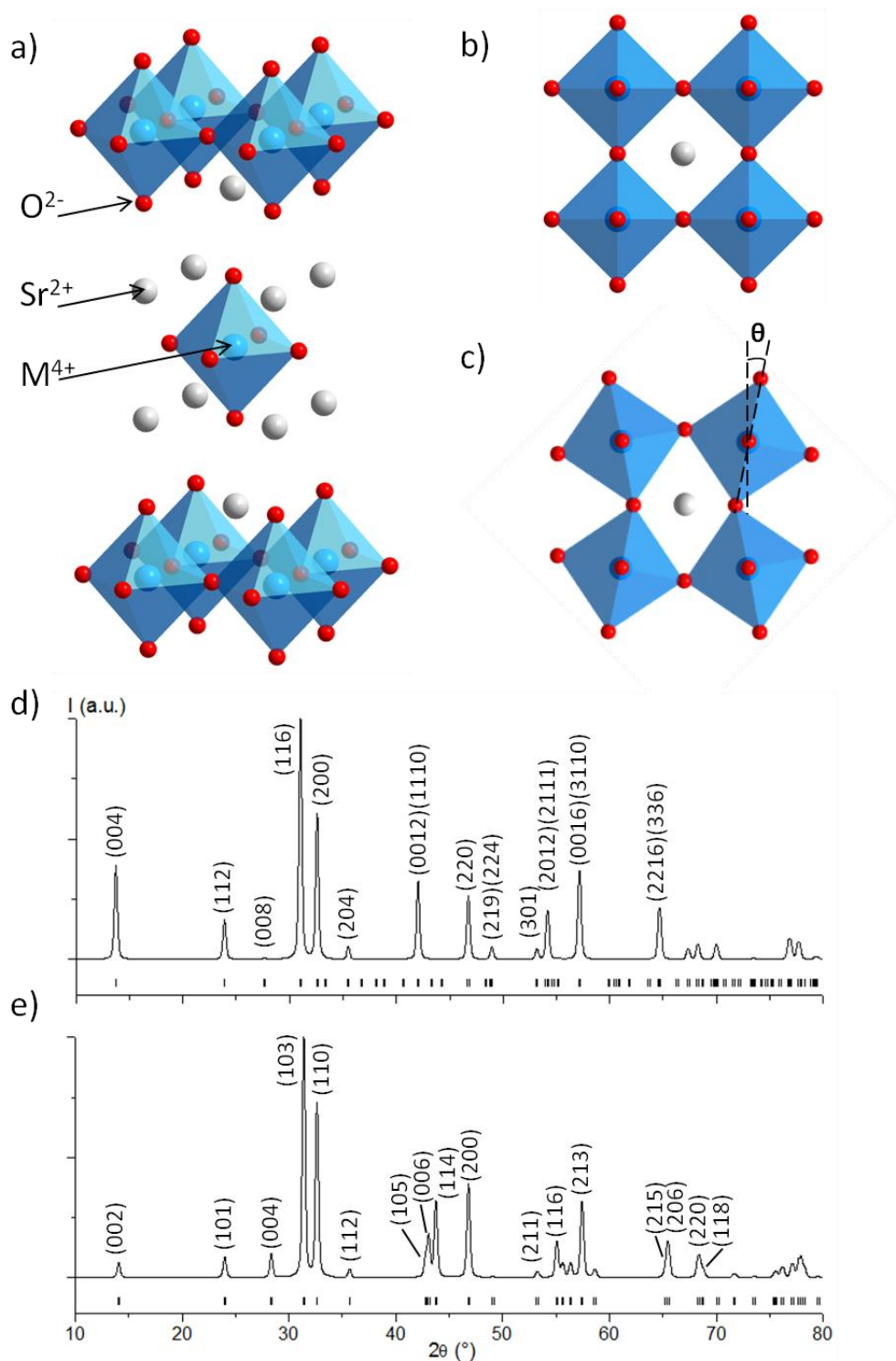


Figure 4.3. Representation of the K_2NiF_4 -type structure for Sr_2MO_4 (M = Ti, Fe, Co) in a perspective view (a) and in projection in the (a,b) plane (b). In case of Sr_2IrO_4 , the same latter projection (c) evidences the octahedra tilting $\theta \sim 11^\circ$ around the c axis. Simulated XRD patterns of Sr_2IrO_4 (d) from [14] and Sr_2TiO_4 (e) from [28] are shown for comparison.

In the following section the investigation of Ir substitution by three different 3d transition metals (Ti, Fe and Co) is discussed. These metals were chosen as Sr_2TiO_4 , Sr_2FeO_4 and Sr_2CoO_4 compounds all adopt the ideal K_2NiF_4 -type structure [28–30] and there was an interest in investigating the evolution of structure-property relationships as the transition metal coordination moves back towards ideality. These solid-state substitutions are studied by X-ray diffraction, magnetism and electrical measurements.

4.3.2 Results and Discussion

4.3.2.1 X-Ray Diffraction characterization

$\text{Sr}_2\text{Ir}_{1-x}\text{Ti}_x\text{O}_4$ complete solid solution

X-Ray diffraction (XRD) patterns obtained from the nominal compositions $\text{Sr}_2\text{Ir}_{1-x}\text{Ti}_x\text{O}_4$ ($0 \leq x \leq 1$) are shown in figure 4.4a. Single phase patterns were obtained at all values of x , indicating a complete solid solution from Sr_2IrO_4 to Sr_2TiO_4 .

From a structural point, the interest of this complete solid solution is the transition from the tilted ($I4_1/acd$) to the ideal ($I4/mmm$) structure. The octahedral tilting (θ) should disappear with Ti substitution as the structure adopts the ideal K_2NiF_4 -type structure. An initial close comparison of the simulated XRD patterns of both Sr_2IrO_4 from [14] and Sr_2TiO_4 from [28] highlights some clear differences between them (Figure 4.3d-e). For example at $\sim 8^\circ$ in 2θ , the (0,0,4) peak becomes (0,0,2) while its intensity dramatically decreases. On the contrary at $\sim 28^\circ$, the weak (0,0,8) peak observed for

Sr_2IrO_4 becomes more intense as it transitions to the (0,0,4) for Sr_2TiO_4 . As it is sometimes difficult to correctly track the evolution of diffraction peak intensity, it is more reasonable to focus on the $40 - 48^\circ 2\theta$ range, where the indistinguishable (0,0,12) and (1,1,10) peaks observed for Sr_2IrO_4 are replaced by the three distinct peaks (1,0,5), (0,0,6) and (1,1,4) in the case of Sr_2TiO_4 (Figure 4.4b). However, these initial observations can be misleading as it is important to also consider symmetry and scattering factor effects in these XRD patterns. The Ir end member has a larger unit cell and lower symmetry and thus an XRD pattern with more peaks is expected. In addition, Ir and Ti possess different scattering powers and thus some peak intensities may vary from Sr_2IrO_4 to Sr_2TiO_4 . XRD simulations show that this is actually the case for the (1,1,4) peak of Sr_2TiO_4 which becomes very weak in theoretical Sr_2IrO_4 with no IrO_6 tilting. Neutron diffraction experiments can overcome this problem. However, the high cost of iridium precursors and the large mass of samples required for neutron diffraction hindered performance of such an analysis. Therefore, we tried to clarify the Sr_2IrO_4 to Sr_2TiO_4 transition by focusing on the evolution of cell parameters.

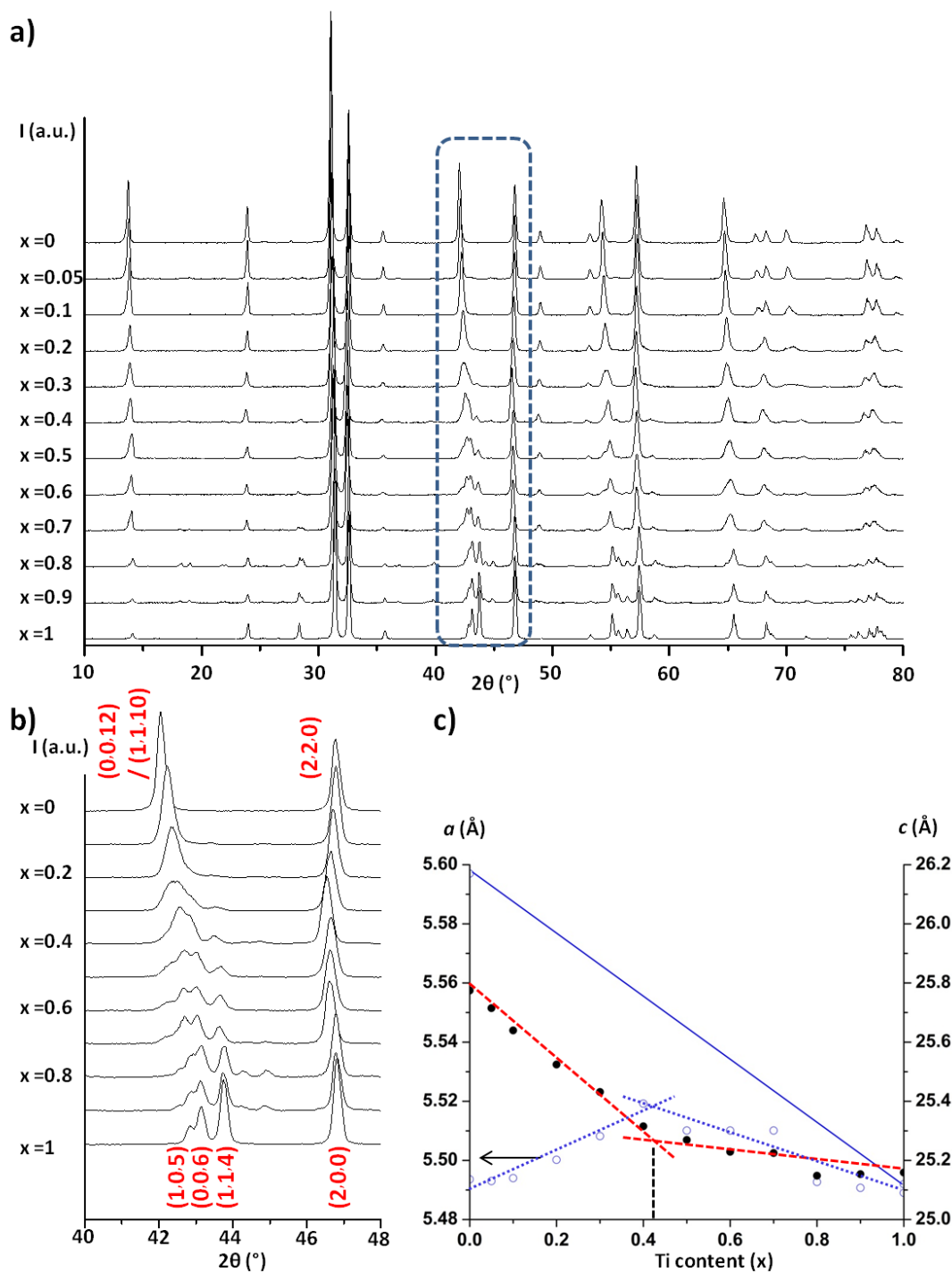


Figure 4.4. (a) XRD patterns of the entire solid solution $\text{Sr}_2\text{Ir}_{1-x}\text{Ti}_x\text{O}_4$ on the whole 2θ range and (b) a focus on the $40 - 48^\circ 2\theta$ region that highlights the transition $I41/acd$ to $I4/mmm$. (c) Refined values of the cell parameters. The a cell parameter has been multiplied by $\sqrt{2}$ for compositions with the Sr_2TiO_4 structure. The dotted and dashed lines highlight the a and c parameter evolutions respectively. The solid line represents the theoretical a parameter

evolution in the case of no octahedra tilting (*i.e.* I4/mmm space group from Sr₂IrO₄ to Sr₂TiO₄)

From Sr₂IrO₄ to Sr₂TiO₄, the *c* parameter significantly decreases (Figure 4.4c) which is as expected considering the ionic radii of Ir⁴⁺ and Ti⁴⁺ (respectively 0.625 and 0.605 Å in a 6-fold coordination [31]). Two distinct linear trends are noticed on either side of *x* = 0.4. The change in the *a* cell parameter with changing *x* is much less than the *c* parameter change. This is due to the presence of two competing processes, which tend to cancel each other. The smaller size of Ti will contribute to a decrease in *a*, but the expected decrease in octahedral tilting will contribute to an increase in *a*. Clearly, the decreased tilting dominates the change in *a* as Ti is first introduced (Figure 4.4c). However, there is then a change from a positive to a negative slope (highlighted by the two dotted lines) at the same Ti content where there is a change in slope for the *c* cell parameter (highlighted by the dashed lines). The solid line indicates the expected change in the *a* cell parameter if the octahedral tilting did not occur. This line is based on the assumption that the M-O distance will be a simple weighted average of the values observed for the end members. In the case of the ideal Sr₂TiO₄ structure, the *a* cell parameter is simply twice the Ti-O distance in the *ab* plane. (For ease of comparison the values in the figures for *a* are multiplied by $\sqrt{2}$ for the high *x* compositions.) Essentially all values of *a* fall below the ideal value based on no tilting of octahedra. At high values of *x* some of this deviation might be due to compression of Ir in the smaller Ti lattice. However, this deviation is expected to be primarily caused by the tilting of the

octahedra. This tilting is assumed to be disordered for values of x greater than 0.4. The impact of tilting on the a cell parameter then becomes more significant when the tilting becomes ordered at values of x less than 0.4. We have no direct proof of the change of space group from $I4_1/acd$ to $I4/mmm$ at about $x = 0.4$, but such a change must occur at some value of x , which is most likely 0.4. From simple geometric considerations, we can calculate the amount of octahedra tilting necessary to decrease the value of a from the ideal value of a to the value of a actually observed. This gives a tilt angle of 6.8° for $x = 0.4$ compared to the tilt angle of 11° observed for $x = 0.0$.

$Sr_2Ir_{1-x}M_xO_4$ ($M = Fe, Co$) partial solid solutions

XRD patterns obtained for the compositions $Sr_2Ir_{1-x}Fe_xO_4$ ($0 \leq x \leq 0.5$) and $Sr_2Ir_{1-x}Co_xO_4$ ($0 \leq x \leq 0.4$) are shown in Figure 4.5a and 4.5b. Weak impurity peaks are detected for $Sr_2Ir_{0.5}Fe_{0.5}O_4$ and $Sr_2Ir_{0.6}Co_{0.4}O_4$. For higher contents, impurity traces clearly increase; therefore, the solid solutions are in these cases not complete. As for the Ti case, an increase of the Fe or Co content directly impacts the XRD patterns and therefore the cell parameters. A close look in the $40 - 50^\circ 2\theta$ region (Figure 4.5a and 4.5b) highlights the distinct changes in the XRD patterns.

In the case of Fe, despite the presence of weak impurities, it is still possible to refine the cell parameters of the main $Sr_2Ir_{1-x}Fe_xO_4$ phase until $x = 0.6$ (Figure 4.5c). Similar to $Sr_2Ir_{1-x}Ti_xO_4$, the c parameter evolution can be split into two linear regions with distinct slopes around $x = 0.4$. Above this

content limit, the c parameter evolution may follow a linear trend until the pure end-member Sr_2FeO_4 , as it is suggested in figure 4.5c.

The solubility threshold in $\text{Sr}_2\text{Ir}_{1-x}\text{Co}_x\text{O}_4$ is even more limited, as some impurities are revealed for a Co content up to 0.4. Below this limit, the c cell parameter linearly decreases to finally reach $\sim 25.0 \text{ \AA}$, which is close to the c value of Sr_2CoO_4 [30].

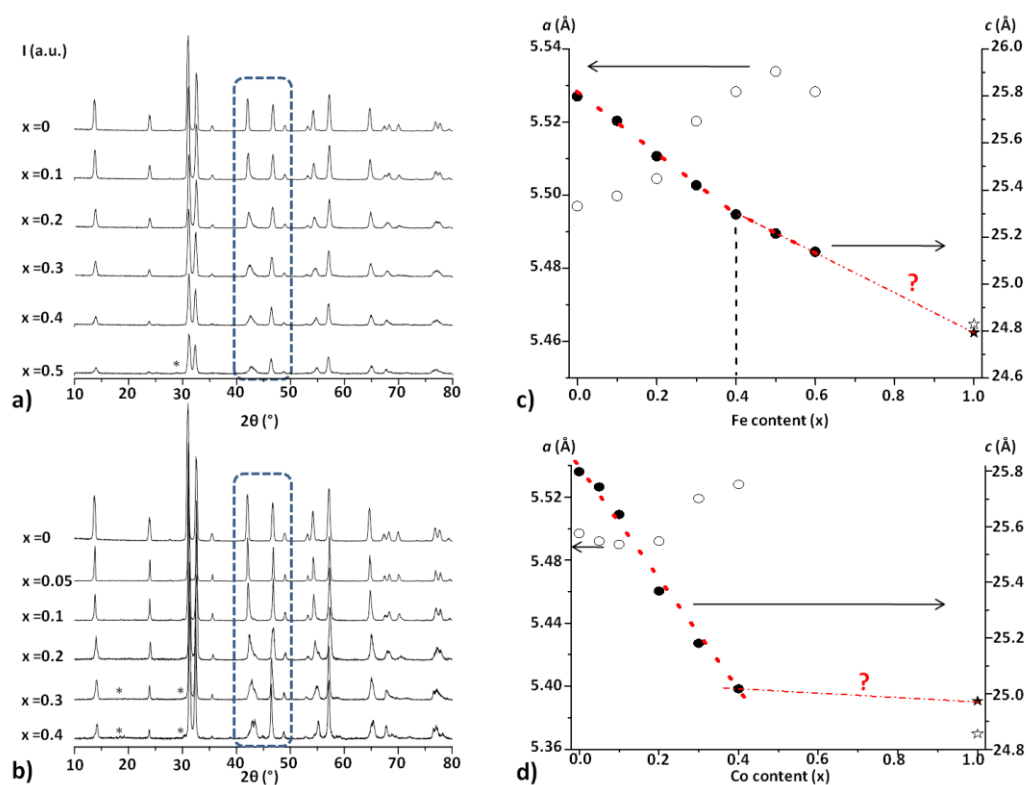


Figure 4.5. XRD patterns of (a) $\text{Sr}_2\text{Ir}_{1-x}\text{Fe}_x\text{O}_4$ (up to $x = 0.5$) and (b) $\text{Sr}_2\text{Ir}_{1-x}\text{Co}_x\text{O}_4$ (up to $x = 0.4$). Weak peak impurities are marked by a * symbol. (c and d). Evolution of the corresponding cell parameters a (empty circles) and c (black circles). Sr_2FeO_4 and Sr_2CoO_4 values (star) are taken from the literature [29,30]. The dashed lines (in c and d) show that the c parameter evolution can be split into two linear regions with distinct slopes around $x = 0.4$ and may then linearly decrease to the Fe and Co end members.

In both cases, the evolution of the a parameter is more difficult to analyze as the variation is minimal for the same reasons discussed for $\text{Sr}_2\text{Ir}_{1-x}\text{Ti}_x\text{O}_4$. However a weak increase is revealed from the pure Sr_2IrO_4 end-member to the solubility limit. For higher M content ($M = \text{Fe}$ or Co), a decrease can be assumed as the final a parameter values of both Sr_2FeO_4 and Sr_2CoO_4 are significantly lower.

As the c cell parameter of Sr_2IrO_4 is higher than that of Sr_2TiO_4 , Sr_2FeO_4 and Sr_2CoO_4 , it is then logical to observe a decrease of the parameter when Ir is substituted by either Ti, Fe or Co. In each case however, the decrease is not totally linear and can be split into two distinct domains. Below the transition, the space group $I4_1/acd$ gives a better profile matching fit than $I4/mmm$. Above the transition however, it is better to use the latter one. Note that in the complete solution $\text{Sr}_2\text{Ir}_{1-x}\text{Ru}_x\text{O}_4$, which is also a transition from $I4_1/acd$ to $I4/mmm$, the c parameter evolution is also not completely linear [16]. As with the a parameter, these observations must be related to the tilting of the MO_6 octahedra that characterizes the Sr_2IrO_4 structure in addition to the changing octahedral M-O distance.

It is interesting to compare the influence of the Ir substitution by Ti, Fe, or Co. The crystallographic transition between $I4_1/acd$ and $I4/mmm$ does not affect the Ti insertion. The $\text{Sr}_2\text{Ir}_{1-x}\text{Ti}_x\text{O}_4$ solid solution is complete, similar to the $\text{Sr}_2\text{Ir}_{1-x}\text{Ru}_x\text{O}_4$ solid solution [16]. However, the Fe and Co solid solutions are not complete, which may be explained by the large difference between ionic radii. In addition, there is no report on the ambient pressure

solid-state synthesis of Sr_2FeO_4 and Sr_2CoO_4 ; however, high-pressure methods have been used to stabilize both compositions with ideal K_2NiF_4 -type structures [29,30]. It is then reasonable to assume that complete solid solutions $\text{Sr}_2\text{Ir}_{1-x}\text{Fe}_x\text{O}_4$ and $\text{Sr}_2\text{Ir}_{1-x}\text{Co}_x\text{O}_4$ can be obtained by using such high-pressure techniques.

4.3.2.2 Physical measurements

$\text{Sr}_2\text{Ir}_{1-x}\text{Ti}_x\text{O}_4$ complete solid solution

The Sr_2IrO_4 composition shows ferromagnetic ordering with a T_c near 250 K; the origins of which have been difficult to precisely determine. Earlier investigations pointed out that Ir^{4+} has a relatively large amount of spin-orbit coupling and that Dzyaloshinskii-Moriya (DM) interactions, driven by IrO_6 octahedra structural distortion, are what lead to the ferromagnetic (FM) ordering observed [14,15]. At one point, it was suggested from single crystal studies that Sr_2IrO_4 may be a band ferromagnet, with low density of charge carriers given that the effective moment to saturated moment ratio, $\mu_{\text{eff}}/\mu_{\text{Sat}}$, is greater than unity [20]. However a later study demonstrated that spin-orbit interactions were in fact responsible for the FM state [32]. This has also been supported by a more recent theoretical investigation which also points out the importance of spin-orbit coupling within the system and how it plays a key role in observed physical properties [17].

The overall magnetic behavior of the $\text{Sr}_2\text{Ir}_{1-x}\text{Ti}_x\text{O}_4$ solid solution (Figure 4.6a) can be explained by considering two facts, 1) introducing Ti^{4+} will dilute the observed magnetic moment as it has $3d^0$ electronic

configuration and 2) the average M-O-M bond angle will increase to the ideal I4/mmm M-O-M angle of 180° as a result of Ti substitution. Previous studies of $\text{Sr}_2\text{Ir}_{1-x}\text{Ru}_x\text{O}_4$ powder samples and $\text{Sr}_2\text{IrO}_{4-\delta}$ single crystals have demonstrated that the physical properties for these compositions are quite sensitive to the M-O-M angle [16,20].

Given the lack of d electrons in the Ti^{4+} ion, a loss in the overall magnetization as Ti^{4+} is substituted for Ir^{4+} in the $\text{Sr}_2\text{Ir}_{1-x}\text{Ti}_x\text{O}_4$ solid solution is expected. Looking at figure 4.6a we can see that the low temperature molar susceptibility does indeed decrease as more Ti is incorporated into the structure. For Sr_2IrO_4 we observe an effective moment, μ_{eff} , of $0.33 \mu_{\text{B}}$ by fitting from 265 - 325 K. Similar to ref. [16], data were corrected for core diamagnetism and then fit using a modified Curie-Weiss law, $\chi = C / (T - \theta) + \chi_0$, where χ_0 , found to be 4.1×10^{-4} emu/mol, represents the temperature independent paramagnetism and θ , found to be 246 K, represents the Weiss constant. Sr_2TiO_4 was found to be diamagnetic with a nearly temperature independent molar susceptibility of approximately 2×10^{-4} emu / mol. Figure 4.6b shows the molar susceptibility plotted as emu per mol of Ir^{4+} near the Curie transition temperature of ~ 250 K for Sr_2IrO_4 . For $x = 0.1$ there is a slight depression of the onset transition temperature however for $x \geq 0.2$ there is relatively little change. Figure 4.6c details the magnetization versus magnetic field characteristics of the $\text{Sr}_2\text{Ir}_{1-x}\text{Ti}_x\text{O}_4$ solid solution between -5 and 5 T at temperature of 5 K. The saturation moment for Sr_2IrO_4 at 5 T is found to be $\sim 0.06 \mu_{\text{B}} / \text{Ir}^{4+}$. The low temperature molar susceptibility (Figure

4.6a) and M - H measurements (Figure 4.6c) compositions indicate that there is an increasing paramagnetic contribution as Ti content increases. This leads to a decrease in the observed magnetic moment per mole of M^{4+} ions, shown in the inset of figure 4.6c, which appears to change strongly for $x = 0.0 - 0.3$ and then less strongly for $x = 0.5 - 0.8$. Interestingly this correlates well with the change in lattice parameters observed by powder XRD and supports the idea that below $x \sim 0.4$ there must still be significant octahedral tilting and antiferromagnetic (AFM) Ir - O - Ir interactions, leading to a weak FM state driven by canting, while above $x \sim 0.4$ the tilting is further diminished and the Ir^{4+} ions are sufficiently dilute leading to paramagnetic interactions. Nevertheless susceptibility measurements give evidence of a weak FM transition even for $x = 0.7$ and this would seem to necessitate that some AFM Ir - O - Ir interactions and octahedral tilting remain.

Contrary to conventional band theory Sr_2IrO_4 is semiconducting and has been referred to as a Mott insulator [17] where the insulating state results from spin-orbit coupling induced narrowing of Ir *d*-bands. Samples within the $Sr_2Ir_{1-x}Ti_xO_4$ solid solution exhibit semiconducting behavior, as shown in figure 4.6d, and this is in agreement with the already reported behavior of the end members Sr_2IrO_4 [16] and Sr_2TiO_4 [33]. It is also interesting to note there is a color change with an increasing Ti substitution; Sr_2IrO_4 is black and compositions progressively turn to green-brown until becoming white at Sr_2TiO_4 .

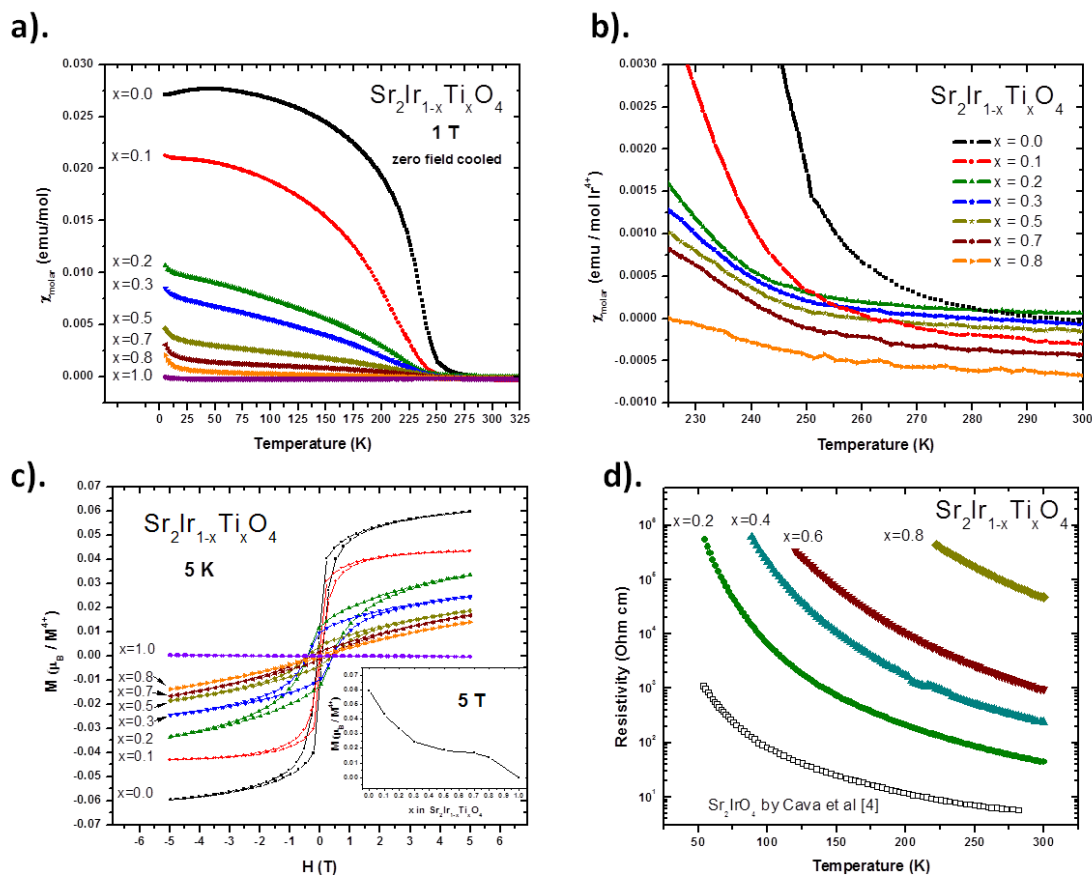


Figure 4.6. Magnetic molar susceptibility (a), molar susceptibility as per emu per mol of Ir^{4+} near the Curie transition temperature (b), magnetization versus magnetic field between -5 and 5 Tesla at 5 K (c), and electrical resistivity (d) evolution in temperature from 5 to 300 K of $\text{Sr}_2\text{Ir}_{1-x}\text{Ti}_x\text{O}_4$ samples. Sr_2IrO_4 resistivity data are taken from a previous work [16]. In case of the pure Sr_2TiO_4 , too high resistivity prevented four probe measurements.

$\text{Sr}_2\text{Ir}_{1-x}\text{M}_x\text{O}_4$ (M=Fe and Co)

Figure 4.7a and 4.8a gather the evolution in temperature of the magnetic susceptibility for $\text{Sr}_2\text{Ir}_{1-x}\text{Fe}_x\text{O}_4$ and $\text{Sr}_2\text{Ir}_{1-x}\text{Co}_x\text{O}_4$ samples up to $x = 0.5$ and $x = 0.3$ respectively. As in the previous case of the Ti substitution, both Fe and Co doping lead to a gradual decrease of the magnetic susceptibility at low temperature. According to previous Mössbauer spectroscopy analysis, only the presence of Fe^{4+} cations in pure Sr_2FeO_4 is confirmed (*i.e.* no oxygen vacancies) [34]. In addition, magnetic

measurements carried out on pure Sr_2CoO_4 confirmed the presence of Co^{4+} in the intermediate spin state [35]. Even if the synthesis of these two end-members requires a high-pressure technique, we can assume that conventional solid state methods lead to the substitution of Ir^{4+} by Fe^{4+} and Co^{4+} respectively. Note that an antiferromagnetic signal is detected at low temperature for the $\text{Sr}_2\text{Ir}_{0.7}\text{Co}_{0.3}\text{O}_4$ and can be attributed to Co_3O_4 ($T_N = 34$ K) presence which is not visible by XRD. Thus the solubility limit of Co in $\text{Sr}_2\text{Ir}_{1-x}\text{Co}_x\text{O}_4$ is actually below 0.3.

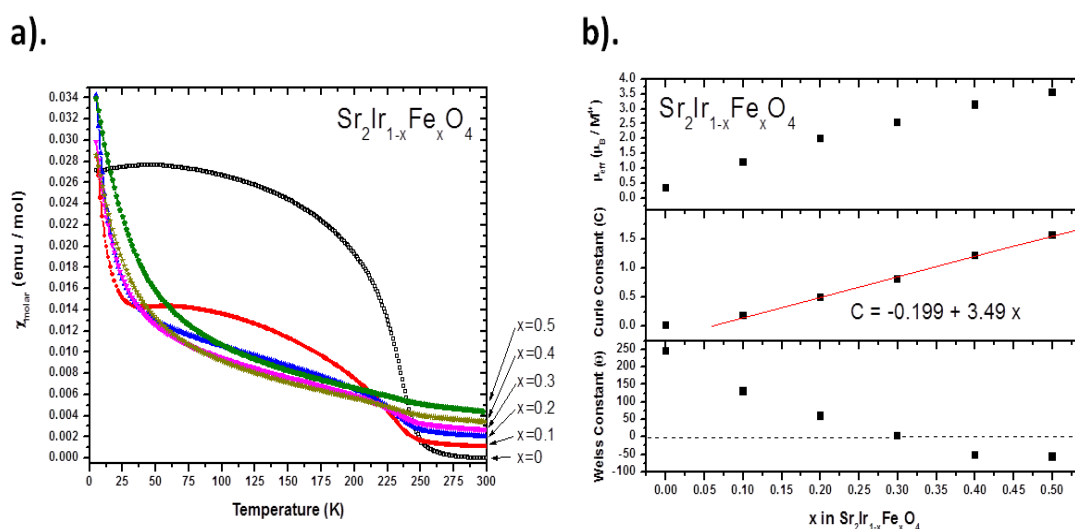


Figure 4.7. Magnetic susceptibility (a) evolution in temperature from 5 to 300 K of $\text{Sr}_2\text{Ir}_{1-x}\text{Fe}_x\text{O}_4$ (x up to 0.5) and refined values for Weiss constant, Curie Constant and effective moment (b) for the same compositions.

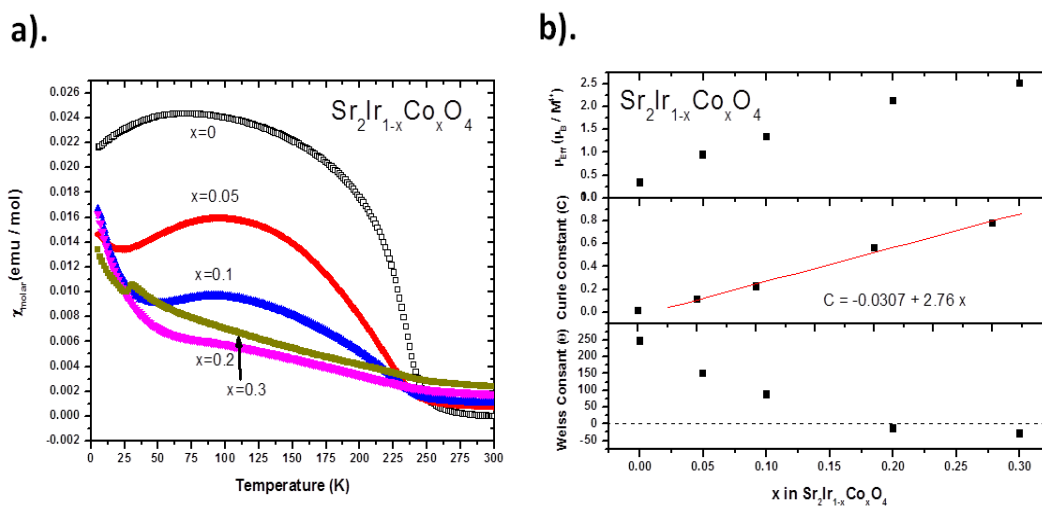


Figure 4.8. Magnetic susceptibility (a) evolution in temperature from 5 to 300 K of $\text{Sr}_2\text{Ir}_{1-x}\text{Co}_x\text{O}_4$ (x up to 0.3) and refined values for Weiss constant, Curie Constant and effective moment (b) for the same compositions. Note that the weak presence of Co_3O_4 for the composition $\text{Sr}_2\text{Ir}_{0.7}\text{Co}_{0.3}\text{O}_4$ was not detected by XRD.

The effective moments for $\text{Sr}_2\text{Ir}_{1-x}\text{M}_x\text{O}_4$ compositions ($x = 0.1 - 0.5$ for $\text{M} = \text{Fe}$ and $x = 0.1 - 0.3$ for $\text{M} = \text{Co}$) were determined by fitting with the Curie-Weiss law, $\chi = C / (T - \theta)$, from 265 - 325 K. Figures 4.7b and 4.8b plot the evolution of the effective moment as well as Curie and Weiss constants with substitution. For $\text{Sr}_2\text{Ir}_{1-x}\text{Fe}_x\text{O}_4$ there is an increase in the observed effective moment upon substitution, in agreement with the increase in unpaired electrons for Fe^{4+} . Similar to the study of $\text{Sr}_2\text{Ir}_{1-x}\text{Ru}_x\text{O}_4$ [16], we can assume a linear increase in Curie constant with Fe substitution; thus, the magnetic moment for Sr_2FeO_4 is estimated to be $5.15\mu_B$. This agrees well with the estimated spin only moment for a high spin (HS) d^4 cation in octahedral coordination ($4.89\mu_B$) and the reported moment for Sr_2FeO_4 ($5.6\mu_B$) [29]. It is also noted that there is a transition from positive to negative Weiss constant

for $\text{Sr}_2\text{Ir}_{1-x}\text{Fe}_x\text{O}_4$ above $x = 0.3$ indicating a transition to antiferromagnetism; Sr_2FeO_4 has an antiferromagnetic ground state with $T_N = 60$ K [29]. For $\text{Sr}_2\text{Ir}_{1-x}\text{Co}_x\text{O}_4$ compositions, a similar increase in the effective moment is observed. Sr_2CoO_4 has been stabilized using high pressure and is reported to possess Co^{4+} in the intermediate spin (IS) state [35]. Extrapolating the Curie constants to full Co substitution predicts an effective moment of about $4.69\mu_B$ for Sr_2CoO_4 which falls in between the values expected for a Co^{4+} IS state ($3.87\mu_B$) and HS state ($5.92\mu_B$).

4.3.3 Conclusion

A complete solid solution $\text{Sr}_2\text{Ir}_{1-x}\text{Ti}_x\text{O}_4$ was synthesized and characterized. The c parameter is found to decrease from the Ir to Ti end member. The a parameter initially increases then decreases to the a of Sr_2TiO_4 highlighting the opposing effects of decreasing octahedral tilting and decreasing octahedral M-O distance. The magnetic measurements reveal a decrease in the low temperature susceptibility and observed magnetic moment per metal ion as Ti content is increased and also support the idea that approximately midway through the solid solution paramagnetic interactions between Ir^{4+} ions become significant. Resistivity measurements evidence a semiconducting behavior in the whole range of the solid solution which is logical regarding the behavior of both Sr_2IrO_4 and Sr_2TiO_4 .

The Ti substitution was extended to the cases of Fe and Co as the Sr_2FeO_4 and Sr_2CoO_4 structure is similar to Sr_2TiO_4 . However, the solid

solutions are not complete, but limited here: up to $x = 0.4$ for Fe and less than $x = 0.3$ for Co. The evolution of the c -axis cell parameter in these two cases seems to follow the same trend as in the complete solid solution $\text{Sr}_2\text{Ir}_{1-x}\text{Ti}_x\text{O}_4$. To further substitute the Ir site by Fe or Co, the synthesis method needs to be however optimized: a high-pressure technique, required for the synthesis of the end members Sr_2FeO_4 and Sr_2CoO_4 , should allow for the investigation of complete solid solutions. The effective paramagnetic moment increases as Ir is replaced with either Fe or Co, as expected based on previous reports of Sr_2FeO_4 and Sr_2CoO_4 .

4.3.4 Experimental

Polycrystalline samples were prepared by conventional solid-state method using strontium carbonate SrCO_3 (Alfa 99.9%, iridium oxide IrO_2 (obtained by heating hydrated iridium chloride $\text{IrCl}_3 \cdot x\text{H}_2\text{O}$ (JMC 99.9%) two times for 12 h at 700 °C under air) with either titanium oxide TiO_2 (JMC 99.99%), iron oxide Fe_2O_3 (Alfa 99.99%) or cobalt oxide Co_3O_4 (Alfa 99.7%). SrCO_3 was dried overnight at 120 °C before use to avoid moisture contamination. Precursors were mixed thoroughly in the stoichiometric proportions, pelletized, and heated in air on a platinum tray in an alumina crucible. Typical heating treatments were 12 h at 1050 °C with heating and cooling rates set to +5 and -5 °C/min respectively.

Each powder sample was firstly characterized by XRD using a Rigaku Miniflex II diffractometer for the 2θ range from 10 to 80 °. Copper $K\alpha$

radiation was selected with a graphite monochromated diffracted beam. Room temperature cell parameters were refined using GSAS and Fullprof softwares [36–38]. Magnetic and electronic properties were carried out using a Quantum Design Physical Properties Measurement System (PPMS). Magnetic susceptibility measurements were done on encapsulated powder samples in a magnetic field of 1 Tesla, from 5 to 300 - 325 K (zero-field-cooled). Magnetization versus magnetic field data was collected at 5 K from 0 - 5 Tesla. Samples were reground, pelleted, and sintered for an additional 12 h in order to perform four-probe resistivity measurements from 5 to 300 K.

4.4 Investigation of the $\text{Sr}_2\text{Ti}_{1-x}\text{Rh}_x\text{O}_4$ solid solution.

4.4.1 Introduction

Neutron diffraction studies by Subramanian et al. have shown that similar to Sr_2IrO_4 , Sr_2RhO_4 crystallizes in a non-ideal K_2NiF_4 -type structure with Rh^{4+} ions in octahedral coordination and the RhO_6 octahedra rotated about the c-axis [15]. In Sr_2RhO_4 , the rotation of the octahedra about the c-axis is about 9.7° which is slightly less than the octahedral rotation in Sr_2IrO_4 of about 11° . The structural effects of this rotation are observed in the neutron diffraction studies where superlattice peaks confirm an expansion of the unit cell and overall change in space group from $I4/mmm$ to $I4_1/acd$. Similar to Sr_2IrO_4 , the tetragonal unit cell dimensions are $\sqrt{2}a_1 \times 2c_1$ with a_1 and c_1 representing the cell parameters for the ideal $I4/mmm$ unit cell. Structural data comparing these two compounds by Subramanian et al. is summarized in table 4.2 [15].

Compound	Space Group	<i>a</i> cell parameter (Å)	<i>c</i> cell parameter (Å)	MO_6 Rotation Angle
Sr_2IrO_4	$I4_1/acd$	5.4979(2)	25.798(1)	11°
Sr_2RhO_4	$I4_1/acd$	5.4531(1)	25.7548(7)	9.7°

Table 4.2. Structural data at 300 K comparing Sr_2IrO_4 and Sr_2RhO_4 . Adapted from [15].

Magnetically Sr_2RhO_4 does not show the ferromagnetic-like ordering that is observed in Sr_2IrO_4 . However, possible low temperature short range antiferromagnetic ordering in the composition has been reported [39]. Electrically, Sr_2RhO_4 shows metallic conductivity below 150 K unlike Sr_2IrO_4 which has been described as a Mott insulator [17,39].

Thus given the close similarity in structure to Sr_2IrO_4 and successful substitution of Ti for Ir in the complete $\text{Sr}_2\text{Ir}_{1-x}\text{Ti}_x\text{O}_4$ solid solution, it is worthwhile to investigate structure-property relationships in possible $\text{Sr}_2\text{Ti}_{1-x}\text{Rh}_x\text{O}_4$ phases. Structural, magnetic and electrical data are presented and discussed.

4.4.2 Results and Discussion

XRD patterns of the compositions synthesized show that the solubility limit for Rh in $\text{Sr}_2\text{Ti}_{1-x}\text{Rh}_x\text{O}_4$ was found to be $x = 0.6$. Figure 4.9 shows the XRD patterns of the single phase compositions. Significant changes in the XRD patterns can be seen by examining the $40^\circ - 45^\circ$ and $52^\circ - 57^\circ$ 2θ range. However, due to differences in scattering power between Ti and Rh, the XRD data was refined and unit cell parameters for the tetragonal cells were determined for more clarity on structural changes. These cell parameters are plotted in figure 4.10 where an overall increase in the c parameter is observed from $x = 0$ to $x = 0.6$ while the a parameter is found to remain relatively constant. As the figure shows using the red dotted lines, two regimes are

observed for the a parameter. The a cell parameter can be seen to be slightly increasing below $x = 0.2$ but then stops increasing after this composition. A similar change around the $x = 0.2$ composition can be seen in the c parameter behavior where the slope of increase clearly changes. In examining the c/a ratio, a change in slope is also evident around the $x = 0.2$ composition as shown in figure 4.11, where the c/a ratio is decreasing below $x = 0.2$ but then begins to increase for $x > 0.2$ compositions. Given the relatively similar sizes of Ti^{4+} (0.6 Å in 6-fold coordination) and Rh^{4+} (0.605 Å in 6-fold coordination), it may be expected that little to no change is observed in the a parameter with Rh substitution [31]. This could be argued to be the case looking at the a parameter scale in figure 4.10 where all the changes in the a cell parameter are within 0.02 Å. Nevertheless, it is important to remember that structural changes occurring with Rh substitution include a rotation of the octahedra which will result in a decrease in the a parameter. It could then also be argued that the effect of these rotations on the a parameter may be involved in the change observed at $x = 0.2$ shown in figure 4.10.

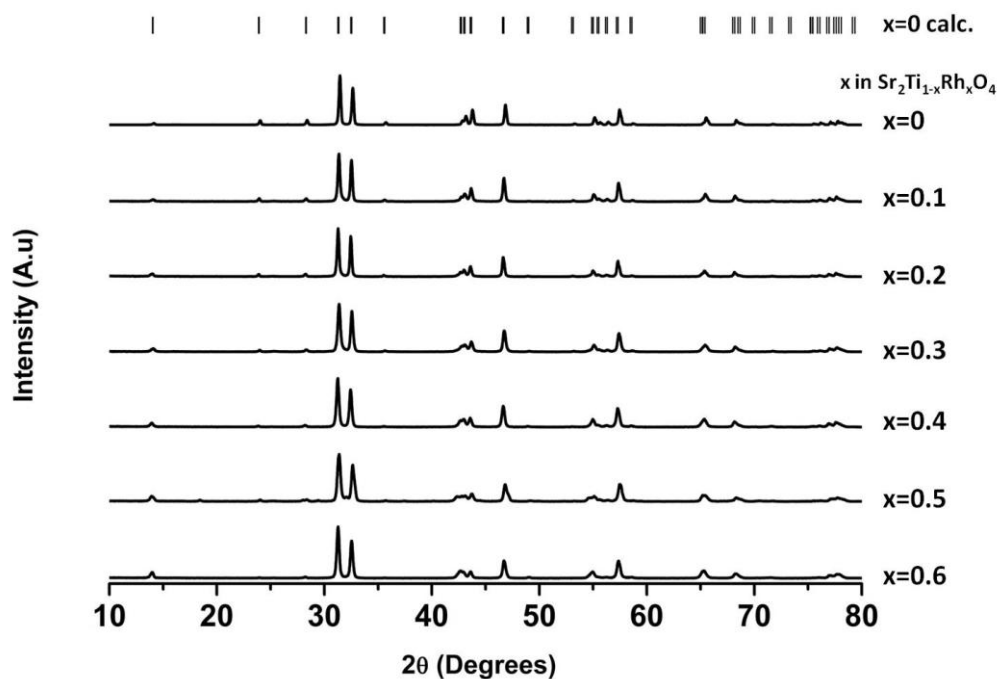


Figure 4.9. XRD patterns of single phase $\text{Sr}_2\text{Ti}_{1-x}\text{Rh}_x\text{O}_4$ ($x \leq 0.6$) compositions.

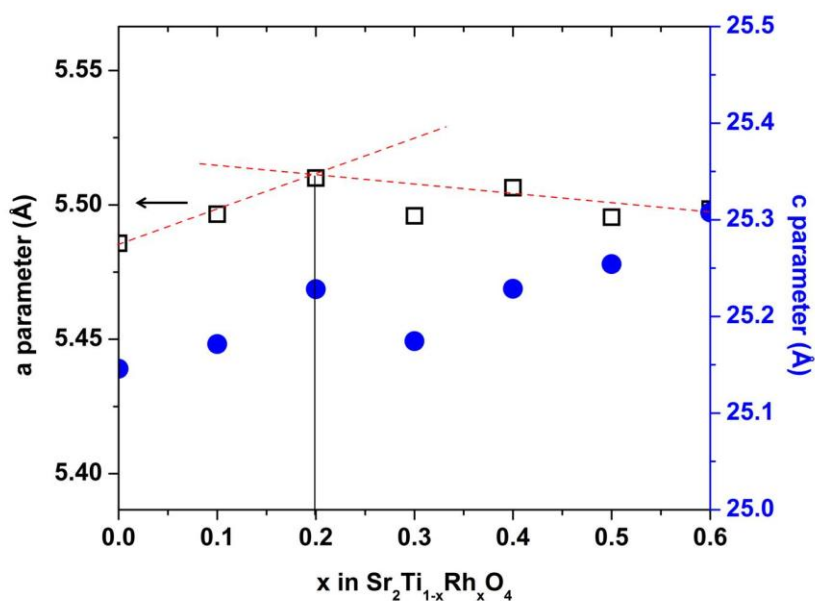


Figure 4.10. Refined lattice parameters of the $\text{Sr}_2\text{Ti}_{1-x}\text{Rh}_x\text{O}_4$ phases showing relatively little change in the a cell parameter with Rh substitution, however, a change from a positive to negative slope at the $x = 0.2$ composition can be observed as shown by the dashed line. This is likely related to octahedral

rotation occurring with Rh substitution. The c cell parameter shows an increase with substitution.

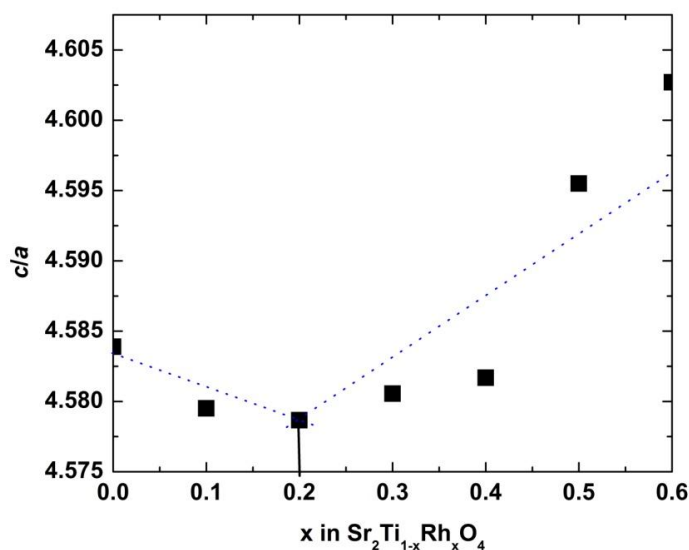


Figure 4.11. The c/a ratio of the refined $\text{Sr}_2\text{Ti}_{1-x}\text{Rh}_x\text{O}_4$ phases. A clear change in slope is observed at the $x = 0.2$ composition which is likely related to octahedral rotation occurring.

Figure 4.12 shows the magnetic susceptibility data with temperature. Given that Ti^{4+} is a d^0 cation and Rh^{4+} is a d^5 (low spin $t_{2g}^5e_g^0$) cation, the substitution of Rh was expected to lead to an increase in susceptibility and this is clearly observed in figure 4.12. However, only paramagnetic behavior was observed and no low temperature antiferromagnetic interactions are clearly evident. Figure 4.13 depicts the electrical resistivity with temperature. Sr_2TiO_4 was found to be insulating and gave no reading with four-probe measurement. However, as figure 4.13 shows, with $x \geq 0.2$ compositions, semiconducting behavior is observed. It is expected that if compositions with higher Rh content can be prepared, a transition from semiconducting to metallic conductivity may be observed as Sr_2RhO_4 shows metallic conductivity.

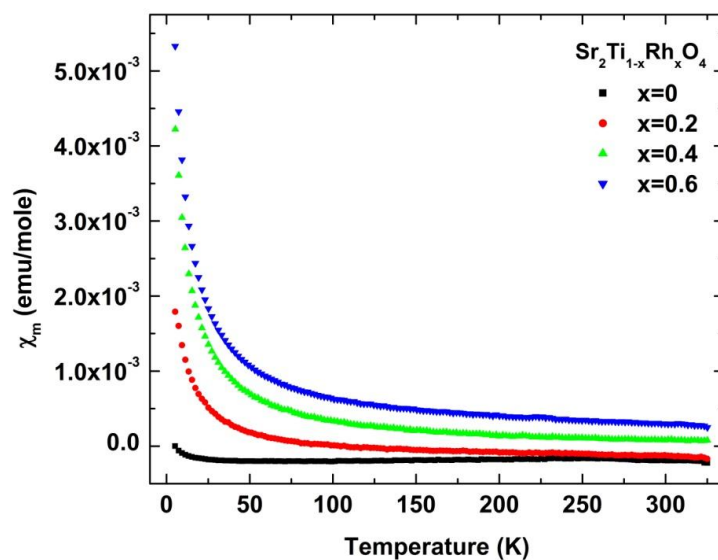


Figure 4.12. The magnetic susceptibility evolution with temperature of the $\text{Sr}_2\text{Ti}_{1-x}\text{Rh}_x\text{O}_4$ phases. All phases show paramagnetic behavior however, high susceptibilities are observed with increasing Rh content.

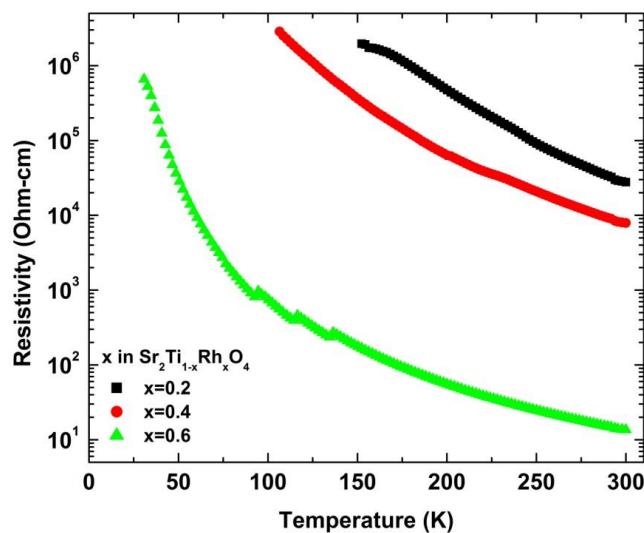


Figure 4.13. The electrical resistivity evolution with temperature of the $\text{Sr}_2\text{Ti}_{1-x}\text{Rh}_x\text{O}_4$ phases. All phases show semiconducting behavior however, a transition to metallic conductivity is expected if higher Rh content can be successfully substituted as Sr_2RhO_4 has been found to be metallic [39].

4.4.3 Conclusion

Following the success substituting Ti for Ir in the complete $\text{Sr}_2\text{Ir}_{1-x}\text{Ti}_x\text{O}_4$ solid solution, Rh substitution for Ti was attempted. Single phase compositions of $x \leq 0.6$ for $\text{Sr}_2\text{Ti}_{1-x}\text{Rh}_x\text{O}_4$ were synthesized and characterized. Synthesis under oxidizing conditions for higher Rh content compositions has of the writing of this thesis proved unsuccessful, but is worth further investigation. The a parameter is shown to change slightly with Rh substitution for the phases synthesized, however a notable change at $x = 0.2$ is observed. This is likely instigated by the effect of octahedral rotations resulting from Rh substitution. A change at the $x = 0.2$ composition is also observed in the c parameter and c/a ratio behavior. Magnetically, the presence of an unpaired electron in Rh^{4+} leads to higher magnetic susceptibility measurements with Rh substitution; however, only paramagnetic behavior is observed for all synthesized compositions. Electrically, $x \geq 0.2$ compositions show semiconducting behavior but a semiconducting to metallic transition may be observed if synthesis of single phase $x > 0.6$ compositions is successful.

4.4.4 Experimental

Polycrystalline samples were prepared by conventional solid-state method using strontium carbonate SrCO_3 (Alfa 99.9%) rhodium oxide Rh_2O_3 (obtained by heating RhI_3 for 10 h at 1073 K in air), and titanium oxide TiO_2 (JMC 99.99%). The precursors were mixed thoroughly in the stoichiometric

proportions, pelletized, and heated in air on a platinum tray in an alumina crucible. Typical heating treatments were 12 h at 1050 °C with heating and cooling rates set to +5 and -5 °C/min respectively.

Each powder sample was firstly characterized by XRD using a Rigaku Miniflex II diffractometer for the 2θ range from 10 to 80 °. Copper $K\alpha$ radiation was selected with a graphite monochromated diffracted beam. Room temperature cell parameters were refined using GSAS software [36,37]. Magnetic and electronic properties were carried out using a Quantum Design Physical Properties Measurement System (PPMS). Magnetic susceptibility measurements were done on encapsulated powder samples in a magnetic field of 1 Tesla, from 5 to 300 K (zero-field-cooled). Samples were reground, pelletized, and sintered for an additional 12 h in order to perform four-probe resistivity measurements from 5 to 300 K.

4.5 References

- [1] L.B. Hunt, *Platinum Met. Rev.* 31 (1987) 32–41.
- [2] S. Tennant, *Phil. Trans.* 94 (1804) 411–418.
- [3] O. Feussner, *Elektrotech. Zeits.* 54 (1933) 155–156.
- [4] J.R. Handley, *Platinum Met. Rev.* 30 (1986) 12–13.
- [5] H. Inouye, *Platinum Met. Rev.* 23 (1979) 100–108.
- [6] W.D. Komer, D.J. Machin, *J. Less Comm. Met.* 61 (1978) 91–105.
- [7] F. Rodi, Eberhardt-Karls-Universitat, 1963.
- [8] R.J. Bouchard, J.L. Gillson, *Mater. Res. Bull.* 6 (1971) 669–679.
- [9] R.D. Roof, Los Alamos National Laboratory.
- [10] A.W. Sleight, *Mater. Res. Bull.* 6 (1971) 775–780.
- [11] D. Balz, K. Plieth, *Z. Elektrochem.* 59 (1955) 545–551.
- [12] R. Heap, M.S. Islam, P.R. Slater, *Dalton T.* (2005) 460.
- [13] J.G. Bednorz, K.A. Müller, *Z. Phys. B: Condens. Matter* 64 (1986) 189–193.
- [14] M.K. Crawford, M.A. Subramanian, R.L. Harlow, J.A. Fernandez-Baca, Z.R. Wang, D.C. Johnston, *Phys. Rev. B* 49 (1994) 9198–9201.
- [15] M.A. Subramanian, M.K. Crawford, R.L. Harlow, T. Ami, J.A. Fernandez-Baca, Z.R. Wang, D.C. Johnston, *Physica C* 235–240 (1994) 743–744.
- [16] R.J. Cava, B. Batlogg, K. Kiyono, H. Takagi, J.J. Krajewski, W.F. Peck, L.W. Rupp, C.H. Chen, *Phys. Rev. B* 49 (1994) 11890–11894.
- [17] F. Wang, T. Senthil, *Phys. Rev. Lett.* 106 (2011) 136402.
- [18] Y. Klein, I. Terasaki, *J. Phys.: Condens. Matter* 20 (2008) 295201.
- [19] C. Cosio-Castaneda, G. Tavizon, A. Baeza, P. de la Mora, R. Escudero, *J. Phys.: Condens. Matter* 19 (2007) 446210.
- [20] G. Cao, J. Bolivar, S. McCall, J.E. Crow, R.P. Guertin, *Physica B: Condens. Matter* 57 (1998) R11039.
- [21] O.B. Korneta, T. Qi, S. Chikara, S. Parkin, L.E. De Long, P. Schlottmann, G. Cao, *Phys. Rev. B* 82 (2010) 115117.
- [22] T.F. Qi, O.B. Korneta, S. Chikara, M. Ge, S. Parkin, L.E. De Long, P. Schlottmann, G. Cao, *J. Appl. Phys.* 109 (2011).
- [23] T. Shimura, Y. Inaguma, T. Nakamura, M. Itoh, Y. Morii, *Phys. Rev. B* 52 (1995) 9143–9146.
- [24] J.J. Randall, L. Katz, R. Ward, *J. Am. Chem. Soc.* 79 (1957) 266–267.
- [25] Q. Huang, J.L. Soubeyroux, O. Chmaissem, I.N. Sora, A. Santoro, R.J. Cava, J.J. Krajewski, W.F. Peck, *J. Solid State Chem.* 112 (1994) 355–361.
- [26] M.E. Leonowicz, K.R. Poeppelmeier, J.M. Longo, *J. Solid State Chem.* 59 (1985) 71–80.
- [27] J. Takahashi, N. Kamegashira, *Mater. Res. Bull.* 28 (1993) 565–573.
- [28] K. Lukaszewicz, *Rocz. Chem.* 33 (1959) 239.
- [29] S.E. Dann, M.T. Weller, D.B. Currie, *J. Solid State Chem.* 92 (1991) 237–240.
- [30] J. Matsuno, Y. Okimoto, Z. Fang, X.Z. Yu, Y. Matsui, N. Nagaosa, M. Kawasaki, Y. Tokura, *Phys. Rev. Lett.* 93 (2004) 167202.
- [31] R.D. Shannon, *Acta Cryst.* A32 (1976) 757 – 767.

- [32] B.J. Kim, H. Ohsumi, T. Komesu, S. Sakai, T. Morita, H. Takagi, T. Arima, *Science* 323 (2009) 1329–1332.
- [33] K. Miwa, I. Kagomiya, H. Ohsato, H. Sakai, Y. Maeda, *J. Eur. Ceram. Soc.* 27 (2007) 4287–4290.
- [34] S.E. Dann, M.T. Weller, D.B. Currie, M.F. Thomas, A.D. Al-Rawwas, *J. Mater. Chem.* 3 (1993) 1231.
- [35] X.L. Wang, E. Takayama-Muromachi, *Phys. Rev. B* 72 (2005) 064401.
- [36] A.C. Larson, R.B. Von Dreele, Los Alamos National Laboratory Report LAUR (2004) 86–748.
- [37] B.H. Toby, *J. Appl. Cryst.* 34 (2001) 210–213.
- [38] J. Rodriguez-Carvajal, *XV IUCr Congress*, 1990.
- [39] T. Shimura, M. Itoh, T. Nakamura, *J. Solid State Chem.* 98 (1992) 198–200.

CHAPTER 5

Further Details on Experimental Methods.

5.1 Introduction

One of the primary driving factors of solid state chemistry research are the experimental methods of sample preparation and characterization available to be employed. With continuous developments in technology, the extent of detail acquirable, coupled with dramatic improvements in efficiency have been achieved. Most scientists would argue that there is a direct correlation between the quality of your data and the relevance of your data. As such, the following sections give further details on experimental techniques, measurements and instruments referred to in the investigations described in this thesis.

5.2 X-ray Diffraction

In investigating structure-property relationships, structure determination often comes first and the most employed technique to garner structural data is X-ray diffraction (XRD). XRD allows for determination of crystal structure information from unit cell parameters to atomic positions and also on the morphology of materials including the quantity and location of impurities and crystallite size.

In principle, X-ray radiation diffracted off a sample is defined by Bragg's law:

$$n\lambda = 2d\sin\theta$$

where n is an integer, λ is the wavelength of the X-ray radiation, d is the interplanar spacing and θ is the angle of incidence of the X-ray beam. At most conditions, the scattered X-rays from the sample cancel each other during destructive interference. However, at specific conditions in which Bragg's law is fulfilled, constructive interference of diffracted beams occurs as shown in figure 5.1. A particular material will diffract X-rays from its characteristic planes leading to unique intensities for specific 2θ values.

From Bragg's law, if θ and λ are known, the d -spacing (distance between diffracting lattice planes) can be calculated. This then allows for calculation of further structural data including unit cell parameters and unit cell angles (α , β , γ). Investigations in this thesis have included XRD on both powder samples and single crystal samples, with specific instrumentation used in each case.

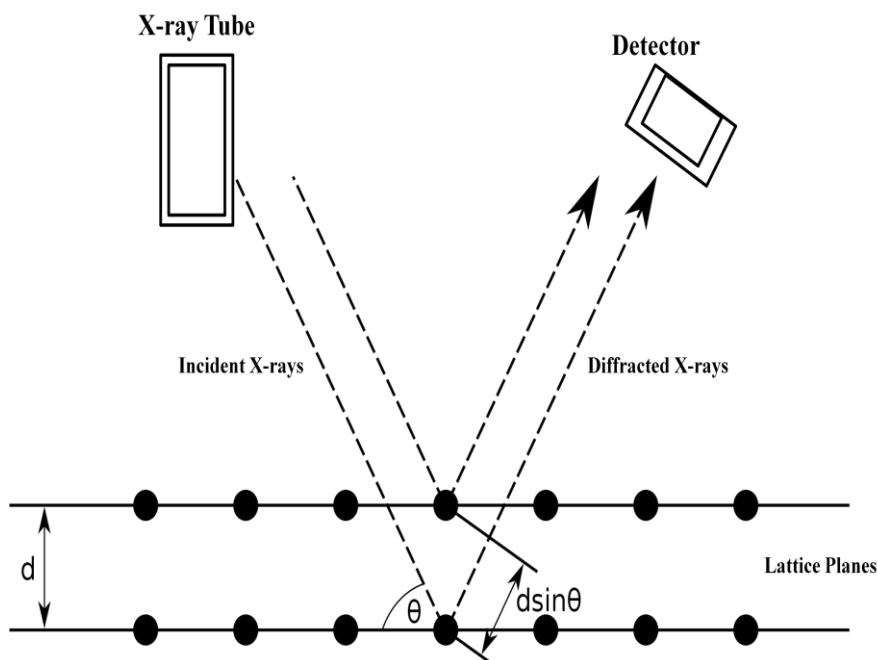


Figure 5.1. Bragg's law relationship depicted by identical incident X-ray beams of equal wavelength being scattered by atoms on different planes of crystalline material. The lower beam travels an extra $2d\sin\theta$ distance with constructive interference resulting when this extra distance equals $n\lambda$. Image is adapted from [1].

5.2.1 Powder X-ray Diffraction – Rigaku Miniflex II Diffractometer

Powder XRD is mainly used for phase identification. Powder samples can be assumed to contain an infinite number of randomly oriented miniscule crystals representing all the planes of the material. Most X-ray diffractometers are composed of three main components. An X-ray source, a sample holder and an X-ray detector [2]. An external chiller system is often also present to prevent the X-ray source from overheating. At the X-ray source, electron beams from an electron source are accelerated onto a metal target leading to core 1s electrons of the metal target being ejected. In order to fill these

vacancies at the 1s level, outer level electrons of the metal target fall into these vacancies emitting radiation in the process called K radiation that lies within the X-ray spectrum. This process is depicted in figure 5.2 This allows for the excited atoms of the metal target to return to ground state. Most of the powder XRD patterns collected in this thesis were done using a Rigaku Miniflex II bench top diffractometer pictured in figure 5.3

With the Miniflex II instrument, a beam of electrons is accelerated from a heated tungsten filament toward an anode through a large voltage. The electron beam bombards a copper metal target at the anode. The resulting Cu $K\alpha$ and Cu $K\beta$ X-ray radiation are directed out a Be window towards the sample. The particular Miniflex II instrument used has a graphite monochromator that allows focus on Cu $K\alpha$ radiation. Other diffractometers sometimes use a Ni filter to absorb the $K\beta$ peaks which tend to be undesirable.

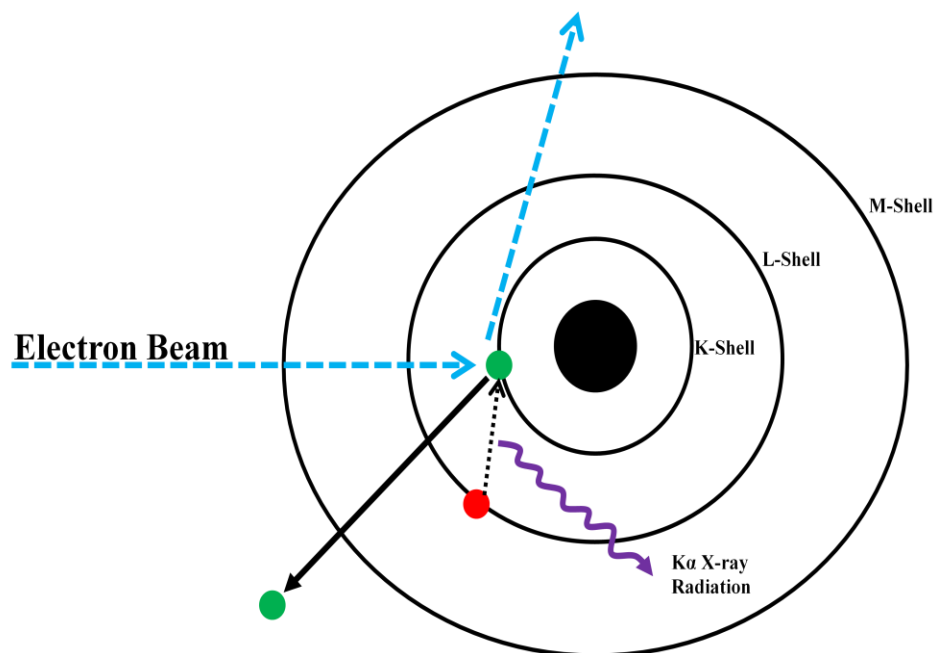


Figure 5.2. Origin of $K\alpha$ radiation. The electron beam excites the atom leading to a core electron (green) being emitted. An electron on the L-shell (red) drops to the K-shell to fill the vacancy and return the atom to the ground state. As the L-shell electron drops into the lower energy K-shell, $K\alpha$ radiation is emitted.

The Miniflex II operates at a fixed tube voltage of 30 kV and a fixed tube output current of 15 mA producing an average Cu $K\alpha$ X-ray radiation with a 1.5418 Å wavelength [3]. Thus, the instrument functions by fixing λ and varying θ . A six sample changer accessory which rotates during operation (pictured in figure 5.3c) was used for powder XRD investigations. This allows multiple samples to be investigated rapidly for phase identification (with 2θ varied at $> 2^\circ/\text{min}$), or more slowly during a step-scan (with a step size and rate of $\sim 0.02^\circ/\text{sec}$ per step) allowing for maximum intensities and highly accurate d-spacings to be collected for analysis of cell parameters and structural refinements.



Figure 5.3. Rigaku Miniflex II diffractometer system. The Haskris water recirculator (a) allows for the instrument (b) to function without the X-ray tube shown in (c) overheating.

5.2.2 Single Crystal X-ray Diffraction – Bruker Smart Apex II

For more detailed crystal structure information single crystal XRD is essential. This detailed information includes unit cell parameters, space group symmetry, atomic position parameters, atomic occupancies, bond angles and bond lengths. Small crystals (in the mm range) are usually measured in a four circle goniometer diffractometer that allows for thousands of reflections to be collected [4].

Single crystal X-ray diffraction data described in this thesis were collected using a Bruker SMART APEX II CCD system and an Oxford Cryostream Cooler at 173 K and 233 K. A fine focus tube was used with an anode power of 50 kV at 30 mA, a crystal to plate distance of 6.0 cm, 512 x 512 pixels/frame, beam center (256.52, 253.16), ϕ/ω scan with step of 0.30° , exposure/frame of 10.0s/frame, and SAINT integration.

Software was then used to analyze the data. An absorption correction was applied by the SADABS program. Crystal structures were solved by

direct methods and refined with full-matrix least-squares method using the SHELXTL software package [5]. Higher angle measurements were carried out using an Oxford-Diffraction Xcalibre2 CCD diffractometer equipped with a Cryojet cooling device.

5.3 Low Temperature Magnetometry and Resistivity – Quantum Design PPMS

Both low temperature magnetic and electrical resistivity measurements were performed using a Physical Property Measurement System (PPMS) by Quantum Design. The instrument pictured in figure 5.4 is essentially a workstation operating on a multisystem platform allowing for several measurements at a wide range of temperatures (3 K – 320 K) to be performed.

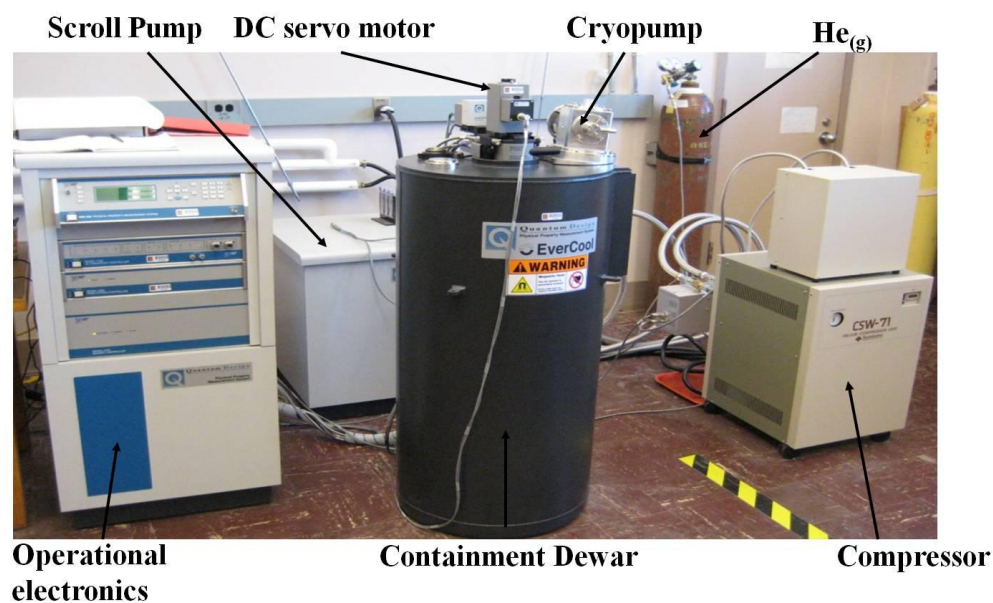


Figure 5.4. The Physical Property Measurement System by Quantum Design. A multiplatform workstation allowing for low temperature magnetometry and electrical resistivity measurements.

As seen in figure 5.4, the system uses compressed He to achieve the low temperatures. The particular system used in this work uses an Evercool liquid He recycling system allowing for recompression of lost He during venting back to liquid He for temperature control. External He can then be

supplied as He gas eliminating the need for liquid He transfers that are costly and time consuming.

5.3.1 Low Temperature Magnetometry

The AC/DC Magnetometry System (ACMS) option for the PPMS allows for AC susceptibility and DC magnetization measurements. The ACMS coil set is inserted into the main dewar and connected to the main instrument via a 12-pin connector. This is depicted in figure 5.5. DC magnetization was primarily used for investigations in this thesis. This involves a magnetic field being applied to a sample to induce a magnetization within the sample which is then detected as an induced voltage by the system. The voltage amplitude is dependent on the magnetic moment and the vertical movement of the sample.

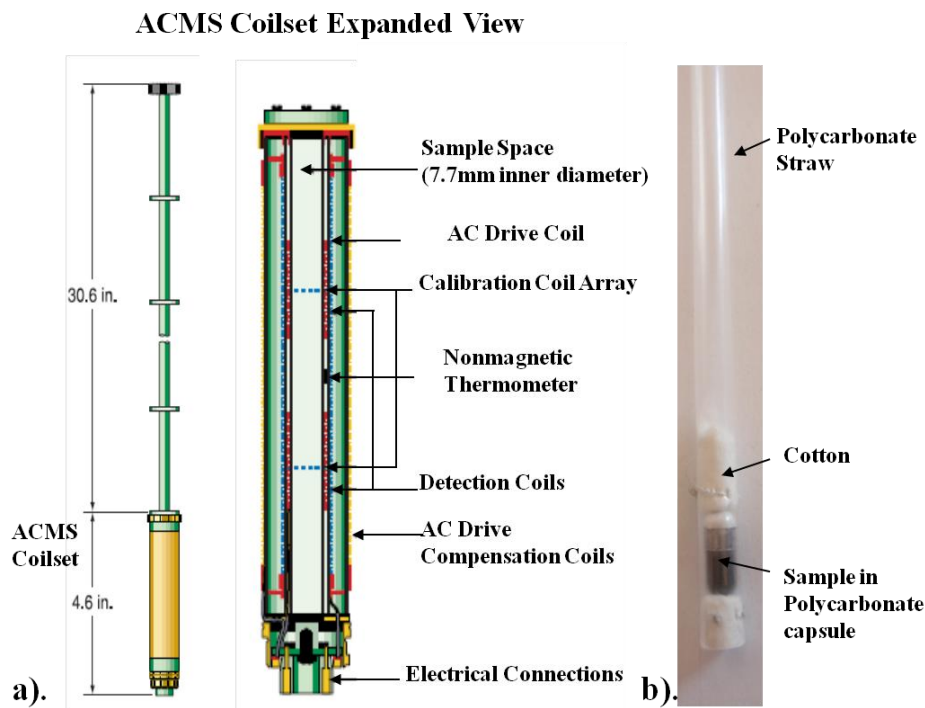


Figure 5.5. A schematic showing the dimensions of the ACMS coil set and tube assemblage (a) [6]. (b) shows a typical powder sample packed in a polycarbonate capsule which is then packed into a polycarbonate straw using cotton.

For the applied field, a strength of up to 7 Tesla is possible from the instrument's superconducting magnet, however, most measurements used an applied field of 0.5 – 1 Tesla. Samples are encapsulated in polycarbonate capsules packed into a polycarbonate straw using cotton. Sample centering and location is also necessary for accurate magnetization measurements.

5.3.2 Low Temperature Electrical Resistivity

Electrical resistivity is an often measured bulk property of oxide materials. Two main ways of measuring electrical resistivity are the two and four-probe method. Two probe measurements include the contact resistance of

the leads and is thus suitable for samples with resistivities above 10 Ohm-cm. With four-probe measurements, lead and contact resistance is excluded and is thus a more accurate electrical resistivity measurement often employed for samples with electrical resistivities below 10 Ohm-cm, where the contact resistance could significantly affect the measurement of the electrical resistivity of the sample [4].

The PPMS allows for four-probe DC resistivity measurements using the resistivity puck pictured in figure 5.6. As the picture shows three bar shaped samples can be measured independently and simultaneously. Four copper contact wires are attached to the bar sample of known dimensions by conducting silver epoxy. The known sample geometry is inputted in the PPMS interface software to calculate resistivity from obtained resistance data. Temperatures from 3 K – 320 K can be measured, with very low temperatures being especially useful for investigating superconducting materials.

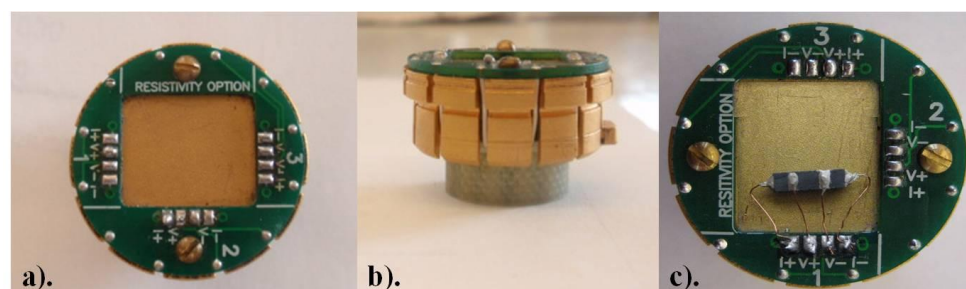


Figure 5.6. The resistivity puck allowing low temperature electrical resistivity measurements of the samples simultaneously numbered on the puck circuit board (a). The puck is connected to the instrument via a 12-pin connection at the base of the puck (b). The samples are measured via the four-probe method (c).

5.4 High Temperature Seebeck and Resistivity – ZEM-3 Thermoanalyzer

Similar to electrical resistivity, the Seebeck coefficient or thermoelectric power is a bulk property of oxide materials. As discussed earlier, the Seebeck coefficient allows for determination of the majority carriers with a positive Seebeck coefficient indicating holes as the majority carrier in a p-type material, while a negative Seebeck coefficient indicates electrons as the majority carrier in an n-type material.

Both high temperature (35°C - 1100°C) Seebeck and four-probe measurements in this thesis were performed in an inert He atmosphere using an ULVAC-RIKO ZEM-3 Thermoanalyzer. This instrument is pictured in figure 5.7. An infra-red furnace (thermal chamber) surrounds the sample area. The sample is placed on spring loaded electrode blocks made of Ni which are tightened against the sample as shown in figure 5.7b. The electrode blocks allow for a thermal gradient across the sample to be created. Adjustable Platinum probes (a standard distance of 3 mm apart) measure the voltage across the sample as well as point temperatures. The voltage difference between the two probes (ΔV) as well as the point temperature difference (ΔT) allows for the measurement of the Seebeck coefficient ($\Delta V/\Delta T$) at a particular furnace temperature (measured by an external thermocouple).

The four electrodes, the two Ni electrodes and the two Pt electrodes allow for simultaneous four-probe electrical resistivity at the high temperatures [7].

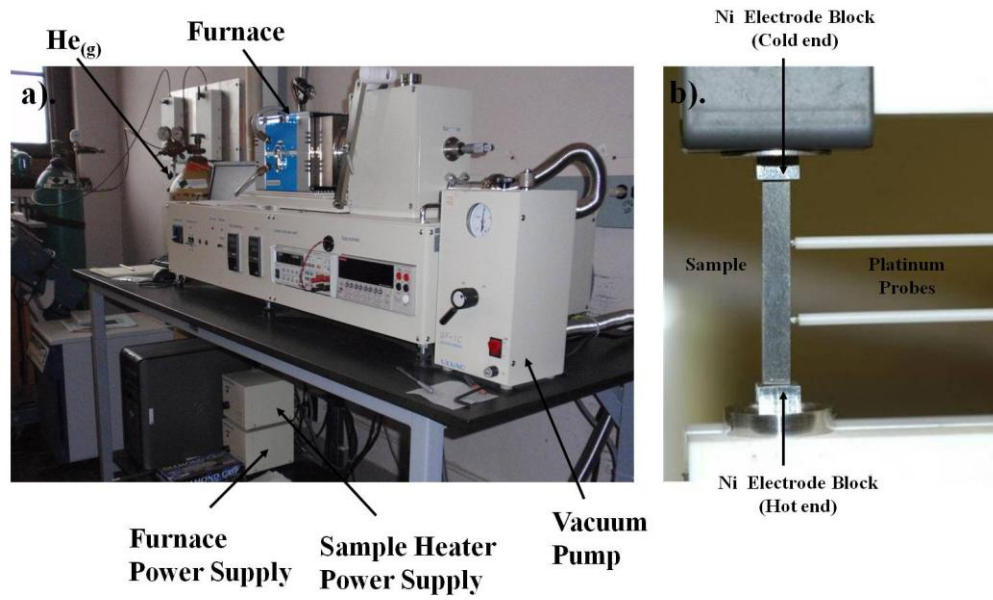


Figure 5.7. The ULVAC-RIKO ZEM-3 Thermoanalyzer set-up (a). Inside the furnace chamber the sample is held in place by Ni electrodes and Pt probes (b).

5.5 Thermal Diffusivity – Netzsch MicroFlash

In order to calculate the thermal conductivity, thermal diffusivity can be measured and used to determine the thermal conductivity based on the relationship,

$$k_T = C_p \cdot \alpha \cdot d$$

where C_p is the specific heat described in the next section, α is the thermal diffusivity and d is the sample bulk density. Thermal diffusivity measurements described in this thesis were measured using a Netzsch LFA 457 Micro Flash under flowing Nitrogen depicted in figure 5.8.

The instrument functions by heating the front side of the pellet with a short laser pulse from a Nd-YAG laser (with a maximum energy of 18.5 J and a pulse length of 0.5 ms). The temperature on the rear side (surface) of the pellet is then measured as a function of time by an infrared detector. The instrument allows for measurements up to approximately 1100°C and thermal diffusivities between 0.01 mm²/s to 1000 mm²/s.

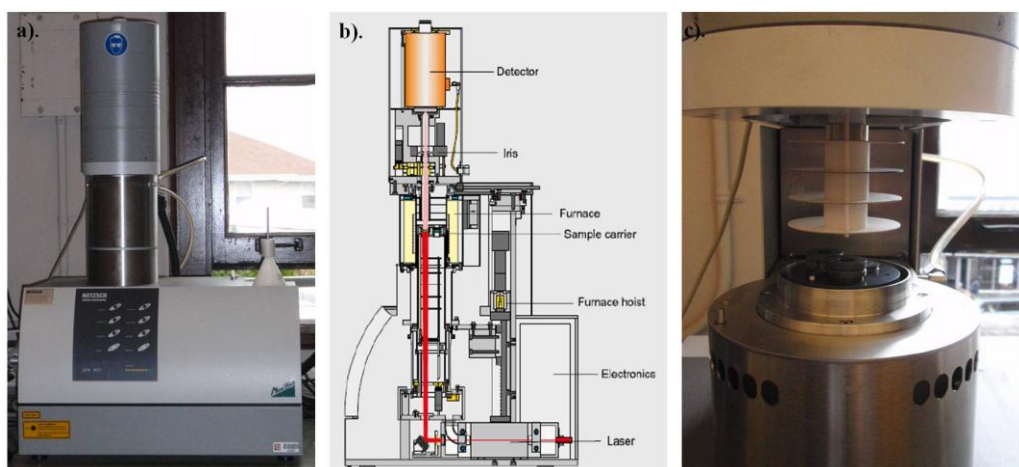


Figure 5.8. An external view of the The Netzsch Microflash (a) and schematic view of the instrument design from [8]. The sample carrier and infrared detector fins are shown in (c).

5.6 Specific Heat – Mettler Toledo Differential Scanning Calorimeter

Specific heat (C_p) measurements in this thesis were performed for calculation of thermal conductivity. A Mettler Toledo 821e Differential Scanning Calorimeter with an alumina (Sapphire) calibration standard under flowing Nitrogen was used. The instrument is pictured in figure 5.9 and was used in cooperation with STARe software package.

The instrument measures the difference in heat required to raise the temperature of the sample compared to the Sapphire reference. The two (sample and reference) are placed in two separate small pans on top of two separate heaters programmed similarly. The difference in heat required for the sample and reference allows for determination of the C_p of the sample [2].

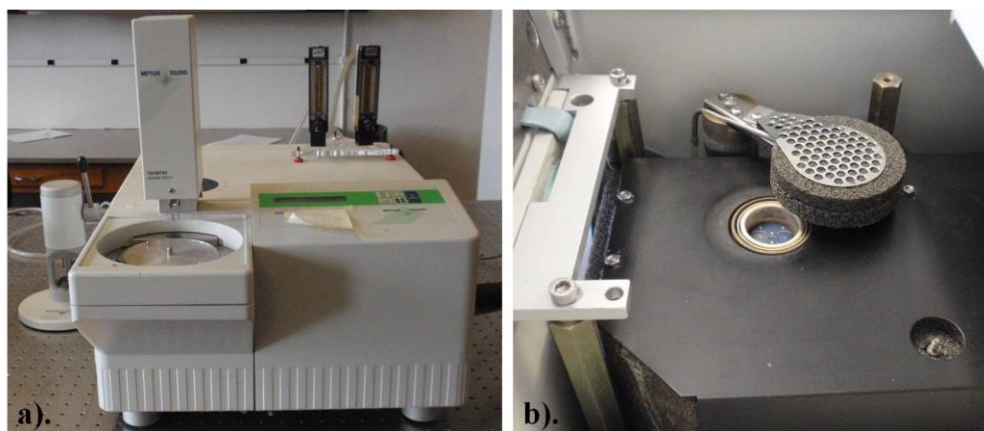


Figure 5.9. The Mettler Toledo DSC (a) with the sample and reference placed in pans that sit on two separate heater in the general furnace area (b).

5.7 References

- [1] Bragg's Law. en.wikipedia.org/wiki/Bragg's_law. Accessed May 2012.
- [2] T. Siritanon, Structure-Property Relationships in Oxides Containing Tellurium., Ph.D Thesis, Oregon State University, Corvallis, OR, 2011.
- [3] Rigaku Corporation. X-ray Diffractometer Miniflex II Instructional Manual. Second Edition. Rigaku Corporation (2006).
- [4] A.K. Cheetham, P. Day, Solid-State Chemistry: Techniques, Oxford University Press, 1987.
- [5] G.M. Sheldrick, SHELEXTL, Version 6.14, Bruker Analytical X-ray Instruments, Inc., Madison, WI. (2003).
- [6] Quantum Design, Physical Property Measurement System Hardware and Operations Manual, Second Edition. Quantum Design (1999).
- [7] ULVAC-RIKO, Inc. Model ZEM-3 Thermoanalyzer: Power Conversion Efficiency Measuring Instrument Instruction Manual.
- [8] LFA 457 MicroFlash® - Laser Flash Apparatus, for thermophysical properties - NETZSCH. <http://www.netzsch-thermal-analysis.com/us/products/detail/pid,26.html>. Accessed May 2012.

General Conclusions and Future Work

The work described in this thesis provides a good insight into the variety of oxides transition metals form. In particular oxides of 4d (Ru, Rh) and 5d (Ir) metals were investigated. The work also exemplifies the strong correlations between the structure and properties of these oxides with structure almost always dictating properties.

This was seen in investigating substitutional effects in hexagonal $\text{Pb}_3\text{Rh}_7\text{O}_{15}$. Despite $\text{Pb}_3\text{Mn}_7\text{O}_{15}$ being isostructural, low percentages of Mn for Rh influenced the $\text{Pb}_3\text{Rh}_7\text{O}_{15}$ properties greatly. The Verwey-type transition that manifests in a variety of physical properties particularly a rapid increase in electrical resistivity at ~ 185 K was found to be diminished by a 4% Mn substitution. The sensitivity of the charge-ordering transition was shown. The prominent magnetic transitions exhibited by $\text{Pb}_3\text{Mn}_7\text{O}_{15}$ were found to be diminished by a 57% Rh substitution. Significantly lower substitution levels were found with Bi for Pb in $\text{Pb}_3\text{Mn}_7\text{O}_{15}$ as compared to in $\text{Pb}_3\text{Rh}_7\text{O}_{15}$.

Structure-Property correlations were also exemplified by $\text{Sr}_{1-x}\text{M}_x\text{RuO}_3$ ($\text{M} = \text{K}, \text{Rb}, \text{Cs}$) and $\text{Sr}_{2-x}\text{La}_x\text{CoRuO}_6$ investigations where the versatility of the perovskite structure was tested. Only low substitutions levels were found possible for the alkali substitutions that decreased the ferromagnetic T_c of SrRuO_3 linked to the distortions resulting from the substitutions. With increasing La content in $\text{Sr}_{2-x}\text{La}_x\text{CoRuO}_6$, some ordering on the B-site resulted observed by a change in space group from $I2/c$ to $P2_1/n$ at $x = 0.5$.

$\text{Sr}_{1.1}\text{La}_{0.9}\text{CoRuO}_6$ was found to show the best thermoelectric performance that can likely be improved with sample processing.

The rutile compositions $(\text{RhV})_{1+x}\text{Ti}_{1-2x}\text{O}_6$ were found to be disordered which was surprising given the fixed valencies. This was a good example as to how crystal structures can defy predictions and alluded to the element of surprise and serendipity that is always possible in solid state chemistry research.

In the case of the $\text{Sr}_2\text{Ir}_{1-x}\text{M}_x\text{O}_4$ ($\text{M} = \text{Ti}, \text{Co}, \text{Fe}$) and $\text{Sr}_2\text{Ti}_{1-x}\text{Rh}_x\text{O}_4$ investigations, a complete solid solution was observed for Ti substitution for Ir with unit cell behavior that showed the contrasting effects of substituting with a smaller cation (Ti) yet decreasing the octahedral tilting found in Sr_2IrO_4 ($\sim 11^\circ$) to the lack of octahedral tilting in Sr_2TiO_4 . The Co and Fe substitutions were incomplete but did indicate similar loss in octahedral tilting with Co/Fe substitution. The $\text{Sr}_2\text{Ti}_{1-x}\text{Rh}_x\text{O}_4$ solid solution is also currently incomplete despite synthesis under oxidizing conditions for high Rh compositions. Nonetheless, the structural effects of octahedral tilting with greater Rh content were observed in the unit cell dimensions of the single phase compositions ($x \leq 0.6$). The Rh substitution also led to higher magnetic susceptibility and more conducting materials.

As a whole, these findings though interesting should not mark the end of all these investigations. As the saying goes, good research leads to more research and essentially asks more questions than it answers. Thus, I believe further investigations into the Verwey-type transition in $\text{Pb}_3\text{Rh}_7\text{O}_{15}$ are

warranted especially given that the low temperature (below T_v) phase has not been fully defined structurally. Other substitutions for Rh and Pb may help lead down that path.

Currently, to the best of my knowledge, no substitutions showing an increase of the ferromagnetic T_c in SrRuO_3 have been reported. Although significant work in describing the itinerant ferromagnetism exhibited by SrRuO_3 has been done, successful investigation aimed at increasing the T_c of SrRuO_3 would be newsworthy.

In the case of $\text{Sr}_2\text{Ti}_{1-x}\text{Rh}_x\text{O}_4$, synthesis optimization could allow completion of the solid solution and observance of an insulator to metallic conductivity with increasing Rh. Furthermore, the search for superconductivity in structures analogous to La_2CuO_4 like Sr_2IrO_4 should continue with theoretical predictions from powerful software accompanied by physical synthesis and characterization.

Bibliography

- A.L. Allred, *J. Inorg. Nucl. Chem.* 17 (1961) 215–221.
- M. Anderson, K. Greenwood, G. Taylor, K. Poeppelmeier, *Prog. Solid State Chem.* 22 (1993) 197–233.
- P.W. Anderson, *Phys. Rev.* 102 (1956) 1008–1013.
- J. Androulakis, P. Migiakis, J. Giapintzakis, *Appl. Phys. Lett.* 84 (2004) 1099–1101.
- A.R. Armstrong, P.G. Bruce, *Nature* 381 (1996) 499–500.
- J.P. Badaud, *Comptes Rendus Hebdomadaires Des Séances De l'Académie Des Sciences. Série C. Sciences Chimiques* 278 (1974) 521.
- M.N. Baibich, J.M. Broto, A. Fert, F.N. Van Dau, F. Petroff, *Phys. Rev. Lett.* 61 (1988) 2472–2475.
- L. Balcells, J. Navarro, M. Bibes, A. Roig, B. Martínez, J. Fontcuberta, *Appl. Phys. Lett.* 78 (2001) 781–783.
- D. Balz, K. Plieth, *Z. Elektrochem.* 59 (1955) 545–551.
- J. Bardeen, L.N. Cooper, J.R. Schrieffer, *Phys. Rev.* 108 (1957) 1175–1204.
- L. Basford, *Electricity Made Simple*, 1971.
- P.D. Battle, T.C. Gibb, C.W. Jones, F. Studer, *J. Solid State Chem.* 78 (1989) 281–293.
- P.D. Battle, C.W. Jones, F. Studer, *J. Solid State Chem.* 90 (1991) 302–312.
- P.D. Battle, W.J. Macklin, *J. Solid State Chem.* 52 (1984) 138–145.
- P.D. Battle, C.P. Grey, M. Hervieu, C. Martin, C.A. Moore, Y. Paik, *J. Solid State Chem.* 175 (2003) 20–26.
- W.H. Baur, *Crystallogr. Rev.* 13 (2007) 65–113.
- J.G. Bednorz, K.A. Müller, *Z. Phys. B: Condens. Matter* 64 (1986) 189–193.
- W. Bensch, H.W. Schmalke, A. Reller, *Solid State Ionics* 43 (1990) 171–177.
- J.W.M. Biesterbos, J. Hornstra, *J. Less Comm. Met.* 30 (1973) 121–125.
- J.-W.G. Bos, J.P. Attfield, *Chem. Mater.* 16 (2004) 1822–1827.
- J.-W.G. Bos, J.P. Attfield, T.-S. Chan, R.-S. Liu, L.-Y. Jang, *Phys. Rev. B* 72 (2005) 014101.
- R.J. Bouchard, J.L. Gillson, *Mater. Res. Bull.* 6 (1971) 669–679.
- R.J. Bouchard, J.L. Gillson, *Mater. Res. Bull.* 7 (1972) 873–878.
- R.J. Bouchard, J.F. Weiher, *J. Solid State Chem.* 4 (1972) 80–86.
- R.J. Bouchard, J.F. Weiher, J.L. Gillson, *J. Solid State Chem.* 6 (1973) 519–525.
- I.D. Brown, D. Altermatt, *Acta Crystallogr., Sect. B: Struct. Sci.* 41 (1985) 244–247.
- R.C. Buchanan, *Ceramic Materials for Electronics: Processing, Properties, and Applications.*, Marcel Dekker, Inc., New York, 1986.
- V. Caignaert, F. Millange, M. Hervieu, E. Suard, B. Raveau, *Solid State Commun.* 99 (1996) 173–177.
- A. Callaghan, C.W. Moeller, R. Ward, *Inorg. Chem.* 5 (1966) 1572–1576.
- G. Cao, J. Bolivar, S. McCall, J.E. Crow, R.P. Guertin, *Physica B: Condens. Matter* 57 (1998) R11039.
- R.J. Cava, B. Batlogg, K. Kiyono, H. Takagi, J.J. Krajewski, W.F. Peck, L.W. Rupp, C.H. Chen, *Phys. Rev. B* 49 (1994) 11890–11894.
- A.K. Cheetham, P. Day, *Solid-State Chemistry: Techniques*, Oxford University Press, 1987.

- J.B. Claridge, H.-C. zur Loye, *Chem. Mater.* 10 (1998) 2320–2322.
- J.M.D. Coey, *Acta Crystallogr., Sect. B: Struct. Sci.* 26 (1970) 1876.
- M. Coey, *Nature* 430 (2004) 155–157.
- E.C. Constable, *Coord. Chem. Rev.* 73 (1986) 113–173.
- C. Cosio-Castaneda, G. Tavizon, A. Baeza, P. de la Mora, R. Escudero, *J. Phys.: Condens. Matter* 19 (2007) 446210.
- M.K. Crawford, M.A. Subramanian, R.L. Harlow, J.A. Fernandez-Baca, Z.R. Wang, D.C. Johnston, *Phys. Rev. B* 49 (1994) 9198–9201.
- S.E. Dann, M.T. Weller, D.B. Currie, *J. Solid State Chem.* 92 (1991) 237–240.
- S.E. Dann, M.T. Weller, D.B. Currie, M.F. Thomas, A.D. Al-Rawwas, *J. Mater. Chem.* 3 (1993) 1231.
- B. Darriet, M. Devalette, B. Latourrette, *Acta Crystallogr., Sect. B: Struct. Sci.* B34 (1978) 3528.
- L. Degueldre, Y. Gobillon, L. Clerbols, L. Bourgeois, U.S. Patent 3,736,270.
- M. Dlouhá, J. Hejtmánek, Z. Jiráček, K. Knížek, P. Tomeš, S. Vratislav, *J. Magn. Magn. Mater.* 322 (May) 1189–1191.
- J. Eilertsen, S. Rouvimov, M.A. Subramanian, *Acta Mater.* 60 (2012) 2178–2185.
- J. Eilertsen, J. Li, S. Rouvimov, M.A. Subramanian, *J. Alloys Compd.* 509 (2011) 6289–6295.
- H.W. Eng, P.W. Barnes, B.M. Auer, P.M. Woodward, *J. Solid State Chem.* 175 (2003) 94–109.
- I. Felner, U. Asaf, *Physica B: Condens. Matter* 337 (2003) 310–317.
- O. Feussner, *Elektrotech. Zeits.* 54 (1933) 155–156.
- R. Feyerherm, E. Dudzik, S. Valencia, J.A. Mydosh, Y.-K. Huang, W. Hermes, R. Pöttgen, *Phys. Rev. B* 85 (2012) 085120.
- R. Franz, G. Wiedemann, R. Franz, G. Wiedemann, *Annalen der Physik* 165, 165 (1853) 497, 497–531, 531.
- R. Funahashi, I. Matsubara, Siwen Li, H. Yamada, K. Ueno, Thermoelectrics, 1999. Eighteenth International Conference, 1999, pp. 153–156.
- R. Funahashi, T. Mihara, M. Mikami, S. Urata, N. Ando, Thermoelectrics, 2005. ICT 2005. 24th International Conference, 2005, pp. 307–314.
- J.A. García, M.E. Villafuerte-Castrejón, J. Andrade, R. Valenzuela, A.R. West, *Mater. Res. Bull.* 19 (1984) 649–654.
- J.S. Gardner, G. Balakrishnan, D.M. Paul, *Physica C* 252 (1995) 303–307.
- A.J. Gatimu, R. Berthelot, S. Muir, A.W. Sleight, M.A. Subramanian, *J. Solid State Chem.* 190 (2012) 257–263.
- A.J. Gatimu, H. Mizoguchi, A.W. Sleight, M.A. Subramanian, *J. Solid State Chem.* 183 (2010) 866–870.
- T.C. Gibb, R. Greatrex, N.N. Greenwood, D.C. Puxley, K.G. Snowdon, *J. Solid State Chem.* 11 (1974) 17–25.
- A.M. Glazer, *Acta Crystallogr., Sect. B: Struct. Sci.* 28 (1972) 3384–3392.
- J.B. Goodenough, *Magnetism and the Chemical Bond*, John Wiley & Sons, New York, 1963.
- J.B. Goodenough, *Phys. Rev.* 100 (1955) 564–573.
- J.B. Goodenough, *Prog. Solid State Chem.* 5 (1971) 145–399.
- R. Greatrex, G. Hu, D.C. Munro, *Mater. Res. Bull.* 21 (1986) 797–802.

- J.R. Handley, *Platinum Met. Rev.* 30 (1986) 12–13.
- R.M. Hazen, *Sci. Am.* 258 (1988) 74–80.
- T. He, J. Chen, T.G. Calvarese, M.A. Subramanian, *Solid State Sci.* 8 (2006) 467–469.
- T. He, J. Chen, H.D. Rosenfeld, M.A. Subramanian, *Chem. Mater.* 18 (2006) 759–762.
- R. Heap, M.S. Islam, P.R. Slater, *Dalton T.* (2005) 460.
- H. Hosono, *Mater. Matters* 4 32–35 (2009).
- C.J. Howard, H.T. Stokes, *Acta Crystallogr., Sect. B: Struct. Sci.* 54 (1998) 782–789.
- C.J. Howard, B.J. Kennedy, P.M. Woodward, *Acta Crystallogr., Sect. B: Struct. Sci.* 59 (2003) 463–471.
- Q. Huang, J.L. Soubeyroux, O. Chmaissem, I.N. Sora, A. Santoro, R.J. Cava, J.J. Krajewski, W.F. Peck, *J. Solid State Chem.* 112 (1994) 355–361.
- L.B. Hunt, *Platinum Met. Rev.* 31 (1987) 32–41.
- K.W. Hyung, T.Y. Kwon, Y. Jeon, *Solid State Commun.* 125 (2003) 259–264.
- H. Inouye, *Platinum Met. Rev.* 23 (1979) 100–108.
- J. Isasi, M.L. López, M.L. Veiga, C. Pico, *J. Alloys Compd.* 232 (1996) 36–42.
- J. Isasi, M.L. Veiga, F. Fernandez, C. Pico, *J. Mater. Sci.* 31 (1996) 4689–4692.
- J. Isasi, M.L. Veiga, Y. Laureiro, R. Saez-Puche, C. Pico, *J. Alloys Compd.* 177 (1991) 143–147.
- M.J. Isasi, R. Sáez-Puche, M.L. Veiga, C. Pico, A. Jerez, *Mater. Res. Bull.* 23 (1988) 595–601.
- A.L. Ivanovskii, T.I. Chupakhina, V.G. Zubkov, A.P. Tyutyunnik, V.N. Krasilnikov, G.V. Bazuev, S.V. Okatov, A.I. Lichtenstein, *Phys. Lett. A* 348 (2005) 66–70.
- G. J.E., *J. Less Comm. Met.* 111 (1985) 335–345.
- J.P. Jakubovics, Magnetism and Magnetic Materials., Institute of Metals, London, 1987.
- C.W. Jones, P.D. Battle, P. Lightfoot, W.T.A. Harrison, *Acta Crystallogr., Sect. C: Cryst. Struct. Commun.* 45 (1989) 365–367.
- T. Kajitani, Y. Ono, Y. Miyazaki, Y. Morii, Thermoelectrics, 2002. Proceedings ICT. Twenty-First International Conference, 2002, pp. 195–198.
- Y. Kamihara, T. Watanabe, M. Hirano, H. Hosono, *J. Am. Chem. Soc.* 130 (2008) 3296–3297.
- A. Kanbayasi, *J. Phys. Soc. Jpn.* 41 (1976) 1876–1878.
- A. Kanbayasi, *J. Phys. Soc. Jpn.* 44 (1978) 108–113.
- S.. Kasap, Thermoelectric Effects in Metals: Thermocouples. An e-booklet (1997–2001). N. Khosrovani, A.. Sleight, *Int. J. Inorg. Mater.* 1 (1999) 3–10.
- B.J. Kim, H. Ohsumi, T. Komesu, S. Sakai, T. Morita, H. Takagi, T. Arima, *Science* 323 (2009) 1329–1332.
- B.H. Kim, B.I. Min, *Phys. Rev. B* 80 (2009) 064416.
- S.H. Kim, P.D. Battle, *J. Magn. Magn. Mater.* 123 (1993) 273–282.
- S.H. Kim, P.D. Battle, *J. Solid State Chem.* 114 (1995) 174–183.
- G. King, P.M. Woodward, *J. Mater. Chem.* 20 (2010) 5785.
- W.D. Kingery, H.K. Bowen, D.R. Uhlmann, Introduction to Ceramics, 2nd Edition., John Wiley & Sons, New York, 1976.
- Y. Klein, I. Terasaki, *J. Phys.: Condens. Matter* 20 (2008) 295201.

- M.C. Knapp, P.M. Woodward, *J. Solid State Chem.* 179 (2006) 1076–1085.
- H. Kobayashi, M. Nagata, R. Kanno, Y. Kawamoto, *Mater. Res. Bull.* 29 (1994) 1271–1280.
- K.-I.K. Kobayashi, *Nature* 395 (1998) 677.
- W. Kobayashi, W. Tamura, I. Terasaki, *J. Electron. Mater.* 38 (2009) 964–967.
- W.D. Komer, D.J. Machin, *J. Less Comm. Met.* 61 (1978) 91–105.
- O.B. Korneta, T. Qi, S. Chikara, S. Parkin, L.E. De Long, P. Schlottmann, G. Cao, *Phys. Rev. B* 82 (2010) 115117.
- K. Koumoto, D. Rowe, *Thermoelectrics Handbook*, CRC Press, 2005, pp. 35–1–35–15.
- P. Lacorre, J.B. Torrance, J. Pannetier, A.I. Nazzal, P.W. Wang, T.C. Huang, *J. Solid State Chem.* 91 (1991) 225–237.
- A.C. Larson, R.B. Von Dreele, Los Alamos National Laboratory Report LAUR (2004) 86–748.
- V. Lazarev, I. Prosychev, S. Shaplygin, *Zh. Neorg. Khim.* 24 (1979) 313.
- Y. Le Page, L.D. Calvert, *Acta Crystallogr., Sect. C: Cryst. Struct. Commun.* 40 (1984) 1787–1789.
- H. Leiva, R. Kershaw, K. Dwight, A. Wold, *Mater. Res. Bull.* 17 (1982) 1539–1544.
- H. Leiva, R. Kershaw, K. Dwight, A. Wold, *J. Solid State Chem.* 47 (1983) 293–300.
- I. Leonov, A.N. Yaresko, *J. Phys.: Condens. Matter* 19 (2007) 021001.
- M.E. Leonowicz, K.R. Poeppelmeier, J.M. Longo, *J. Solid State Chem.* 59 (1985) 71–80.
- I. Levin, J.Y. Chan, R.G. Geyer, J.E. Maslar, T.A. Vanderah, *J. Solid State Chem.* 156 (2001) 122–134.
- C. Li, K.C.K. Soh, P. Wu, *J. Alloys Compd.* 372 (2004) 40–48.
- J.M. Longo, P.M. Raccach, J.B. Goodenough, *J. Appl. Phys.* 39 (1968) 1327–1328.
- J.M. Longo, J.A. Kafalas, R.J. Arnott, *J. Solid State Chem.* 3 (1971) 174–179.
- M.W. Lufaso, P.W. Barnes, P.M. Woodward, *Acta Crystallogr., Sect. B: Struct. Sci.* 62 (2006) 397–410.
- M.W. Lufaso, P.M. Woodward, *Acta Crystallogr., Sect. B: Struct. Sci.* 57 (2001) 725–738.
- K. Lukaszewicz, *Rocz. Chem.* 33 (1959) 239.
- G. Lunde, *Z. Anorg. Allg. Chem.* 163 (1927) 345.
- G.D. Mahan, J.O. Sofo, *Proc Natl Acad Sci USA* 93 (1996) 7436–7439.
- G. Mahan, *Solid State Phys.* 51 (1998) 81–157.
- A. Mamchik, W. Dmowski, T. Egami, I.-W. Chen, *Phys. Rev. B* 70 (2004) 104410.
- R.E. Marsh, F.H. Herbstein, *Acta Crystallogr B Struct Sci.* 39 (1983) 280–287.
- J. Matsuno, Y. Okimoto, Z. Fang, X.Z. Yu, Y. Matsui, N. Nagaosa, M. Kawasaki, Y. Tokura, *Phys. Rev. Lett.* 93 (2004) 167202.
- D.C. Mattis, *The Theory of Magnetism Made Simple.*, World Scientific Publishing Co., New York, 2006.
- I.I. Mazin, D.J. Singh, *Phys. Rev. B* 56 (1997) 2556–2571.
- A.D. McNaught, A. Wilkinson, *IUPAC Compendium of Chemical Terminology. The Gold Book.* (2nd Edition), Blackwell Science, 1997.
- M.L. Medarde, *J. Phys.: Condens. Matter* 9 (1997) 1679–1707.
- W. Meissner, R. Ochsenfeld, *Naturwissenschaften* 21 (1933) 787–788.

- D. Mikhailova, H. Ehrenberg, G. Mieke, D. Trots, C. Hess, R. Schneider, H. Fuess, *J. Solid State Chem.* 181 (2008) 190–198.
- R.H. Mitchell, *Perovskites: Modern and Ancient*, Almaz, 2003.
- K. Miwa, I. Kagomiya, H. Ohsato, H. Sakai, Y. Maeda, *J. Eur. Ceram. Soc.* 27 (2007) 4287–4290.
- Y. Miyahara, *J. Phys. Soc. Jpn.* 32 (1972) 629–634.
- H. Mizoguchi, W.J. Marshall, A.P. Ramirez, A.W. Sleight, M.A. Subramanian, *J. Solid State Chem.* 180 (2007) 3463–3468.
- H. Mizoguchi, A.W. Sleight, M.A. Subramanian, *MRS Proceedings* 1148E (2008).
- H. Mizoguchi, Y. Michiue, A.W. Sleight, M.A. Subramanian, *Inorg. Chem.* (2011).
- H. Mizoguchi, A.P. Ramirez, T. Siegrist, L.N. Zakharov, A.W. Sleight, M.A. Subramanian, *Chem. Mater.* 21 (2009) 2300–2305.
- H. Mizoguchi, L.N. Zakharov, W.J. Marshall, A.W. Sleight, M.A. Subramanian, *Chem. Mater.* 21 (2009) 994–999.
- H. Mizoguchi, L.N. Zakharov, N.S.P. Bhuvanesh, A.W. Sleight, M.A. Subramanian, *J. Solid State Chem.* 184 (2011) 1381–1386.
- P.S.R. Murthy, K.R. Priolkar, P.A. Bhoje, A. Das, P.R. Sarode, A.K. Nigam, *Eur. Phys. J. B* 78 (2010) 275–282.
- Obama Campaign, *All of the Above Approach - President Obama's Approach to Energy Independence* (2012).
- M. Ohtaki, in: *Thermoelectrics, 1999. Eighteenth International Conference On, 1999*, pp. 565–568.
- S. Okada, A. Sakai, T. Kanno, S. Yotsuhashi, H. Adachi, *J. Appl. Phys.* 105 (2009) 083711–083716.
- P.J. Omary, R. Kohlmuller, P. Batail, R. Chevalier, *Acta Crystallogr., Sect. B: Struct. Sci.* B36 (1980) 1040.
- H.K. Onnes, *Commun. Phys. Lab. Unvi. Leiden. Suppl.* 29 (1911).
- C.L. Pang, G. Thornton, *Surf. Sci.* 600 (2006) 4405–4406.
- L. Pauling, *J. Am. Chem. Soc.* 51 (1929) 1010.
- M.A. Peña, J.L.G. Fierro, *Chem. Rev.* 101 (2001) 1981–2018.
- T.F. Qi, O.B. Korneta, S. Chikara, M. Ge, S. Parkin, L.E. De Long, P. Schlottmann, G. Cao, *J. Appl. Phys.* 109 (2011) 07D906–07D906–3.
- P.G. Radaelli, D.E. Cox, M. Marezio, S.-W. Cheong, *Phys. Rev. B* 55 (1997) 3015–3023.
- P.G. Radaelli, D.E. Cox, M. Marezio, S.-W. Cheong, *Phys. Rev. B* 55 (1997) 3015–3023.
- R.J. Radwanski, Z. Ropka, *Physica B: Condens. Matter* 345 (2004) 107–110.
- J.J. Randall, L. Katz, R. Ward, *J. Am. Chem. Soc.* 79 (1957) 266–267.
- C.N.R. Rao, B. Reveau, *Transition Metal Oxides: Structure, Properties, and Synthesis of Ceramic Oxides*, 2nd Edition., John Wiley & Sons, New York, 1998.
- J.C.E. Rasch, D.V. Sheptyakov, J. Schefer, L. Keller, M. Boehm, F. Gozzo, N.V. Volkov, K.A. Sablina, G.A. Petrakovskii, H. Grimmer, K. Conder, J.F. Löffler, *J. Solid State Chem.* 182 (2009) 1188–1192.
- K. Renger, *Die Anfängliche Suszeptibilität Von Eisen Und Magnetit in Abhängigkeit Von Der Temperatur*, Zurich, 1913.
- M.B. Robin, P. Day, *Adv. Inorg. Chem. and Radiochem.* 10 (1967) 247.

- F. Rodi, Eberhardt-Karls-Universität, 1963.
- J. Rodriguez-Carvajal, *XV IUCr Congress*, 1990.
- R.D. Roof, Los Alamos Laboratory.
- Z. Ropka, R. Radwanski, *Phys. Rev. B* 67 (2003).
- D. Rowe, CRC Handbook of Thermoelectrics, 1995.
- A. Roy, J. Ghose, *Mater. Res. Bull.* 33 (1998) 547–551.
- S.N. Ruddlesden, P. Popper, *Acta Crystallogr.* 10 (1957) 538–539.
- R. Schad, C.D. Potter, P. Beliën, G. Verbanck, V.V. Moshchalkov, Y. Bruynseraede, *Appl. Phys. Lett.* 64 (1994) 3500.
- M.M. Schieber, Experimental Magnetochemistry: Nonmetallic Materials., John Wiley & Sons, New York, 1967.
- A. Schilling, M. Cantoni, J.D. Guo, H.R. Ott, Published Online: 06 May 1993; | Doi:10.1038/363056a0 363 (1993) 56–58.
- M. Schofield, *Paint Manufacture* 15 (1945) 161.
- L.W. Schroeder, M. Mathew, *J. Solid State Chem.* 26 (1978) 383–387.
- P.W. Selwood, Magnetochemistry, Interscience Publishers Inc., New York, 1943.
- R.D. Shannon, *Acta Cryst.* A32 (1976) 757 – 767.
- R.D. Shannon, C.T. Prewitt, *J. Solid State Chem.* 2 (1970) 134–136.
- I. Shaplygin, I. Prosychev, V. Lazarev, *Zh. Neorg. Khim.* 31 (1986) 2870.
- I.B. Sharma, D. Singh, *Bull. Mater. Sci.* 21 (1998) 363–374.
- G.M. Sheldrick, SHELEXTL, Version 6.14, Bruker Analytical X-ray Instruments, Inc., Madison, WI. (2003).
- M. Shikano, R. Funahashi, *Appl. Phys. Lett.* 82 (2003) 1851.
- T. Shimura, Y. Inaguma, T. Nakamura, M. Itoh, Y. Morii, *Phys. Rev. B* 52 (1995) 9143–9146.
- T. Shimura, M. Itoh, T. Nakamura, *J. Solid State Chem.* 98 (1992) 198–200.
- T. Shimura, M. Itoh, T. Nakamura, *J. Solid State Chem.* 98 (1992) 198–200.
- S. Shuba, A. Mamchik, I.-W. Chen, *J. Phys.: Condens. Matter* 18 (2006) 9215–9220.
- T. Siritanon, Structure-Property Relationships in Oxides Containing Tellurium., Doctoral, Oregon State University, 2011.
- T. Siritanon, K. Biswas, A.W. Sleight, M.A. Subramanian, *Mater. Res. Bull.* 46 (2011) 2016–2020.
- A.W. Sleight, *Mater. Res. Bull.* 6 (1971) 775–780.
- A.W. Sleight, H.Y. Chen, J.L. Gillson, ACS/CSJ Chemical Congress, Honolulu, HI, April 1-6, 1979, American Chemical Society, Washington, DC. (1979) 75.
- A.W. Sleight, *Mater. Res. Bull.* 33 (1998) 1564.
- A.E. Smith, Functional Transition Metal Oxides: Structure-Property Relationships, Oregon State University, 2010.
- A.E. Smith, H. Mizoguchi, K. Delaney, N.A. Spaldin, A.W. Sleight, M.A. Subramanian, *J. Am. Chem. Soc.* 131 (2009) 17084–17086.
- G.J. Snyder, E.S. Toberer, *Nat. Mater.* 7 (2008) 105–114.
- K.E. Stitzer, M.D. Smith, H.C. zur Loye, J. Darriet, *Chem. Commun.* (2001) 1680–1681.
- M.A. Subramanian, M.K. Crawford, R.L. Harlow, T. Ami, J.A. Fernandez-Baca, Z.R. Wang, D.C. Johnston, *Physica C* 235-240 (1994) 743–744.
- T. Sugiyama, N. Tsuda, *J. Phys. Soc. Jpn.* 68 (1999) 3980–3987.

- J. Takahashi, N. Kamegashira, *Mater. Res. Bull.* 28 (1993) 565–573.
- S. Tennant, *Phil. Trans.* 94 (1804) 411–418.
- I. Terasaki, Thermoelectrics, 2005. ICT 2005. 24th International Conference, 2005, pp. 301–306.
- I. Terasaki, N. Murayama, Oxide Thermoelectrics, Research Signpost, Trivandrum, India, 2002.
- I. Terasaki, Y. Sasago, K. Uchinokura, *Phys. Rev. B* 56 (1997) R12685–R12687.
- I. Terasaki, Y. Sasago, K. Uchinokura, Thermoelectrics, 1998. Proceedings ICT 98. XVII International Conference, 1998, pp. 567–569.
- B.H. Toby, *J. Appl. Cryst.* 34 (2001) 210–213.
- P. Tomeš, J. Hejtmánek, K. Knížek, *Solid State Sci.* 10 (2008) 486–490.
- T.M.M. Tritt, *Proceedings - Electrochem. Soc.* 2003-27 (2004) 257.
- T.M. Tritt, *Encyclopedia of Materials: Science and Technology* (2002) 1–11.
- T.M. Tritt, M.A. Subramanian, *Mater. Res. Soc. Bull.* 31 (2006) 188–198.
- E.J.W. Verwey, *Nature* 144 (1939) 327–328.
- N.V. Volkov, K.A. Sablina, O.A. Bayukov, E.V. Eremin, G.A. Petrakovskii, D.A. Velikanov, A.D. Balaev, A.F. Bovina, P. Böni, E. Clementyev, *J. Phys.: Condens. Matter* 20 (2008) 055217.
- N.V. Volkov, K.A. Sablina, E.V. Eremin, P. Böni, V.R. Shah, I.N. Flerov, A. Kartashev, J.C.E. Rasch, M. Boehm, J. Schefer, *J. Phys.: Condens. Matter* 20 (2008) 445214.
- F. Walz, *J. Phys.: Condens. Matter* 14 (2002) R285–R340.
- F. Wang, T. Senthil, *Phys. Rev. Lett.* 106 (2011) 136402.
- X.L. Wang, E. Takayama-Muromachi, *Phys. Rev. B* 72 (2005) 064401.
- P. Weiss, R. Forrer, *Ann. Phys.* 12 (1929) 279.
- P. Weiss, K. Renger, *Arch. Elektrotechn.* 11 (1914) 406.
- A.R. West, *Basic Solid State Chemistry Second Edition*, John Wiley & Sons, Ltd, Chichester, 1996.
- A.R. West, T.B. Adams, F.D. Morrison, D.C. Sinclair, *J. Eur. Ceram. Soc.* 24 (2004) 1439–1448.
- W. Westerburg, O. Lang, C. Ritter, C. Felser, W. Tremel, G. Jakob, *Solid State Commun.* 122 (2002) 201–206.
- P.M. Woodward, *Acta Crystallogr., Sect. B: Struct. Sci.* 53 (1997) 32–43.
- P.M. Woodward, *Acta Crystallogr., Sect. B: Struct. Sci.* 53 (1997) 44–66.
- P.M. Woodward, T. Vogt, D.E. Cox, A. Arulraj, C.N.R. Rao, P. Karen, A.K. Cheetham, *Chem. Mater.* 10 (1998) 3652–3665.
- J.P. Wright, J.P. Attfield, P.G. Radaelli, *Phys. Rev. B* 66 (2002) 214422.
- [221]
- M. Wu, J. Ashburn, C. Torng, P. Hor, R. Meng, L. Gao, Z. Huang, Y. Wang, C. Chu, *Phys. Rev. Lett.* 58 (1987) 908–910.
- T. Yamada, K. Suzuki, S. Chikazumi, *Appl. Phys. Lett.* 13 (1968) 172.
- H. Yoshioka, M. Tsuchiizu, H. Seo, *J. Phys. Soc. Jpn.* 76 (2007) 3701.